Astronomy & Astrophysics manuscript no. astroph˙dust˙effects˙article˙accepted
January 24, 2013

The effects of dust on the derived photometric parameters of disks and bulges in spiral galaxies

Bogdan A. Pastrav[1], Cristina C. Popescu[1,3], Richard J. Tuffs[2], and Anne E. Sansom[1]

[1] Jeremiah Horrocks Institute, University of Central Lancashire, PR1 2HE, Preston, UK
e-mail: bapastrav@uclan.ac.uk;cpopescu@uclan.ac.uk;aesansom@uclan.ac.uk
[2] Max Planck Institut für Kernphysik, Saupfercheckweg 1, D-69117 Heidelberg, Germany
e-mail: Richard.Tuffs@mpi-hd.mpg.de
[3] Visiting Scientist, Max Planck Institut für Kernphysik, Saupfercheckweg 1, D-69117 Heidelberg, Germany

Received / Accepted

ABSTRACT

We present results of a study to quantify the effects of dust on the derived photometric parameters of disks (old stellar disks and young stellar disks) and bulges: disk scale-lengths, axis-ratios, central surface-brightness, bulge effective radii and Sérsic indexes. The changes in the derived photometric parameters from their intrinsic values (as seen in the absence of dust) were obtained by fitting simulated images of disks and bulges produced using radiative transfer calculations and the model of Popescu et al. (2011). The fits to the simulations were performed using GALFIT 3.0.2 data analysis algorithm and the fitted models were the commonly used infinitely thin disks described by exponential, general Sérsic and de Vaucouleurs distributions. We find the young stellar disks to suffer the most severe variation in the photometric parameters due to dust effects. In this context we also present corrections for narrow line (Balmer line) images. Old stellar disks are also significantly affected by dust, in particular when fits are performed with exponential functions. The photometric parameters of bulges are to a lesser extent affected by dust. We also find that the variation of dust corrections with face-on dust opacity and inclination is similar for bulges with different intrinsic stellar emissivities (different Sérsic index), with differences manifesting only close to edge-on orientations of the disk. Dust corrections for bulges are found to be insensitive to the choice of the truncation radius and ellipticity of the bulge. All corrections are listed in the Appendix and made available in electronic format.

Key words. galaxies: spiral – galaxies: bulges – galaxies: photometry – galaxies: structure – ISM: dust, extinction – radiative transfer

1. Introduction

In recent years deep wide field spectroscopic and photometric surveys of galaxies (e.g. Sloan Digital Sky Survey - SDSS, York et al. 2000; The Galaxy and Mass Assembly - GAMA, Driver et al. 2011) are providing us with large statistical samples of galaxies for which major morphological components can be resolved out to z=0.1. This trend will continue into the future with the advent of VISTA/VST (Emerson & Sutherland 2010, Arnaboldi et al. 2012), which will provide wide-field imaging surveys with sub-arcsec resolution, and will culminate in the wide-field diffraction limited space-borne surveys done with Euclid (Laureijs et al. 2010). In parallel, automatic routines like GALFIT (Peng et al. 2002, Peng et al. 2010), GIM2D (Simard et al. 2002), BUDDA (Gadotti 2008) or MegaMorph (Bamford et al. 2012) have been developed to address the need of fitting large number of images of galaxies with 1D analytic functions for the characterisation of the surface brightness distribution of their stellar components. In particular Sérsic functions are the most common distributions that have been used to describe and fit the observed profiles of galaxies and their constituent morphological components (e.g. Hoyos et al. 2011, Simard et al. 2011, Kelvin et al. 2012, Häußler et al. 2012). The derived Sérsic indexes are then used (either by themselves or in combination with other photometric parameters) to classify galaxies as disk- or spheroid-dominated ones (e.g. Kelvin et al. 2012, Grootes et al. 2012) or in terms of a bulge-to-disk ratio when bulge/disk decomposition is performed (Allen et al. 2006, Simard et al. 2011, Lackner & Gunn 2012).

One potential problem with the interpretation of the results of Sérsic fits is that the measured Sérsic parameters differ from the intrinsic ones (as would be derived in the absence of dust). This is because real galaxies, in particular spiral galaxies, contain large amounts of dust (e.g Stickel et al. 2000, Tuffs et al. 2002, Popescu et al. 2002, Stickel et al. 2004, Vlahakis et al. 2005, Driver et al. 2007, Dariush et al. 2011, Rowlands et al. 2012, Bourne et al. 2012, Dale et al. 2012, Grootes et al. 2013) and this dust changes their appearance from what would be predicted to be seen in projection based on only their intrinsic stellar distributions (e.g. Tuffs et al. 2004, Möllenhoff et al. 2006, Gadotti et al. 2010). Determining the changes due to dust is thus essential when characterising and classifying galaxies based on their fitted Sérsic indexes (Pastrav et al. 2012). In addition it is, for a variety of reasons, essential to quantitatively understand and correct for the effects of dust on all photometric parameters derived from Sérsic fits, such as scale-lengths, effective radii, axis-ratios, surface-brightnesses and integrated luminosities.

Thus, knowledge of the scale-length of disks of galaxies is essential in understanding how these systems were assembled over cosmic time. If the disks of spiral galaxies grow from the inside out, as predicted by semi-analytical hierarchical models for galaxy formation (e.g. Mo et al. 1998), one would predict the stellar populations to be younger and have lower metallicity in the outer disk than in the inner disk, such that local universe galaxies should be intrinsically larger at the shorter wave-

lengths where light from the young stellar population is more prominent. For the same reason one would expect the intrinsic sizes of spiral disks to be larger at the current epoch than at higher redshift. Observationally, such predictions can be tested in two ways. One way is to compare the spatial distribution of the constituent stellar populations at different wavelengths, for local universe galaxies. Another way is to look for structural differences in galaxies observed at different cosmological epochs, at the same rest frame wavelength. Both methods require knowledge of the scale-length of disks, as measured at different wavelengths or at different redshifts (and therefore potentially for different dust opacities in disks). Since the effect of dust on the measured scale-lengths varies as a function of wavelength and disk opacity (e.g. Möllenhoff et al. 2006), it is imperative to quantify these effects on the derived scale-lengths. Accurate knowledge of the intrinsic scale-lengths of disks is also important when modelling the radiation fields in galaxies based on self-consistent calculations of the transfer of radiation in galaxy disks, since any scaling of solutions will depend on the surface area of the disk, and therefore on the square of the scale-length.

Another photometric parameter derived from surface-brightness photometry is the axis-ratio of the disk, which traditionally has been used as a proxy for estimating disk inclinations (Hubble 1926). Here again it is important to quantify the effects of dust on the derived ratios, in particular in studies that require precise knowledge of inclination, as for example in radiative transfer modelling of spiral disks. In the future high precision measurements of axis ratios of galaxies will be the main tool in quantifing the weak lensing effects in experiments aimed in understanding the nature of dark energy in the universe (Peacock 2008, Jouvel et al. 2011, Cimatti & Scaramella 2012) or in constraining modified gravitational theories (Martinelli et al. 2011). In these studies even small systematic deviations introduced by dust could prove important when estimating weak lensing effects.

Surface brightness measurements are an integral part of resolved studies of stellar populations, and quantitative corrections due to dust are required for a proper analysis which removes degeneracies due to dust. Studies of bulges in galaxies also require their effective radii and surface brightness distributions to be corrected for the effects of dust. This is because, although bulges themselves may be largely devoid of dust, they are seen through copious amounts of dust in the interstellar medium in the central regions of disks (Tuffs et al. 2004, Driver et al. 2007). Finally, measurements of scale-lengths and luminosities of narrow band images, like those of Balmer lines or of nebular lines, are also important in understanding the extent to which star-formation is distributed in galaxies, and again these studies will rely on proper corrections due to dust.

While a long list of reasons for the importance of proper dust corrections on the derived photometric parameters of galaxies can be still continued, we should only mention one last topic, namely that of scaling relations in galaxies (see Graham 2011 for a review on this topic). These relations are extremely important because they provide direct insights into the physical mechanisms of how galaxies assembly over cosmic time. Graham & Worley (2008) used the radiative transfer model of Popescu et al. (2000) and the predictions for dust corrections for brightness and scale-length of disks from Möllenhoff et al. (2006) to analyse the intrinsic (dust corrected) luminosity-size and (surface-brightness)-size relations for discs and bulges. Recently Grootes et al. (2012) found a strong relation between dust opacity and stellar surface mass density, a relation that was derived making use of dust corrections (Pastrav et al. in prep.) calculated from simulations produced with radiative transfer models (Popescu et al. 2011). The work of Graham & Worley (2008) and of Grootes et al. (2012) demonstrated the crucial importance of proper dust corrections on the analysis of scaling relations for galaxies.

At this point one could ask the retorical question of why should we not try to do a proper job from the beginning, and fit images of galaxies with realistic surface distributions that already take into account the distortions due to dust. The first answer to this question is that no analytic functions exist to describe the complex modifications to surface brightness distributions induced by dust. Nonetheless, such modified surface brightness distributions can be calculated using radiative transfer codes, and indeed such simulations already exist in the literature (e.g. Tuffs et al. 2004, Popescu et al. 2011) or could be potentially produced. The problem is, however, that instead of fitting one or two analytic functions with a few free parameters, as usually done by the observers, one would need to find the best fit distribution from a large data set of simulations corresponding to all combinations of parameters describing dust effects. When knowing that even simple function fitting is computationally a difficult task when dealing with large samples of galaxies, it becomes immediately apparent that complex distribution fitting, though desirable, is computationally impractical. The goal of this paper is therefore not to provide a better description of "nature", but to use realistic descriptions to provide observers with a means of correcting their simplistic - but necessary - approach to the quantification of the appearance of galaxies.

The approach of providing corrections due to dust is not new, and has been already used in the past to quantify these effects on the photometric parameters derived from surface brightness photometry, especially for disks (Byun et al. 1994, Evans et al. 1994, Cunow 2001, Möllenhoff et al. 2006, Gadotti et al. 2010). While there is overall consistency in the general trends found in these studies, the amplitude of the effects depend on the details of the geometrical model and/or of the optical properties of the grains used in the radiative transfer simulations, and, to some extent, on the fitting algorithm used to compare these simulations with the commonly used analytic functions. In some cases simplifying assumptions in the calculations of simulations can also account for differences in results (e.g. ignoring scattered light; Evans et al. 1994).

This paper follows-on from our previous study from Möllenhoff et al. (2006), where we quantified the effects of dust on the derived photometric parameters of disks only, seen at low to intermediate inclinations. In keeping with our previous approach we used simulations based on a model that can simultaneously account for both dust-attenuation in the UV/optical range and dust emission in the Mid-infrared (MIR)/Far-infrared (FIR)/sub-mm range. Most of the simulations come from the library of Popescu et al. (2011), while additional simulations have been created for the purpose of this paper. In particular in this paper we quantify the effects of dust on all morphological components of spirals, including bulges of different Sérsic indexes and young stellar disks seen in the ultraviolet. We also consider corrections for photometric parameters on narrow-line imaging. Another goal of this paper is to quantify the effects of dust when fits are done with general Sérsic functions with variable Sérsic indexes, even for cases of exponential disks, since, as we will show in this paper, dust can even alter the type of function (the Sérsic index) that provides the best fits to dust-attenuated images. In addition we disentangle in this paper dust effects from projection effects of the combined radial and vertical distribution of stellar emissivity, and give detailed corrections for both effects, to be used individually or in conjuction, as may better

serve the purpose of observers. In this paper we provide a comprehensive data set of corrections that cover the whole parameter space in dust opacity, inclination and wavelength for all morphological components in spiral disks. All the corrections are made publically available at the CDS database. These corrections describe the effect of dust on each morphological component taken individually, as seen through a common distribution of dust. When more morphological components need to be decomposed, dust may introduce an extra effect on the decomposition itself. We do not attempt to describe this latter effect here. The effect of dust on bulge-disk decomposition has been previously discussed by Gadotti et al. (2010) and will be the object of a future study (Pastrav et al. in prep).

This paper is organized as follows. In Sect. 2, we briefly describe the stellar emissivity and dust distributions used in the simulations. The method and general approach used to fit the simulated images and to derive the apparent photometric parameters is explained in Sect. 3, while the technical details of the whole fitting process are presented in Sect. 4. The projection effects are presented and discussed in Sect. 5, while in Sect. 6 we show and comment on the results for dust effects on the derived photometric parameters, for each morphological component. In Sect. 7, we discuss the effect on the dust and projection corrections of changing some of the geometrical parameters of our model. In Sect. 8 we compare the predictions of our model with recent observational data coming from the GAMA survey and in Sect. 9 we summarize the results and present our conclusions.

2. The simulated images

Since the philosophy of this paper is to provide corrections to observers, our approach is to follow as closely as possible the procedures and algorithms observers use to perform surface brightness photometry of real images of galaxies. It is just that instead of using observations of galaxies we use simulations for which the input parameters describing the distributions of stellar emissivity and dust are known. By comparing the input values of the parameters describing the simulations with the values of the measured parameters describing simplified distributions, as used by the observers, we can then quantify the degree to which observers underestimate or overestimate the intrinsic parameters of galaxies, under the assumption that the simulations are a good representation of observed galaxies.

Our simulations were produced as part of the large library of dust and PAH emission SEDs and corresponding dust attenuations presented in Popescu et al. (2011). The details of these calculations are described in length in Popescu et al. (2011). Here we only briefly mention their main characteristics. All the simulations were calculated using a modified version of the ray-tracing radiative transfer code of Kylafis & Bahcall (1987), which include a full treatment of anisotropic scattering, and the dust model from Weingartner & Draine (2001) and Draine & Li (2007), incorporating a mixture of silicates, graphites and PAH molecules.

The simulations were produced separately for old stellar disks, bulges and young stellar disks, all seen through a common distribution of dust. The geometrical model of Popescu et al. (2011) consists of both a large scale distribution of diffuse dust and stars, as well as a clumpy component physically associated with the star forming complexes. For the purpose of this study only the large scale distribution of diffuse dust is considered, as it is this that affects the large-scale distribution of UV/optical light determining the values of parameters typically used in fitting surface-brightness distribution (as listed in Sects. 3 and 4).

The intrinsic volume stellar distributions were described by exponential functions in both radial and vertical direction for the disks and by deprojected de Vaucouleurs functions for the bulges. The corresponding dust distributions were described by double (radial and vertical) exponential functions for the two dust disks of the model. The length parameters of the model describing the volume emissivity for stars and dust: scale-lengths, scale-heights, effective radii, are listed in Table 1 in Tuffs et al. (2004). The relevant information for this work is that the old stellar disk component has a scale-length that decreases with increasing optical/NIR wavelength, as given in Table 2 in Tuffs et al. (2004), while the scale-height remains constant over this wavelength range. Similarly, the effective radius of the bulge does not vary with optical/NIR wavelength. The bulge is an oblate ellipsoid with an axial ratio (thickness) of 0.6. For the purpose of testing the effects of changing the ellipticity of the bulge on the derived corrections, we also produced a few simulations for spherical bulges. The young stellar disk has a much smaller scaleheight than the older stellar disk (by a factor of 4.6), while its scalelength is constant over wavelength and is equal to that of the old stellar disk in the B band. The scalelength of the dust disk associated with the old stellar population is larger (by a factor of 1.4) than that of the corresponding stellar disk, while its scaleheight is smaller (by a factor of 1.5) than the scaleheight of the old stellar disk. By contrast, the young stellar disk spatially coincides with its associated dust disk (same scaleheights and lengths). The physical interpretation of this model and the way some of the geometrical parameters have been empirically constrained from data are also described in length in Tuffs et al. (2004) and Popescu et al. (2011). A schematic representation of the geometrical model can be found in Fig. 1 from Popescu et al. (2011).

Apart from these already existing simulations additional ones have been produced for the purpose of this study. These are simulations of bulges corresponding to general Sérsic functions with various Sérsic indexes. Since there is no exact analytical deprojection of Sérsic functions, the simulations were created with volume emissivities that, for the case of untruncated distributions, will reproduce Sérsic distributions of various Sérsic indexes.

All the simulated images have 34.54 pc/pixel. The disks were produced with a truncation radius at 5 exponential scalelength of the volume stellar emissivity. For bulges we produced two sets of simulations, with truncations at 3 and 10 effective radii, respectively. The truncation at $3R_0^{eff}$ was chosen as this avoids the problem of having a disk-bulge system dominated by the bulge light at high galactocentric radii for large values of the Sérsic index. The truncation at $10R_0^{eff}$ is essentially representative of a bulge with no truncation at all, since at this galactocentric radius almost all the light inside the profile has been accounted for.

Here we note that the simulations for old stellar disks presented in this paper slightly differ from the disk simulations from our previous study in Möllenhoff et al. (2006). This is due to the updates in the dust model used in Popescu et al. (2011), which included the incorporation of PAH molecules. Thus, though both the old dust model (from Popescu et al. 2000, as used in the simulations from Möllenhoff et al. 2006) and the new one can simultaneously account for the extinction and emission properties of the diffuse dust in the Milky Way, the relative contribution of scattering and absorption to the total extinction differ in the two models. This produces some small differences in the simulations.

The simulations used in this paper span the whole parameter space of the model of Popescu et al (2011). Thus simu-

lations were produced for 7 values of central face-on B band optical depth τ_B^f, 21 values for the disk inclination, 5 standard optical/NIR bands B,V,I,J,K (for disk, thin disk and bulge) and 9 FUV to NUV wavebands (for thin disk, corresponding to wavelengths of 912 Å, 1350 Å, 1500 Å, 1650 Å, 2000 Å, 2200 Å, 2500 Å, 2800 Å and 3650 Å). The values of the dust opacity cover a wide range, from almost dustless to extremely optically thick cases, $\tau_B^f = 0.1, 0.3, 0.5, 1.0, 2.0, 4.0, 8.0$. The inclination values were chosen in such a way that $\triangle \cos(i) = 0.05$, with $1 - \cos(i) \in [0, 1]$, resulting in 21 values. For each case corresponding dustless simulations were produced to provide the reference point for quantifying the effects of dust and to also assess projection effects of the stellar distributions (see Sect. 3).

3. The method and general approach

Following the approach taken by observers on real images, all the simulated images were fitted with infinitely thin disks described by exponential (Eq. 1), Sérsic (Eq. 2), or de Vaucouleurs (Eq. 3) distributions:

$$\Sigma(r) = \Sigma_0\ exp(-\frac{r}{r_s}) \tag{1}$$

$$\Sigma(r) = \Sigma_0\ exp[-\kappa_n(\frac{r}{r_e})^{1/n}] \tag{2}$$

$$\Sigma(r) = \Sigma_0\ exp[-\kappa_4(\frac{r}{r_e})^{1/4}] \tag{3}$$

where Σ_0 is the central surface brightness of the infinitely thin disk, r_s and r_e is the scale-length and effective radius[1] of the infinitely thin disk respectively, n is the Sérsic index, while κ_n is a variable, coupled with n (e.g. Ciotti & Bertin 1999, Graham & Driver 2005).

From the formulation of the fitting functions it is clear that, even in the absence of dust, these simple distributions would differ from those of real galaxies due to the fact that they describe infinitely thin disks, while disks and bulges have a thickness. This means that in real life there would be an additional vertical distribution of stars superimposed on the corresponding radial distribution. This would produce isophotal shapes which are different from those predicted by an infinitely thin disk. We call these effects **projection effects**.

The approach adopted in this paper is to separate projection effects from dust effects. Thus, we first derive the projection effects, by calculating the change between the intrinsic parameters of the volume stellar emissivity and those measured on dustless images. Subsequently, we derive the dust effects by calculating the change between the parameters measured on dustless and dusty images, respectively, for the same inclination and wavelength. So the total change in parameter values between the measured ones on dusty images and the corresponding parameters of the volume stellar emissivity can be written as a chain of corrections. In the case that the parameter is either the exponential scale-length R or the Sérsic effective radius R^{eff} of the surface-brightness distribution of the measured object, then the total correction can be written as

$$corr(A) = corr^{proj}(A) * corr^{dust}(A) \tag{4}$$

[1] such that half of the total flux is within r_e

with

$$corr^{proj}(A) = \frac{A_i}{A_0} \tag{5}$$

$$corr^{dust}(A) = \frac{A_{app}}{A_i} \tag{6}$$

where A is either R or R^{eff}, A_0 is the corresponding parameter describing the volume stellar emissivity (which we call *"intrinsic parameter of the volume stellar emissivity"*), A_i is the corresponding fitted parameter of the dustless simulated image (which we simply call *"intrinsic"* parameter), and A_{app} is the fitted parameter of the dust attenuated simulated image (which we call *"apparent"* parameter).

Eqs. 4,5 and 6 also apply for the fitted axis-ratio Q, except that the meaning of the quantities defining $corr^{proj}$ in Eq. 5 are different, since, as we will see later, it only makes sense to express corrections with respect to an infinitely thin disk case.

In the case that the fitted parameter is the Sérsic index n^{sers} the corrections are additive, since they are expressed as differences instead of ratios. The corresponding formulas for them become:

$$corr(B) = corr^{proj}(B) + corr^{dust}(B) \tag{7}$$

with

$$corr^{proj}(B) = B_i - B_0 \tag{8}$$

$$corr^{dust}(B) = B_{app} - B_i \tag{9}$$

Eqs. 7, 8 and 9 also apply for the fitted parameter surface-brightness, except that the term $corr^{proj}$ in Eq. 8 is again not taken with respect to the volume stellar emissivity. This is because surface-brightness is by definition a projected quantity (describing a surface). We define this correction with respect to the simulated image without dust.

One advantage of separating projection from dust effects is that this provides observers with a larger flexibility in using these corrections, according to different needs. In some cases observers may be only interested in the pure dust effects ($corr^{dust}$), in other cases the interest may be in deriving the intrinsic parameters of the volume stellar emissivity (e.g. $corr^{dust} * corr^{proj}$).

Another advantage of this approach is that it provides a more robust quantification of the dust effects. As we will show in this paper, the term related to projection effects $corr^{proj}$ is affected by variations in the geometrical parameters of the volume stellar emissivity, including the truncation radius, while the term related to dust effects $corr^{dust}$ is relatively insensitive to such factors. This of course is true as long as both terms are derived on simulations produced with the same geometrical parameters: e.g. truncation radius.

Finally, the approach of chain corrections allows further corrections to be added to the formula, if more complex cases are to be considered. The best example of the generalisation of this formula is for multicomponent fits. Thus, when bulge-disk decomposition is to be performed, an additional correction would need to be calculated. This is the correction between the fitted parameters obtained from bulge-disk decomposition in the presence of dust, and the fitted parameters of the same bulge and disk, if they were to be observed alone through the same distribution of dust. If we were to use the example from Eq. 4 and Eq. 7, the generalisation of these formulas for the case of bulge/disk decomposition is:

$$corr(A) = corr^{proj}(A) * corr^{dust}(A) * corr^{B/D}(A) \quad (10)$$

$$corr(B) = corr^{proj}(B) + corr^{dust}(B) + corr^{B/D}(B) \quad (11)$$

where the additional terms are

$$corr^{B/D}(A) = \frac{A_{app}^{B/D}}{A_{app}} \quad (12)$$

$$corr^{B/D}(B) = B_{app}^{B/D} - B_{app} \quad (13)$$

The additional term $corr^{B/D}$ will be quantified in a separate paper (Pastrav et al. in prep) for all photometric parameters, and will be related to the effects described here through equations like Eqs. 10 and 11.

All corrections are presented in terms of polynomial fits. Most of the fits are of the form:

$$corr(x) = \sum_{k=0}^{N} a_k\, x^k \quad \text{for} \quad 0 \le x \le 0.95 \quad (14)$$

where $x = 1 - \cos(i)$ and N has a maximum value of 5. In the case of the axis-ratio of disks Q, a combination of a polynomial and a constant was neccesary, according to different ranges in inclination (see Sects. 5.1 and 6.1).

4. The fitting procedure

For the fitting routine we used the commonly used GALFIT (version 3.0.2) data analysis algorithm (Peng et al. 2002, Peng et al. 2010). GALFIT uses a non-linear least squares fitting, based on the Levenberg-Marquardt algorithm. Through this, the goodness of the fit is checked by computing the χ^2 between the simulated image (in the case of observations, the real galaxy image) and the model image (created by GALFIT, to fit the galaxy image). This is an iterative process, and the free parameters corresponding to each component are adjusted after each interation in order to minimimise the normalized (reduced) value of χ^2 (χ^2/N_{DOF}, with N_{DOF}=number of pixels-number of free parameters, being the number of degrees of freedom).

Since in our simulated images we do not have noise, we use as input to GALFIT a "sigma" image (error/weight image) which is constant for all pixels, except for points outside the physical extent of our simulated images. The latter were set to a very high number, to act as a mask. This was necessary since our simulations are truncated in their volume stellar and dust emissivities while the fitting functions extend to infinity. We did not try to use the truncation functions from GALFIT, as this would only work properly for truncations done on surface stellar brightnesses. The simulated images have no background (by construction, unlike real images); this is why the sky value was set to zero during the fitting procedure, for all morphological components.

To fit the simulated images we used the exponential ("expdisk"), the Sérsic ("sersic") and the de Vaucouleurs ("devauc") functions, as available in GALFIT. As explained in Sect. 3, these functions represent the distribution of an infinitely thin disk, and their mathematical description is given by Eqs. 1, 2 and 3

Since our simulations were produced with high resolution and were not convolved with any instrumental PSF, during the fitting procedure there was no need to use the PSF component available in GALFIT. It should however be noted that for lower resolution observations, where deconvolution from PSF is essential, an extra correction needs to be added to the corrections presented here. This is because the deconvolution itself is affected by dust. This effect will be analysed in future papers. Here we only note that such a correction, when available, could be simply added in our formulation of chain corrections. Eq. 4 and 7 would then become:

$$corr(A) = corr^{proj}(A) * corr^{dust}(A) * corr^{PSF}(A) \quad (15)$$

$$corr(B) = corr^{proj}(B) + corr^{dust}(B) + corr^{PSF}(B) \quad (16)$$

where the additional terms are

$$corr^{PSF}(A) = \frac{A_{app}^{PSF}}{A_{app}} \quad (17)$$

$$corr^{PSF}(B) = B_{app}^{PSF} - B_{app} \quad (18)$$

The terms A_{app}^{PSF} or B_{app}^{PSF} represent the measured values of the photometric parameters A or B, which would be derived from fits done on dust-attenuated simulations convolved with PSFs. In this case the corrections will be a function of resolution.

Coming back to our fully sampled simulations, for the measurements presented in this paper the free parameters of the fit are: the X and Y coordinates of the centre of the galaxy in pixels, the integrated magnitude of the image, the scale-length R (for exponential)/ effective radius R^{eff} (for Sérsic and de Vaucouleurs functions), axis-ratios Q, Sérsic index n^{sers} (for Sérsic function) and position angle. The axis-ratio Q is defined as the ratio between the semi-minor and semi-major axis of the projected image. The position angle is the angle between the semi-major axis and the Y axis and it increases in counter clock-wise direction. For all our simulated images, the position angle was fixed to -90 (semi-major axis perpendicular on Y axis).

5. Projection effects

The main goal of this work, that of quantifying the changes due to dust on the derived photometric parameters of the main morphological components of spiral galaxies, is achievable due to the fact that, as mentioned before, the intrinsic parameters of the volume stellar emissivity are known, since they are input in the simulations. However, even in the absence of dust, the derived photometric parameters of the images measured from fitting infinitely thin disk distributions would differ from the intrinsic parameters of the volume stellar emissivity due to the thickness of real galaxies, which we call projection effects. Quantifying projection effects allows us to derive the change between the intrinsic parameters of the volume stellar emissivity and those measured on non-dusty images, which, subsequently, can be used to measure the changes between the parameters of the dustless and dusty images, respectively.

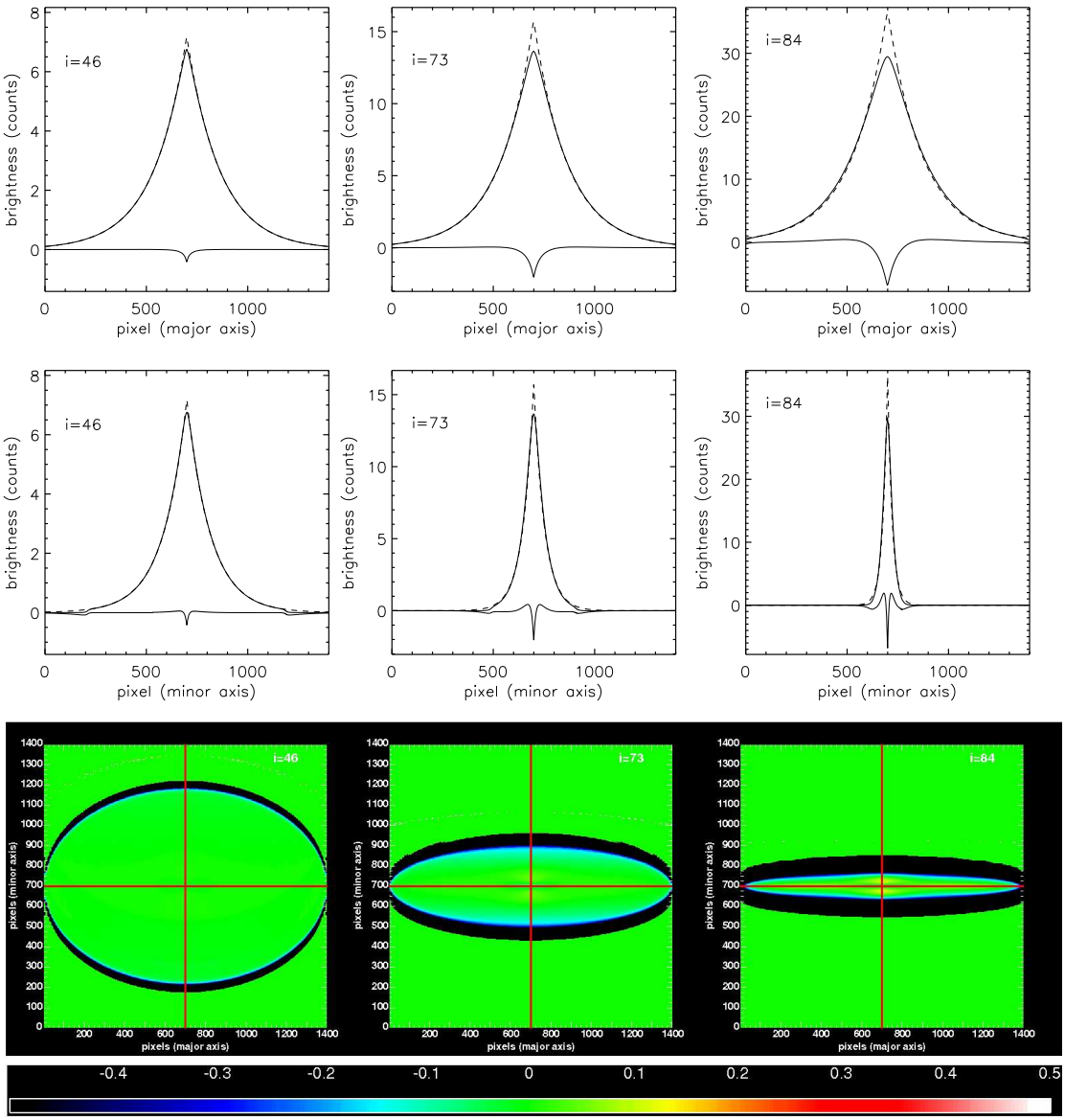

Fig. 1. Major and minor axis **disk** profiles (**upper and middle rows**) showing the deviations from pure exponentials due to projection effects. Solid upper curves are for **B band** dust-free images, dashed curves are for corresponding exponential fits, while absolute residuals (*simulation* − *fit*) are represented by solid lower curves. The fits were done by fixing the position of the intensity peak of the fitted image to the geometrical center of the map, which, in this case, corresponds to the intensity peak in the simulated image. The cuts were taken parallel and perpendicular to the major axis of the disk images, through their geometrical centers, at inclinations $1 - \cos(i) = 0.3, 0.7, 0.9$ ($i = 46°, 73°, 84°$). **Lower row**: Corresponding relative residuals ($\frac{simulation-fit}{simulation}$), at the same inclinations as the profiles. The red lines show radial and vertical cuts through the geometrical centre of each image.

5.1. The Disk

Disks are fairly thin objects; their vertical extent is significantly smaller than their radial extent (by a factor of 10 or so in our model; Tuffs et al. 2004). This means that projection effects will only start to be visible close to edge-on orientations, when the vertical distribution of stars becomes apparent.

5.1.1. Exponential fits to the disk

To quantify the projection effects we first fitted the dustless simulated images with an infinitely thin exponential disk, as available in GALFIT. To observe the accuracy of the fits, we analysed both the profiles and the relative residual maps, between the simulated and the fitted images. In the upper and middle rows of Fig. 1, we present the major and minor axis profiles for the B band images, for three orientations of the disk. At lower inclinations the exponential fits are a good representation of the profiles, while at higher inclinations deviations from a pure exponential start to appear due to above mentioned projection effects. In particular, these deviations can be seen in the central part of the disks - the flattening of the simulated profiles. At higher inclinations, projection effects produce deviations from a pure exponential also at intermediate radii, with stronger effects in the minor axis direction. For example, at an inclination of 84°, Fig. 1 (lower row, right panel) shows a deviation of up to 15% in the minor axis direction (the yellow wings; see also the corresponding double peak in the minor axis profile residuals in Fig. 1, second row). The black area that surrounds the disk, corresponding to very large relative residuals, appears because the simulated

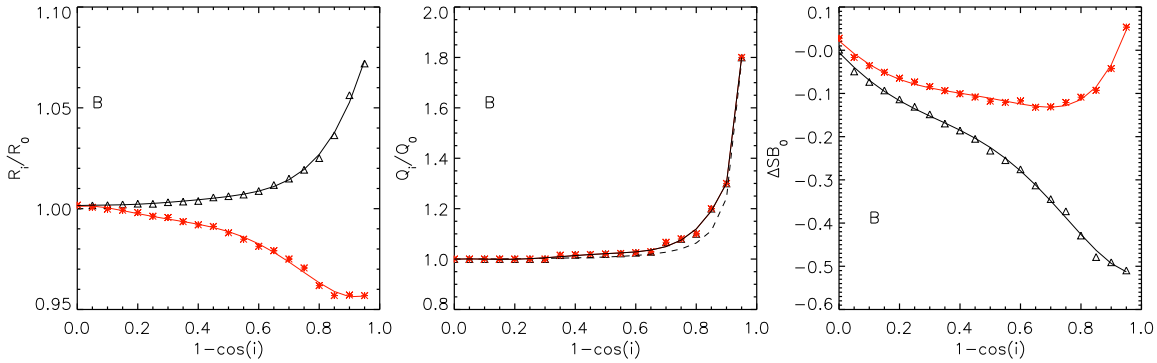

Fig. 2. Projection effects $corr^{proj}$ on the derived B band photometric parameters of **disks fitted with exponential fuctions** (black) and with **Sérsic functions** (red) : scale-lengths, axis-ratios and central surface brightnesses. The symbols represent the measurements while the solid line are polynomial fits to the measurements.The plots represent the inclination dependence of: **left** - the ratio between the intrinsic scale-lengths, R_i, and the intrinsic (radial) scale-length of the volume stellar emissivity, R_0; **middle** - the ratio between the intrinsic axis-ratio, Q_i, and the axis-ratio of an infinitely thin disk, Q_0; with dashed line we overplotted the analytic formula from Driver et al. 2007, which is a modification of the Hubble formula from Hubble 1926, to take into acount the thickness of the disk; **right** - the ratio between the central surface brightness of the fitted images and of the coresponding simulated images, ΔSB_0, expressed in magnitudes. In the case of a Sérsic fit, R_i (left panel) is the equivalent intrinsic scale-length, calculated from the derived intrinsic Sérsic effective radius, R_i^{eff}, using the relation $R_i^{eff} = 1.678R_i$ (which is an exact transformation only for $n^{sers} = 1$).

images are truncated, while the exponential fitted images extend to infinity (as explained in Sect. 4, we did not attempt to use the truncation features of GALFIT).

To understand the cause of all these deviations we need to remember that what we try to do is to fit the projection of two exponential distributions (radial and vertical) with one single exponential, which will inevitably result in an imperfect fit. As long as the vertical extent of the disk will project within the predicted elliptical shape of the infinitively thin disk, meaning as long as the axis ratios of the measured isophotes will correspond to the predicted cos(i) inclination of the infinitly thin disk, the projected stellar distribution will be dominated by the radial exponential distribution of the disk, and the fit will accurately reproduce this radial distribution. At higher inclinations the vertical extent of the disk will increase the measured axis ratio of the projected elliptical isophotes (from the predicted cos(i) ratio). This means that the measured axis ratio will not be a good representation of the inclination of the disk. This also means that the fit with an infinitely thin exponential disk will try to account for the extra thickness of the measured elliptical isophotes by trying to force a solution with a larger scale-length. This will produce the deviations from a pure exponential seen in the plots and will systematically overestimate the radial scale-length of the disk and underestimate the inclination of the disk on the basis of an infinitely thin disk approximation only.

The results on this analysis allows us to derive projection effects $corr^{proj}$ on stellar disks using Eq. 5 for the exponential scale-length and axis-ratio and Eq. 8 for the central surface brightness. The inclination dependence of these corrections are shown in Fig. 2. As explained above, the disk scale-length is relatively insensitive to projection effects at low to intermediate inclinations (left panel, Fig. 2), while close to edge-on orientations it increases with inclination with respect to the radial scale-length of the volume stellar emissivity. We note here that the amplitude of these results slightly varies with the wavelength at which the measurements are taken. This happens because the simulations originate from a volume stellar emissivity having a varying radial scale-length with wavelength (for a fixed scale-height), as prescribed in the model of Popescu et al. (2011). Here we only show the results for the B band, as the overall trend in the variation of the derived scale-lengths with inclination is the same for all wavebands. The results for all wavebands are given in the form of polynomial fits (Eq. 14), and are listed in Table A.1.

The deviation of the derived disk axis-ratios from the corresponding axis-ratio of an infinitely thin exponential disk ($corr^{proj}(Q)$) is plotted in the middle panel of Fig. 2, as a function of inclination. As expected, at low inclination the thin disk approximation works very well, while at high inclination the vertical distribution of stars introduces an extra thickness, which cannot be taken into account by the infinitely thin approximation. To account for the steep increase in the measured axis ratio with respect to that of an infinitely thin disk, at high inclination, we had to fit the measurements with a combination of a 5th order polynomial and a constant, of the form:

$$corr(x) = \begin{cases} \sum_{k=0}^{N} a_k\, x^k & \text{for } 0 \le x \le 0.90 \\ b_0 & \text{for } x = 0.95 \end{cases} \qquad (19)$$

where $x = 1 - \cos(i)$. The coefficients of these polynomial fits are listed in Table A.2, for the B,V,I,J,K bands.

Here we also checked that the analytical formula used in Driver et al. (2007) [2] to account for the finite thickness of the disk is a good representation of the dependence of the measured axis ratios on inclination (see overplotted dashed line in Fig. 2, middle).

Finally, we looked at the distortions introduced by the projection effects on the derived central surface brightness ratios ($corr^{proj}(SB)$). Here we considered two measurements. The first one is the measurement for the central pixel, where we calculated the ratio between the central surface brightness for the fitted dustless images of the old stellar disk and the central surface brightness for the corresponding simulated images, ΔSB_0 (Fig. 2, right). The ratios are expressed in magnitudes. A second measurement is to consider an average of the surface brightness over

[2] $Q_i^2 = \cos^2(i) + q^2(1 - \cos^2(i))$, with q being the ratio between the intrinsic scale-height and scale-length of the volume stellar emissivity of the disk, having different values for each optical band

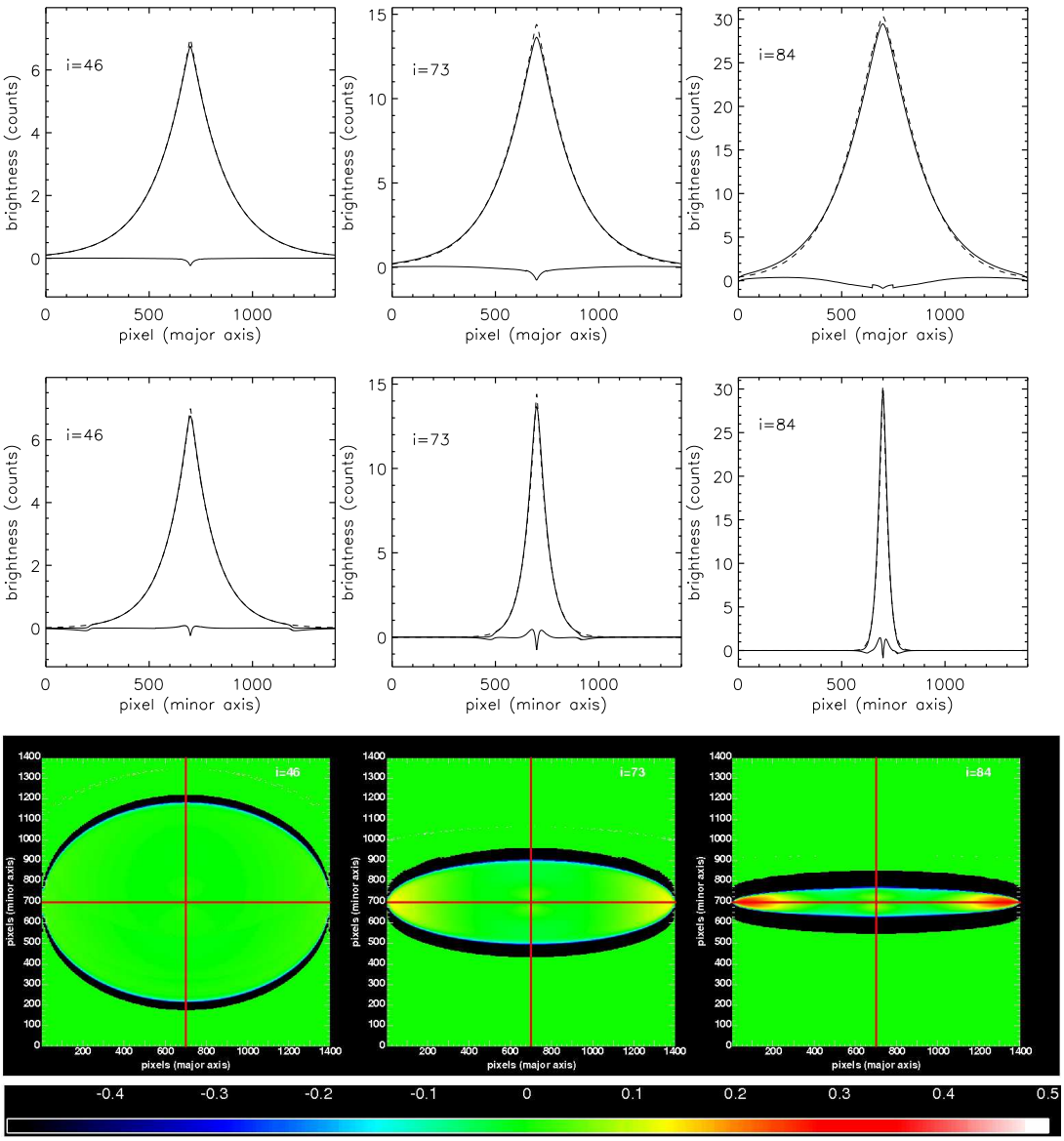

Fig. 3. Major and minor axis **disk** profiles (**upper and middle rows**) showing the deviations from Sérsic functions due to projection effects. Solid upper curves are for **B band** dust-free images, dashed curves are for corresponding variable-index Sérsic fits, while absolute residuals (*simulation* − *fit*) are represented by solid lower curves. The fits were done by fixing the position of the intensity peak of the fitted image to the geometrical center of the map. The cuts were taken parallel and perpendicular to the major axis of the dustless disk images, through their geometrical centers, at inclinations $1 - \cos(i) = 0.3, 0.7, 0.9$ ($i = 46°, 73°, 84°$). **Lower row**: Corresponding relative residuals ($\frac{simulation-fit}{simulation}$) at the same inclinations as the profiles. The red lines show radial and vertical cuts through the geometrical centre of each image.

an elliptical aperture. This second measurement is necessary as a reference for measurements of surface brightness in simulations that include dust. As we will see in Sect. 6, dust introduces asymmetries in the surface-brightness distribution, therefore it only make sense to take an average measurement in the central region. Furthermore, in real observations central regions may be affected by resolution effects, which result in essentially an averaging of the signal. For this reason we define the average central surface brightness ratio, as $\Delta SB_0 = -2.5log(F_i/F_s)$: the ratio of the average central surface brightness (F_i) of the fitted dustless disk images, and the average central surface brightness of the simulated dustless disk images (F_s). Both F_i and F_s were calculated as an average over an elliptical aperture centred on the position of the geometrical centre of the simulated image, with a semi-major axis of $R_i/10$ and an axis-ratio of Q_i. In this case the geometrical centre coincides with the coordinates of the intensity peak of the fitted image and of the simulated image.

As expected for the dustless case, the trends in the corrections for the central pixel ΔSB are the same as for the average ΔSB. These corrections are tabulated in Table A.1, in form of polynomial fits (Eq.14). Overall, the distortions in the surface brightness due to projection effects are negligible at face-on orientation and increase with inclination, producing up to 0.5 mag. difference for an edge-on galaxy. As already noted from Fig. 1, the derived surface brightness from the exponential fit is always brighter than the corresponding one in the simulated images, due to the flattening of their brightnesses in the central regions.

5.1.2. Sérsic fits to the disk

To quantify the deviation of the simulated images from pure exponentials we also fitted these images with a variable-index general Sérsic function, in order to see if a better fit to the images can be obtained. We followed the same approach as in the previous case, plotting major and minor axis profiles (Fig. 3, upper and middle rows) and generating relative residual maps (lower row, same figure) for various inclinations.

Overall the variable-index Sérsic functions provide better fits to the simulated images at higher inclinations than pure exponentials. Thus, the reduced-χ^2 shows a 63% decrease at an inclination of 73° and a 73% decrease at an inclination of 84°. This is a significant improvement in the goodness of the fit for the inclinations where projection effects play a role. In particular, one can see from the profiles in Fig. 3 that GALFIT tries to mimick the departure from exponentiality in the centre of the disks by fitting the simulated images with a Sérsic index lower than 1. This can also be seen from Fig. 4, where we plotted the inclination dependence of the derived Sérsic index of the fitted disk images. At high inclinations, the best fits correspond to output values for the Sérsic indexes as low as 0.8.

As expected, at lower inclinations Sérsic fits recover the results from pure exponentials, since no projection effects are manifested by face-on disks. Thus, the reduced-χ^2 is similar for exponential and Sérsic fits. For example the reduced-χ^2 shows a 0.0004% decrease at an inclination of 46°. Similarly, the fitted Sérsic index is 1 (exponential) for face-on disks.

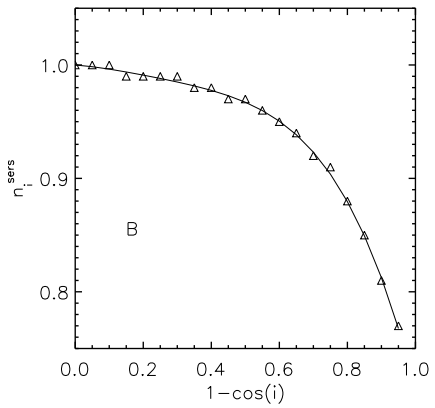

Fig. 4. The inclination dependence of the Sérsic index n_i^{sers} for the dustless images (triangles) of the **disk** in the B band, for the case that the images are **fitted with a general Sérsic function** having n_i^{sers} as a free parameter. The solid line shows the polynomial fit to the measurements.

We fitted the variation of n_i^{sers} index with inclination using a 4th order polynomial (Eq. 14). The fit for the B band is shown by the solid line in Fig. 4, while the coefficients of the fits in all wavebands are listed in Table A.3. By applying Eq. 8 for the specific case of the Sérsic index, we define the departure from exponentiality due to projection effects,

$$\Delta n_i^{sers} = n_i^{sers} - n_0^{sers} \quad (20)$$

where n_0^{sers} is the Sérsic index of the volume stellar emissivity (for disks $n_0^{sers} = 1$; exponential). From the definition, it follows that Δn_i^{sers} varies with inclination from 0 to up to -0.2. Though Sérsic functions provide better fits to the disk images, in particular in the centre and at intermediate distances from the centre, they are poorer fits to the outer disks, where relative residuals can be high (e.g. 35-40% at 84°; see Fig. 3). The reason for this is that the surface brightness distribution in the outer parts is still decreasing according to an exponential distribution, while the fitted distribution - described by a Sérsic index less than 1.0 (mainly determined by the brightest pixels in the centre) is falling faster at large radii, thus underpredicting the luminosity profiles in the outer parts. However, outer disks of galaxies are in real life subject to additional truncation/anti-truncation effects, and may in any case require additional components to be fitted. We therefore conclude that variable index Sérsic functions are better representations of the disk images corresponding to pure exponential distributions of the volume stellar emissivity.

The resulting variation of the derived Sérsic effective radius R_i^{eff} is compared with the corresponding derived exponential scale-length (from an exponential fit) by using the linear transformation $R_i^{eff} = 1.678 R_i$ (which is exact only for $n^{sers} = 1.0$) and by overplotting the variation of the equivalent intrinsic scale-length R_i in Fig. 2, with a red line (left panel). One can see an opposite trend in the two variations. At face-on inclinations both the exponential and the Sérsic fit are identical ($n^{sers} = 1.0$). As the inclination increases the equivalent scale-length of the Sérsic fit decreases with respect to the radial scale-length of the volume stellar emissivity (while the intrinsic exponential scale-length increases). This is due to the decrease in the fitted Sérsic index with increasing inclination, resulting in an equivalent scale-length which is decreasingly smaller and smaller from the $R_i^{eff}/1.678$ transformation. The results of the polynomial fits (Eq. 14) to the $corr^{proj}(R^{eff})$ for all wavebands are listed in Table A.3.

Though the derived effective radius shows a different behaviour with inclination with respect to the exponential fit, the variation in axis ratios seems to be insensitive to whether the fit is done with an exponential or with a variable-index Sérsic function (see Fig. 2, middle panel). In other words the axis ratio seems to be a more robust quantity against projection effects. Irrespectively of the fitting function, the variation with inclination of Q_i only shows the departure from an infinitively thin disk variation, due to the vertical distribution of stars. The $corr^{proj}(Q)$ for the Sérsic fits are thus the same as for the exponential fits and the coefficients of the polynomial fits (Eq. 19) for all wavebands can be found in Table A.2.

Finally, the departure of the fitted central surface brightness from that of the simulated images is minimal in comparison with the exponential fit case (see right hand panel in Fig. 2), another proof that Sérsic fits are better representations of images corresponding to exponential distributions of volume stellar emissivity, especially in the central regions of the disks. The slight overestimation of the central surface brightnesses in the fit as compared to that of the simulations for the high inclinations can be also seen in the radial profiles from Fig. 3. The overall departure of the fit from the simulation is ±0.1 mag, as compared to the 0.5 mag departure in the exponential fit. The coefficients of the polynomial fits (Eq.14) to $corr^{proj}(\Delta SB)$ for all wavebands are listed in Table A.3.

5.2. The Thin Disk

For the thin disk (young stellar disk), the projection effects are insignificant even at very high inclinations. This is due to the different geometry of the young stellar disk, with the ratio between the scale-height and the scale-length of the thin disk being very small (by a factor 60 or so in our model; Tuffs et al. 2004). In other words the approximation of the infinite thin disk is a very good one for this stellar component.

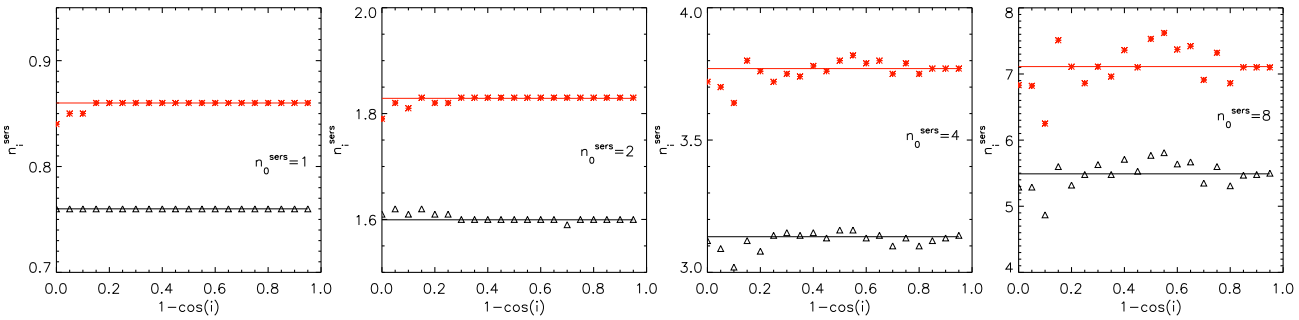

Fig. 5. The derived Sérsic index n_i^{sers} of the dust free images of the **bulge**, for bulges produced with volume stellar emissivities described by (deprojected) Sérsic functions having different Sérsic indexes. The symbols represent the measurements while the solid line are polynomial fits to the measurements. From left to right, the plots correspond to the bulge Sérsic index values $n_0^{sers} = 1.0, 2.0, 4.0, 8.0$. The black curves correspond to bulges truncated at 3 effective radii while the red curves are for bulges truncated at 10 effective radii.

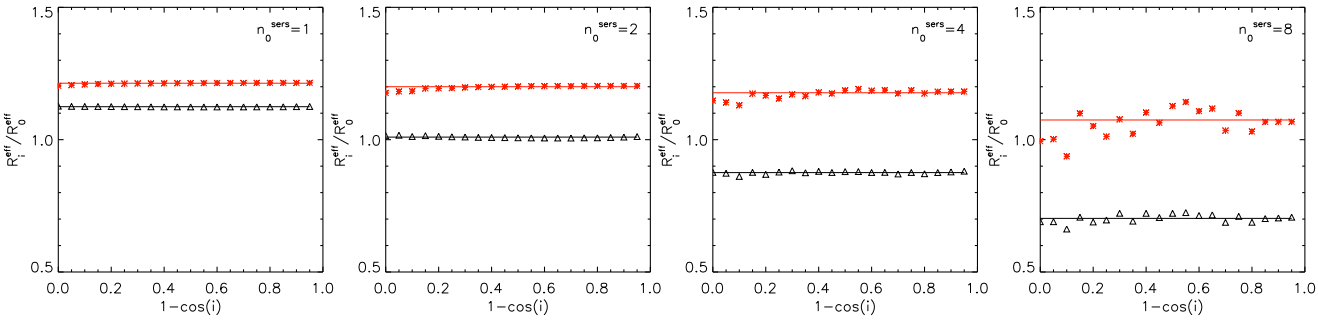

Fig. 6. Projection effects $corr^{proj}$ on the derived effective radius of the **bulge**. The symbols represent the measurements while the solid line are polynomial fits to the measurements. The plots represent the ratio between the intrinsic Sérsic effective radii, R_i^{eff}, and the corresponding volume stellar emissivity, R_0^{eff}. From left to right, the plots correspond to bulges with volume stellar emissivity described by (deprojected) Sérsic functions having Sérsic index values $n_0^{sers} = 1.0, 2.0, 4.0, 8.0$. The black curves correspond to bulges truncated at 3 R_0^{eff} while the red curves are for bulges truncated at 10 R_0^{eff}.

5.3. The Bulge

The problem of projection effects on bulges is very different from that encountered in disks. The difference does not have an intrinsic, physical cause, but originates from the different way astrophysicists use to characterise the distribution of stellar emissivity in these two types of objects, and therefore in the two different ways our simulations are built. In disks the exact mathematical formulation of the stellar emissivity happens at the level of the volume emisivity, where we expect disks to be described by a double exponential, one for the radial distribution and one for the vertical distribution. When projecting this double exponential and fitting the resulting image with a single exponential distribution corresponding to an infinitely thin disk, we will obviously not be able to exactly fit the surface brightness distribution. So this will result in a projection effect. In bulges the situation is reversed. The exact mathematical formulation is for the surface brightness distribution of the images, as given by the Sérsic functions. By construction, the simulations were produced for a volume emissivity that, when projected, at any inclination, will reproduce the Sérsic function for the case of a bulge that extends to infinity. So by construction, the simulations incorporate the projection effects. The caveat is however that this is only true if bulges were to extend to infinity. Since in real life truncations must occur at some distance from the centre (whether this be at a shorter or a longer distance), distortions from the expected Sérsic distributions will occur too. So in our simulations we expect projection effects solely because of the missing light beyond the truncation radius. This would be a constant with inclination, as the missing light will always be the same at any given inclination. It will though strongly depend on the truncation radius, and on the type of Sérsic distribution considered (the Sérsic index).

Since real life bulges can be described by Sérsic functions characterized by different Sérsic indexes, n_0^{sers}, and since real bulges could be either truncated, or could extend to high galactocentric radii (see Maltby et al. 2012) we need to consider all these extra dimensions to the problem. Thus, we produced simulations of bulges with volume stellar emissivity corresponding to (deprojected) Sérsic functions with 4 different values of the Sérsic index $n_0^{sers} = 1, 2, 4, 8$. For each of these the bulges were truncated in the first case at 3 effective radii and in the second one at 10 effective radii. As mentioned in Sect. 2, the truncation at $3R_0^{eff}$ was chosen as this avoids the problem of having a disk-bulge system dominated by the bulge light at high galactocentric radii for large values of the Sérsic index. The truncation at $10R_0^{eff}$ is essentially representative of a bulge with no truncation at all, since at this galactocentric radius almost all the light inside the profile has been accounted for.

The results on projection effects of bulges are calculated using Eq. 8 and 5 for the derived Sérsic indexes and corresponding effective radii, for different types of volume stellar emissivites (n_0^{sers}) and different truncations.

In Fig. 5 we show that, as expected, the derived Sérsic index n_i^{sers} does not depend on inclination. This is true irrespectively of the n_0^{sers} index of the corresponding volume stellar emissiv-

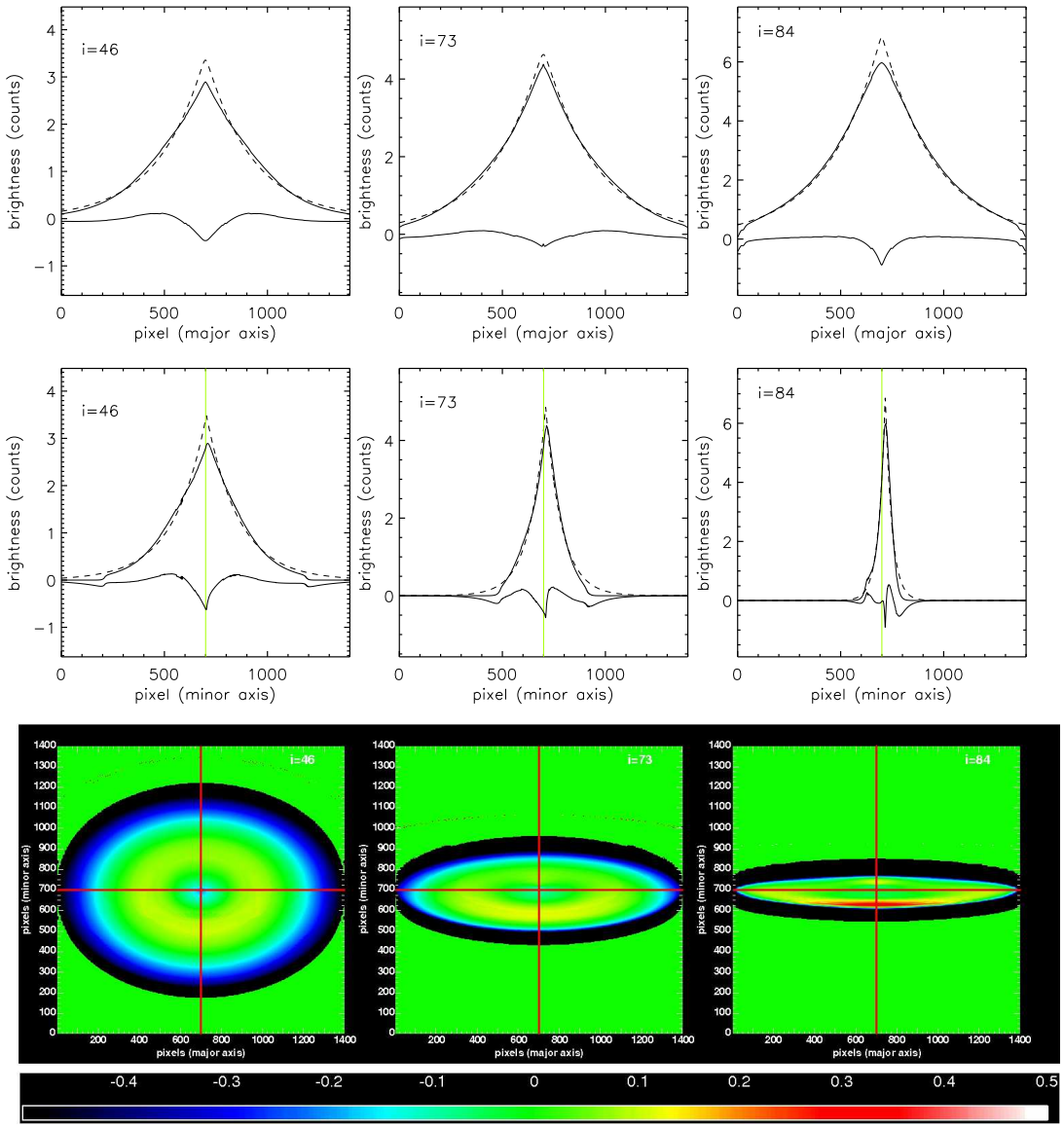

Fig. 7. Major and minor axis **disk** profiles (**upper and middle rows**) showing the deviations from pure exponentials due to the combination of dust and projection effects. Solid upper curves are for **B band** dusty disk images, for $\tau_B^f = 4.0$, dashed curves are for corresponding exponential fits, while absolute residuals ($simulation - fit$) are represented by solid lower curves. The fits were done by letting the geometrical coordinates of the intensity peak as free parameters. The cuts were taken parallel and perpendicular with the major axis of the simulated dusty disk images, through the intensity peaks, at inclinations $1 - \cos(i) = 0.3, 0.7, 0.9$ ($i = 46°, 73°, 84°$). The light green line shows a cut through the geometrical centre of the image. **Lower row**: Corresponding relative residuals ($\frac{simulation-fit}{simulation}$), at the same inclinations and opacity as the profiles. The red lines show radial and vertical cuts through the geometrical centre of the image.

ity and of the truncation radius. For high values of the n_0^{sers} index (n_0^{sers}=8) the constancy of n_i^{sers} with inclination is strongly affected by noise in the measurements. This is not due to any physical effect, but instead is produced by insufficient spatial resolution in the radiative transfer calculations in the inner parts of these bulges. Our simulations were optimised to properly sample the volume emissivity for bulges up to $n_0^{sers} = 4$. For higher values of n_0^{sers}, the steep rise in volume emissivity profiles near the centre would require even finer sampling, which would make these calculations prohibitively time consuming. We believe that for the purpose of this paper the benefit of increasing the resolution in these simulations is limited, and we instead opted to fit all measurements with a 1st order polynomial function (Eq. 14) with a slope equal to zero. The results of the fits are overplotted in Fig. 5 and are listed in Table A.4.

From these results one can also see that the derived Sérsic index is always smaller than the Sérsic index corresponding to the volume stellar emissivity. This is because of the missing light outside the truncation radius. The difference between the Sérsic indexes of the deprojected and projected distribution, Δn_i^{sers} increases (in absolute value) with increasing n_0^{sers}, as seen in Fig. 5, due to the larger variation in the light intensity between the inner and outer radii for large values of n_i^{sers} (more peaky and steep profiles).

For the case of bulges truncated at $10R_0^{eff}$, the fitted values of n_i^{sers} are closer to those of n_0^{sers}, since in this case bulges are

closer to a bulge which has its emissivity extending to infinity (where, as explained before, by construction $n_i^{sers} = n_0^{sers}$).

The constancy of projection effects with inclination is also visible in Fig. 6, for $corr^{proj}(R^{eff})$. As for the case of n_i^{sers}, we fitted the derived ratios with a constant, as listed in Table A.4. Fig. 6 also shows that the derived effective radius of truncated bulges decreases with increasing n_i^{sers}. As expected, the decrease is minimal for bulges truncated at $10R_0^{eff}$. Another aspect that can be noticed from this figure is that for any n_0^{sers} the effective radii for the bulges truncated at $10R_0^{eff}$ are always higher than the ones for the bulges truncated at $3R_0^{eff}$. This happens because in the former case more stellar emissivity will contribute to the corresponding Sérsic distribution than in the latter. Therefore, half of the total stellar emissivity will be enclosed in a larger region for bulges truncated at $10R_0^{eff}$, with a corresponding higher effective radius.

Since in many cases bulges are fitted by observers with de Vaucouleurs functions, we also consider this case, but only for de Vaucouleurs bulges (n_0^{sers}=4) truncated at $3R^{eff}$. The results of the polynomial fits to the n_i^{sers} are given in Table A.5 and are very similar to those obtained using Sérsic functions (for the same n_0^{sers} and truncation radius).

In the following section, when we quantify dust effects for bulges with different Sérsic functions and/or truncation, we apply Eq. 6 and 9, as well as the chain corrections from Eq. 4 and 7, by using dustless and dusty simulations with a common n_0^{sers} and truncation radius.

6. Dust Effects

The quantification of projection effects $corr^{proj}$ allows the subsequent derivation of dust effects $corr^{dust}$. To do this, the simulated dusty images of disks and bulges were fitted, in order to derive the apparent (dust affected) values for the photometric parameters. $corr^{dust}$ were then derived using Eq. 6 and 9, by relating these apparent values of the photometric parameters with the corresponding intrinsic ones, determined from our previous analysis of projection effects. Dust effects were quantified for various values of the central B-band face-on dust optical depth τ_B^f.

In our previous work (Möllenhoff et al. 2006) we did not attempt to disentangle between dust and projection effects, neither did we attempt to analyse the simulations at high inclinations. As we will see in this section, the changes induced by dust in the values of the photometric parameters of spiral galaxies components, $corr^{dust}$, are far more important than projection effects $corr^{proj}$. We present here dust effects for each morphological component and discuss the results.

6.1. The Disk

Dust affects the appearance of the galaxy disks because its opacity is higher in the central parts of the disks, and decreases exponential with radius (e.g. Boissier et al. 2004, Popescu et al. 2005). As a consequence, the central parts of the disks will be more attenuated than the outer parts. This will alter the distribution of stellar emissivity as seen in the absence of dust.

Dust can also induce asymmetries in the surface brightness profiles, at high to edge-on inclinations. This happens because of the difference in the attenuation between the two halves of the disk (separated by the dust disk). At face-on and low inclinations, this effect is negligible, because at each radial position we see the distribution of stellar emissivity through dust columns of same scale-heights. At high inclinations of the disk (seen through the associated dust disk), the half of the disk seen above the dust layer will suffer less attenuation than the half behind it. In addition, anisotropic scattering will also introduce asymmetries, which work in the same direction as the effect of absorption. This results in asymmetric minor axis profiles for inclined disks, with the half of the disk nearest to the observer appearing brighter. These asymmetries cannot be properly taken into account when fitting the images with symmetric analytical functions - exponential distribution and variable index Sérsic function.

Because of these dust-induced asymmetries for the simulated images the position of the intensity peak will generally not coincide with the geometrical center. As a consequence, better fits are provided when the position of the peak intensity is left as a free parameter. The asymmetries induced by dust are particularly visible for higher values of τ_B^f and at higher inclinations.

6.1.1. Exponential fits to the disk

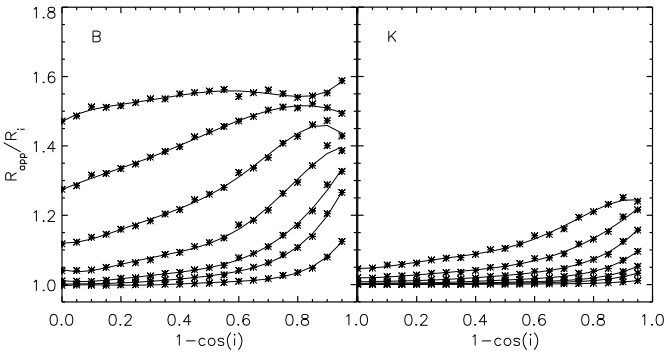

Fig. 8. Dust effects $corr^{dust}$ on the derived scale-length of **disks fitted with exponential functions**. The symbols represent the measurements while the solid line are polynomial fits to the measurements. The plots represent the ratio between the apparent and intrinsic scale-lengths R_{app} and R_i respectively, as a function of inclination $(1 - \cos(i))$, for B and K optical bands. From bottom to top, the curves are plotted for τ_B^f = 0.1, 0.3, 0.5, 1.0, 2.0, 4.0, 8.0.

When fitting disks with exponential functions a main problem is, as mentioned before, the appearance of dust-induced asymmetries at higher values of τ_B^f and i. A good illustration of this effect can be seen from the minor axis profiles in Fig. 7 (middle row, for $\tau_B^f = 4.0$ case), where the position of the intensity peak is shifted with respect to the position of the geometrical centre, marked by the light green line. Also, in the corresponding residual maps on the lower row of Fig. 7 one can notice asymmetric residuals. For example, at 73° inclination the fit underpredicts the lower half of the simulated image with 10-15% (see the yellow lower feature in the residual maps) while at 84°, the residuals are as high as 30-35% (the lower yellow-red feature from Fig. 7; see also the minor axis profiles from the same figure, middle row, right panel).

It is also interesting to note that the residual maps exhibit a ring-like structure at intermediate inclinations (see the yellow ring in the middle row, left panel of Fig. 7). This feature appears because the fit underpredicts the simulated dusty images at intermediate radii (see also the left column of plots in Fig. 7) (first

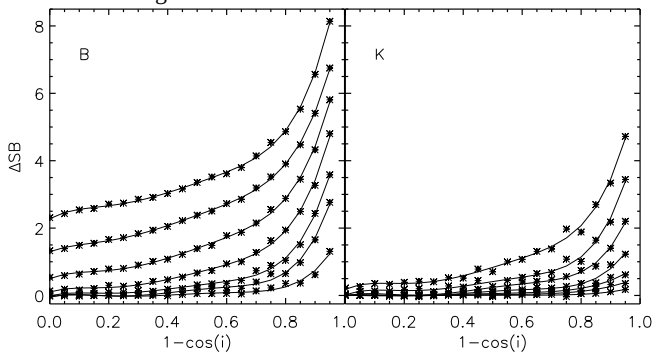

Fig. 9. Dust effects $corr^{dust}$ on the derived central surface brightnesses of **disks fitted with exponential functions**. The symbols represent the measurements while the solid line are polynomial fits to the measurements. The plots represent the ratio between the apparent and intrinsic average central surface-brightness, ΔSB, expressed in magnitudes, versus inclination $(1 - \cos(i))$, for B and K optical bands. From bottom to top, the curves are plotted for $\tau_B^f = 0.1, 0.3, 0.5, 1.0, 2.0, 4.0, 8.0$.

two rows), where both the fit and the simulated image contain only smooth (diffuse) distributions of stellar emissivity. In other words, dust can induce feature-like structures in the residual maps which have no connection with real structures like rings, spiral arms or clumpiness. In view of the fact that it is common practice to use residual maps in observations of galaxies to assess the degree of clumpiness of an object, or even to assess the morphological type (spiral type), we caution that the reliability of the method is limited due to the above mentioned dust effects.

Fig. 8 shows the inclination dependence of the ratio between the apparent and intrinsic scale-lengths ($corr^{dust}(R)$; Eq 6), for different values of the central face-on optical depth, τ_B^f. As previously found (e.g. Möllenhoff et al. 2006), the scale-length ratios increase with opacity and are always greater than 1. As noticed before from Fig. 7, this is due to the dust-induced flattening of the intrinsic stellar emissivity profiles. An additional feature of the plots for the B band is that, for low values of τ_B^f, there is a monotonic increase in scale-length with inclination, while at high opacities, when the disk becomes optically thick along all lines of sight, the increase flattens asymptotically (Fig. 8, left panel; see also Möllenhoff et al. 2006). However, this is not the case for the K band, where even at high τ_B^f we see a monotonic increase in scale-length ratios with inclination (Fig. 8, right panel). This is because in the K band the disk is still optically thin along most of the lines of sight, at all inclinations. The results of the polynomial fits (Eq. 14) to $corr^{dust}(R)$, for all opacities considered, are listed in Tables B.1, B.2, B.3, B.4, B.5 for the B,V,I,J,K bands.

Fig. 9 shows the inclination dependence of the ratio between the apparent and intrinsic average central surface-brightness, expressed in magnitudes $\Delta SB = -2.5 log(F_{app}/F_i)$ ($corr^{dust}(SB)$; Eq. 9). As already noted in Sect. 5, these are calculated as averages in elliptical apertures. F_{app} was calculated as an average over an elliptical aperture centred on the position of the geometrical centre of the fitted dusty images, with a semi-major axis of $R_{app}/10$ and an axis-ratio of Q_{app}

The surface brightness ratios are always positive at any inclination and for all values of τ_B^f, meaning the apparent average central surface brightnesses are always fainter than the intrinsic ones. At high opacities, and close to edge-on inclinations, when the lines of sight pass through the longest columns of dust, the attenuation of central surface brightness is very strong (up to 8 mag for the B band and up to 5 mag for the K band at $\tau_B^f = 8.0$). As with $corr^{dust}(R)$, the results of the polynomial fits (Eq. 14) to $corr^{dust}(\Delta SB)$ for all opacities considered, are given in Tables B.1, B.2, B.3, B.4, B.5 for the B,V,I,J,K bands.

The change in the disk axis-ratio due to dust ($corr^{dust}(Q)$; Eq. 6) has been fitted by a combination of two polynomials, of the form:

$$corr(x) = \begin{cases} a_0 & \text{for } 0 \le x \le x_1 \\ b_0 + b_1\, x_1 & \text{for } x_1 \le x \le 0.95 \end{cases} \quad (21)$$

where $x = 1 - \cos(i)$ and $x_1 = 0.95$ for $\tau_B^f = 0.1, 0.3$, $x_1 = 0.90$ for $\tau_B^f = 0.5, 1.0, 2.0$ and $x_1 = 0.65$ for $\tau_B^f = 4.0, 8.0$. At low to intermediate inclinations, up to $1 - cos(i) = 0.65$, the derived axis-ratio in the presence of dust, Q_{app}, is the same as the intrinsic axis-ratio, Q_i, which, in turn, is the same as the axis ratio of the infinitely thin disk, $Q_0 = cos(i)$. It is only at higher inclinations and higher dust opacities that the dust starts to affect the derived axis-ratios, in the sense that the measured ratios are lower than the corresponding intrinsic values. This means that dust makes disks appear slightly thinner than they are in reality. Nonetheless, even at higher inclinations and dust opacities, the effects due to dust, $corr^{dust}(Q)$, are smaller than projection effects, $corr^{proj}(Q)$. Thus, the decrease in the axis ratio due to dust is at most 10%, while the increase in the intrinsic axis-ratio with respect to the axis-ratio of the infinitely thin disk is up to 50%. Overall, the correction from the $cos(i)$ term is dominated by the increase in the axis ratio due to the vertical distribution of stars. The resulting coefficients of the polynomial fits to $corr^{dust}(Q)$ are given for all opacities considered, in Tables B.6, B.7, B.8, B.9, B.10 for B,V,I,J,K bands.

6.1.2. Sérsic fits to the disk

As with projection effects, to quantify the deviations of the simulated images from pure exponentials we also fitted the dusty disk images with general Sérsic functions. The corresponding major and minor axis profiles for $\tau_B^f = 4.0$ (as displayed in the upper and middle rows of Fig. 10 at three inclinations) show that overall general Sérsic functions are a better representation of the dusty disks. This can also be noticed from the the residual maps (same figure, lower row) where the residuals are very low at most inclinations and radii. A reduced-χ^2 test for the case presented in Fig. 10 (B band and $\tau_B^f = 4.0$) shows a decrease of 94% at an inclination of 46° with respect to the exponential case. However, at higher inclinations the dust-induced asymmetries still remain, as both Sérsic and exponential are symmetric distributions. Correspondingly, the reduced-χ^2 shows a decreasingly improvement in the goodness of the fit with increasing inclination, between the exponential and the Sérsic fit. Thus, the improvement in the goodness of the fit is only 42% for $i = 73°$ and reaches 1.9% at $i = 84°$.

The general trend for the derived Sérsic index is to decrease from the value $n_0^{sers} = 1.0$ (characteristic for an exponential distribution) with the increase of τ_B^f and inclination, for lower values of τ_B^f (see Fig. 11, left panels). This comes as a result of the flattening in the central regions due to the higher attenuation at small galactocentric radii. For higher τ_B^f values the trend reverts, with n_{app}^{sers} now increasing with inclination (see in particular the blue and red curves in the left panels from Fig. 11). This non-monotonic behaviour is caused by the fact that for larger τ_B^f the

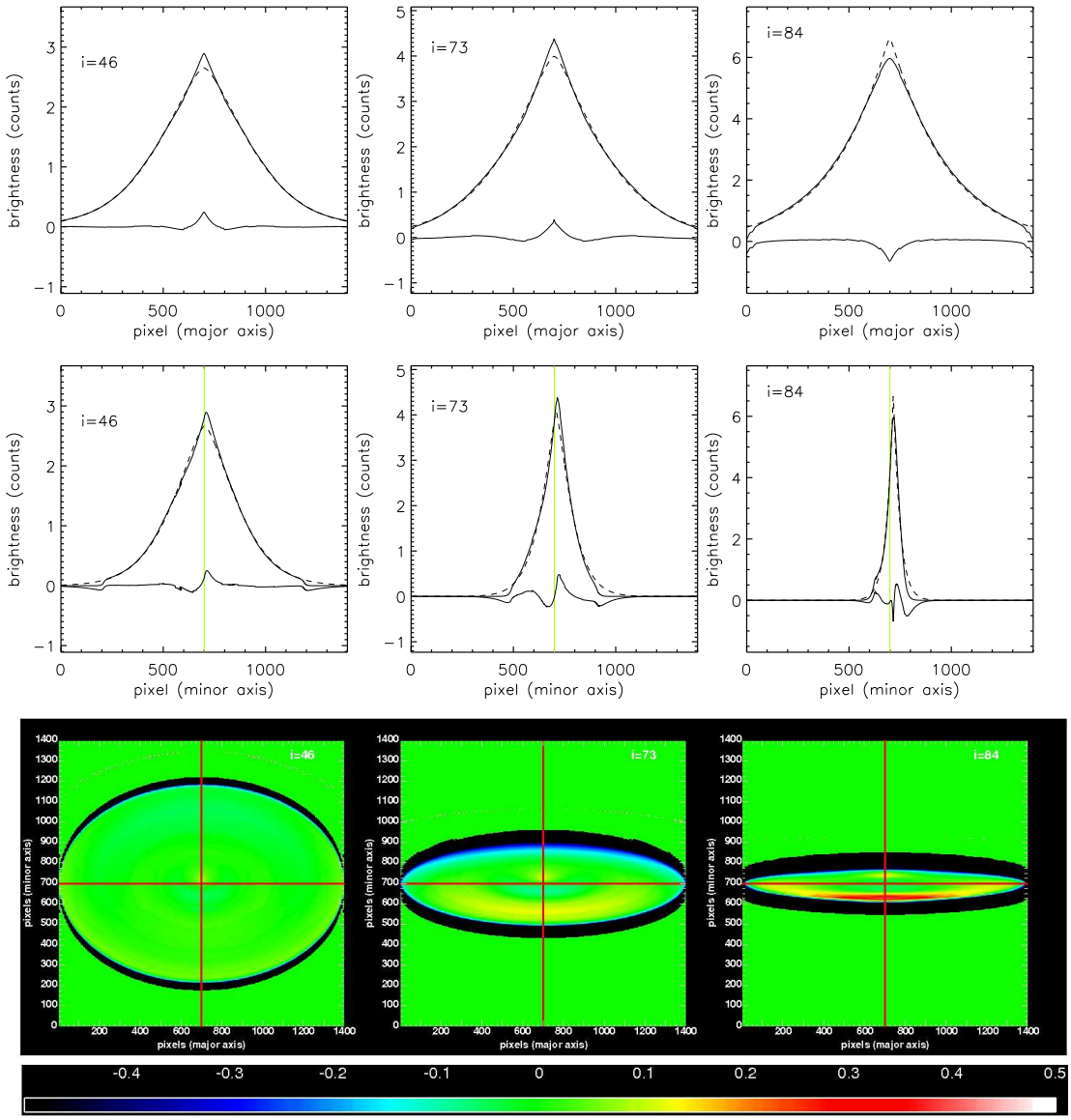

Fig. 10. Major and minor axis **disk** profiles (**upper and middle rows**) showing the deviations from a general Sersic profile due to the combination of dust and projection effects. Solid upper curves are for **B band** dusty disk images, for $\tau_B^f = 4.0$, dashed curves are for corresponding Sérsic fits, while absolute residuals ($simulation - fit$) are represented by solid lower curves. The fits were done by letting the geometrical coordinates of the intensity peak as free parameters. The cuts were taken parallel and perpendicular with the major axis of the simulated dusty disk images, through their intensity peaks, at inclinations $1 - \cos(i) = 0.3, 0.7, 0.9$ ($i = 46°, 73°, 84°$). The light green line shows a cut through the geometrical centre of the image. **Lower row**: Corresponding relative residuals ($\frac{simulation-fit}{simulation}$), at the same inclinations and opacity as the profiles. The red lines show radial and vertical cuts through the geometrical centre of the image.

optical thick core increases in size, moving outwards towards large radii, flattening thus the profile amongst larger and larger radii. This will eventually revert to an exponential. The results of the polynomial fits to the n_{app}^{sers}, for all opacities considered, are listed in Tables B.11, B.12, B.13, B.14, B.15 for the B,V,I,J,K bands.

Since the trends seen in the plots for n_{app}^{sers} are due to both dust and projection effects, we correct for the latter by subtracting $corr^{proj}(n^{sers}) = \Delta n_i^{sers}$ - the corrections defined in Section 4.2, to the derived values of n_{app}^{sers}. The results are plotted in the right panels of Fig. 11. It is reasurring to notice that in the K band, after correcting for projection effects, we recover the intrinsic value of 1 for the Sérsic index, for all inclinations except the edge-on ones, and for most values of dust opacities, except for the very high ones. It is also noticeable that at low inclinations the deviations from exponentiality are mainly due to dust effects while at higher inclinations, both dust and projection effects affect the derived Sérsic index. The resulting effective radius will always be larger than the corresponding one in the absence of dust, with the ratio of these two increasing with inclination, as noticed from Fig. 12. The coefficients of the polynomial fits are listed in the same tables as the n_{app}^{sers}.

The effects of dust on the derived axis ratios Q_{app}/Q_i are the same for the Sérsic and exponential fits, so the results are only listed once in the tables corresponding to the exponential fits.

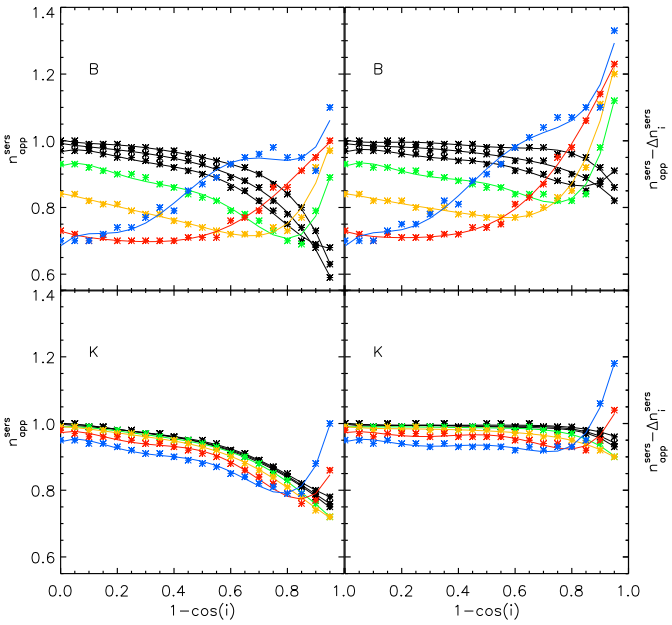

Fig. 11. Left panels: the inclination dependence of the derived Sérsic index for **disks fitted with Sérsic functions**, due to combined dust and projection effects. The symbols represent the measurements while the solid line are polynomial fits to the measurements. **Right panels**: The same but corrected for projection effects (Δn_i^{sers}). Upper panels are for the B band and lower panels are for the K band. From top to bottom, the curves are plotted for τ_B^f=0.1, 0.3, 0.5 (black), 1.0 (green), 2.0 (orange), 4.0 (blue) and 8.0 (red).

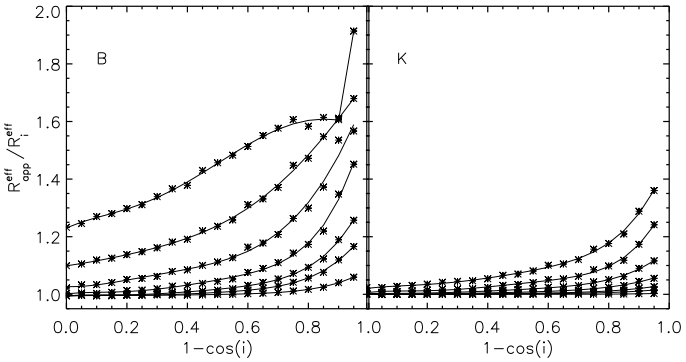

Fig. 12. Dust effects $corr^{dust}$ on the derived effective radius of **disks fitted with Sérsic functions**. The symbols represent the measurements while the solid line are polynomial fits to the measurements. The plots represent the ratio between the apparent and intrinsic Sérsic effective radii, R_{app}^{eff} and R_i^{eff} respectively, as a function of inclination (1 − cos(i)), for B and K optical bands. From bottom to top, the curves are plotted for τ_B^f = 0.1, 0.3, 0.5, 1.0, 2.0, 4.0, 8.0.

6.2. The Thin Disk

The dust affects the perceived distribution of stellar emissivity in the young stellar disk in a stronger way than in the old stellar disk, as we will see in this section, although the overall trend is similar. This is because the young stellar disk is, in our model, completely embedded in the dust distribution, and therefore suffers more attenuation effects than the old stellar disk. By contrast, as already noted in Sect. 5.2, projection effects are negligible for the thin disk, and therefore can be safely ignored.

The main application of our dust corrections on the derived photometric parameters of thin disks are for the UV range, as it is in this spectral range that the young stellar disk is prominent. In the optical range, the young stellar disk cannot be disentangled from the old stellar disk, based on optical images alone. Therefore, in the optical, the measured structural parameters are indicative of the old stellar disk. In analysing optical images of galaxies it is recommended to use dust corrections for the "disk" component. We nevertheless quantify dust corrections in the optical for the "thin disk" as well, as these are useful for deriving corrections for Balmer line/nebular line emission. Dust corrections on line emission can be derived by interpolating between the optical wavelength tabulated in this paper. As an example we only show dust corrections for the Hα line emission.

6.2.1. Exponential fits to the thin disk

In Fig. 13, we show major axis profiles for the dusty young stellar disk images, for two UV bands, at face-on inclination. One can see that for intermediate values of the optical depth, even at face-on inclinations the profiles deviate from pure exponentials, as dust strongly alters the shape of the profile, making it extremely flat in the central part (see the third column plots in Fig. 13). In the central regions we can also observe high residuals between the simulated and the fitted profiles, another indication that the fits are imperfect. With increasing opacity and inclinations, the fits become more imperfect. At a certain point, exponential fits become completely inadequate to represent the surface-brightness distribution of thin disks. For this reason, we present here dust effects only at inclinations and opacity values for which an exponential profile is still a good representation of the stellar emissivity distribution in the young stellar disk. For example, in the UV range we present corrections only up to a dust opacity of $\tau_B^f = 2$.

Fig. 14 shows the inclination dependence of the ratio between the apparent and intrinsic scale-lengths of the thin disk ($corr^{dust}(R)$; Eq. 6), for different values of the B band central face-on optical depth, τ_B^f, for various UV wavelengths. As we can observe from these plots, the strongest distortion dust exerts over the stellar emissivity distribution is, as expected, at the shortest UV wavelengths. The dust effects decrease non-monotonically with increasing UV wavelength, due to the bump in the extinction curve at 2200 Å. Overall, the dust effects are quite severe for this morphological component in particular in the UV range.

But even in the optical range the thin disk is strongly affected by dust. This can be seen in Fig. 15, where we plotted the same quantities as in Fig. 14, this time for the longer optical wavelengths. The strong dust effects are due to the fact that, as mentioned before, the young stellar disk has a smaller scale-height than the old stellar disk, and therefore it has a stronger spatial coupling with the dust. By making a comparison between Fig. 8 on one hand (old stellar disk), and Fig. 15 (young stellar disk) on the other hand, one can see that, for the same wavelength and τ_B^f, the amplitude of the changes in the apparent scale-lengths is higher for the young stellar disk. We notice however that the trend is similar for both stellar components.

In addition to the continuum optical emission we also show an example for the $H\alpha$ line (Fig. 15), as it is the young stellar disk component from where the recombination lines originate (the star forming regions). For other Balmer lines dust correc-

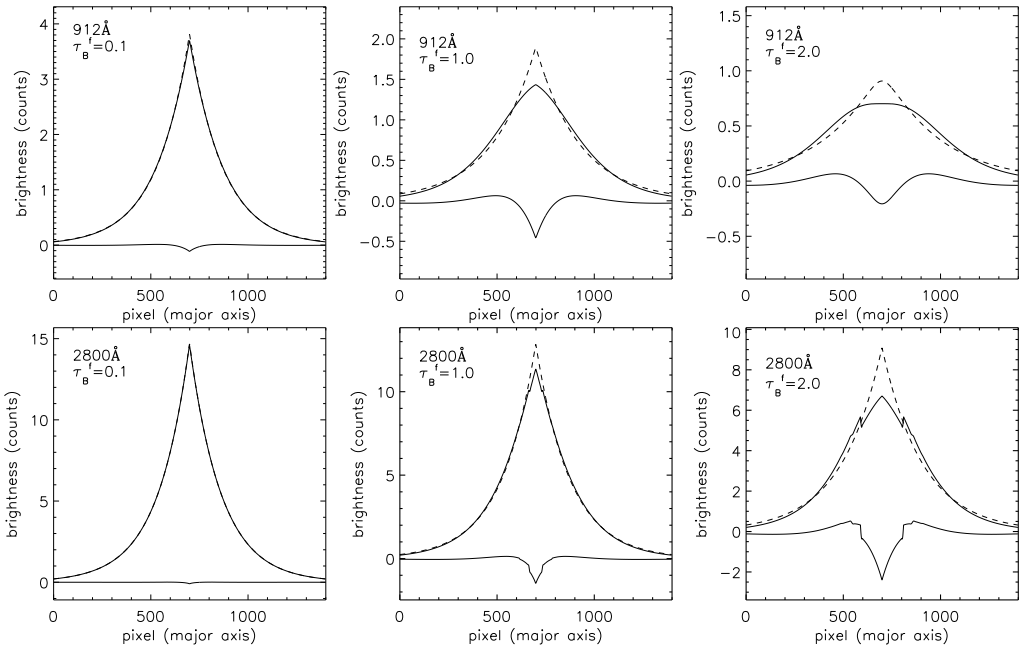

Fig. 13. The face-on major axis profiles for the **thin disk** showing the deviations from pure exponentials due to dust effects. Solid upper curves are for the face-on dusty images, the corresponding exponential fits are represented by dashed curves, while the solid lower curves are for residuals. The upper row of plots corresponds to the 912 Å UV wavelength and $\tau_B^f = 0.1, 1.0, 2.0$ (from left to right), while the lower row of plots corresponds to the 2800 Å UV wavelength and same values of τ_B^f. The fits were done by letting the geometrical coordinates of the intensity peak as free parameters. The cuts were taken parallel and perpendicular with the major axis of the thin disk dusty images, through their intensity peaks.

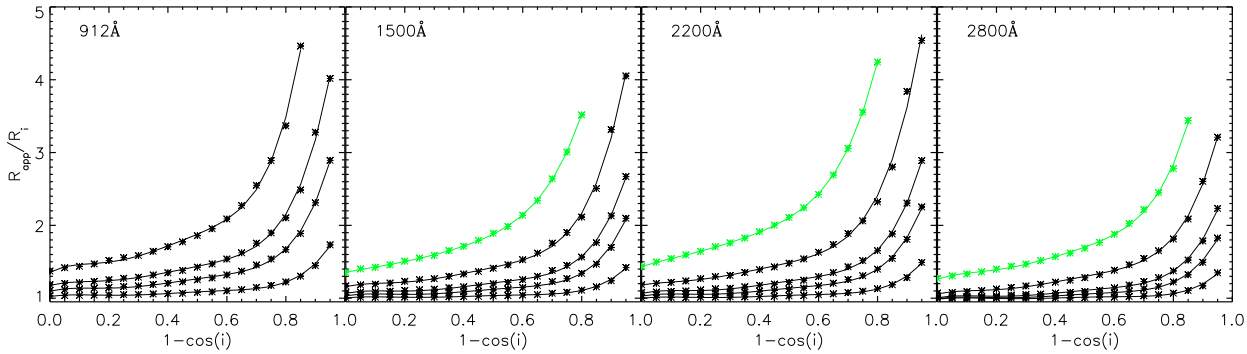

Fig. 14. Dust effects $corr^{dust}$ on the derived scale-length of **thin disks fitted with exponential functions**. The symbols represent the measurements while the solid line are polynomial fits to the measurements. The plots represent the inclination dependence of the ratio between the apparent and intrinsic scale-lengths, R_{app} and R_i respectively. From left to right, the plots corresponds to increasing UV wavelengths: 912 Å, 1500 Å, 2200 Å and 2800 Å. From bottom to top the black curves are plotted for $\tau_B^f = 0.1, 0.3, 0.5, 1.0$. The green curve corresponds to $\tau_B^f = 2.0$.

tions can be obtained by interpolating the corrections for the thin disk between the relevant optical wavelengths. All the corrections $corr^{dust}$, both in the UV range and in the optical, including for the $H\alpha$ line are listed in terms of coefficients of polynomial fits in Tables B.16, B.17, B.18, B.19, B.20, B.21, B.22, B.23, B.24, B.25, B.26, B.27, B.28, B.29, B.30.

6.2.2. Sérsic fits to the thin disk

As in the case of the old stellar disk, in order to quantify the deviations of the stellar emissivity profiles from pure exponentials we also performed Sérsic fits for the thin disk images. In Fig. 16 we present the inclination dependence of the derived Sérsic index (upper row) and the Sérsic effective radii ratios (lower row), for the same UV wavelengths chosen when fitting with an exponential. Even for low values of τ_B^f, at high inclinations the effects of dust are important and increase towards shorter wavelengths. At higher values of τ_B^f the deviations of the derived Sérsic indexes from its exponential value can be dramatic, with values going down to $n_{app}^{sers} = 0.5$ (gaussian) or even lower, to $n_{app}^{sers} \approxeq 0.1$. Since there are no significant projection effects ($\Delta n_i^{sers} \approxeq 0$) for the thin disk (as mentioned in Sect. 4.2), the deviations of the Sérsic index from an exponential are in this case caused only by the dust effects. At high inclinations and for extremely opaque thin disks even Sérsic fits become poor representations of the profiles, therefore these cases were omitted from the plots in Fig. 16.

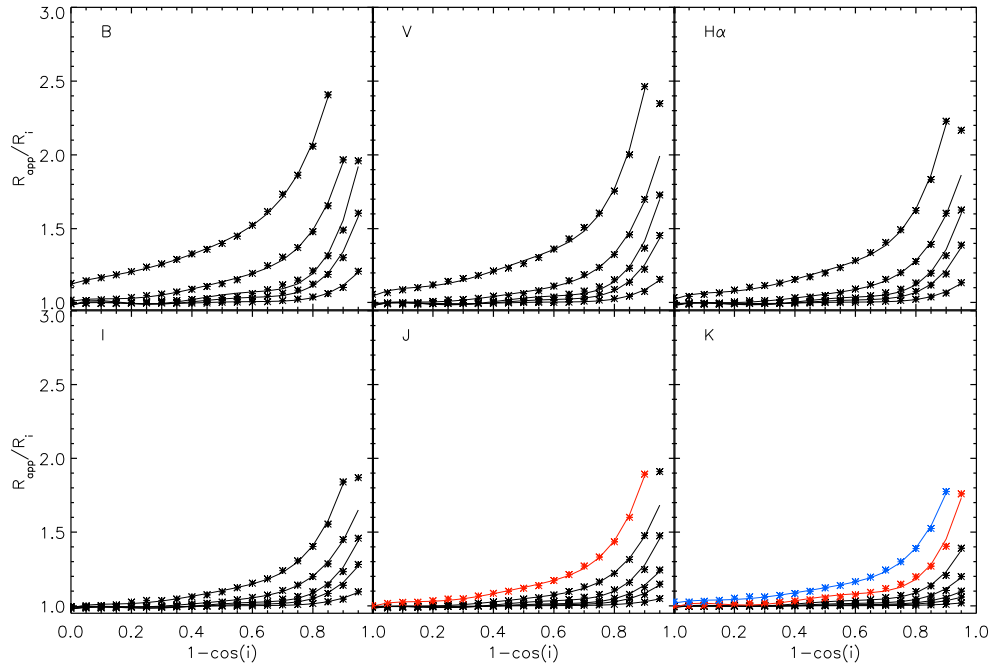

Fig. 15. Same as in Fig. 14, for the optical bands and the $H\alpha$ line. From bottom to top the black curves are plotted for $\tau_B^f = 0.1, 0.3, 0.5, 1.0, 2.0$. The red curve corresponds to $\tau_B^f = 4.0$, while the blue one is for $\tau_B^f = 8.0$.

In the optical range we proceeded in a similar way to the UV range, by fitting variable Sérsic index functions to the simulated images of the young stellar disk. In Figs. 17 and 18 we display the corresponding Sérsic index and effective radii ratios variation as a function of inclination for various optical bands and also for the $H\alpha$ line. By comparing the derived Sérsic indexes for the old stellar disk (Fig. 11, right hand panel) and the young stellar disk (Fig. 17), at the same wavelength, τ_B^f and inclination we notice that the dust-induced changes in the derived Sérsic index are higher in the latter case. We also see that for high values of τ_B^f ($\tau_B^f = 4.0, 8.0$) the trend for the two morphological components is not the same. Thus, for the old stellar disk the derived Sérsic index increases with increasing inclination, while for the young stellar disk an opposite trend is observed.

Our analysis of the dust effects on the derived thin disk axis-ratios ($corr^{dust}(Q)$; Eq. 6) shows that these are negligible, therefore we do not present these. All the other results on $corr^{dust}$, both in the UV and in the optical range, including the $H\alpha$ line are listed in terms of coefficients of polynomial fits in Tables B.31, B.32, B.33, B.34, B.35, B.36, B.37, B.38, B.39, B.40, B.41, B.42, B.43, B.44, B.45.

6.3. The Bulge

The analysis on the effect of dust on bulges is the most novel aspect of this study, as, unlike disks, there is very little work based on radiation transfer simulations on this topic. As for the case of dustless bulges, we used simulations of dusty bulges with volume stellar emissivity distributions described by various Sérsic indexes, $n_0^{sersic} = 1, 2, 4, 8$. Accordingly, for each of these cases we used as fitting functions variable-index Sérsic distributions. For the case of $n_0^{sersic} = 4$ we also used de Vaucoulers functions to fit the simulations. We considered both simulations for bulges truncated at 3 and 10 effective radii, respectively.

We have already seen in Sect. 5.3 that projection effects $corr^{proj}$ on bulges strongly depend on the intrinsic Sérsic index of the volume stellar emissivity n_0^{sers}, and on the existence or not of a truncation radius. So it is important to assess whether dust effects $corr^{dust}$ also have these extra dimensions in parameter space.

We first tested whether the corrections depend on the choice of the Sérsic index used as input in the simulations (n_0^{sers}). To do this we analysed bulges produced with 4 different values of the Sérsic indexes, $n_0^{sersic} = 1, 2, 4, 8$, for the same $\tau_B^f = 1.0$, for bulges truncated at $3R_0^{eff}$, and at different inclinations. Subsequently, we fitted these bulges with variable-index Sérsic functions. The variation of the derived Sérsic indexes with inclination is displayed in Fig. 19. After correcting for projection effects (right panel in Fig. 19), we see that for low to intermediate inclinations the variation of the derived Sérsic index (n_{app}^{sers}) with inclination does not depend on the input Sérsic index in the simulation, n_0^{sers}. In particular for this value of τ_B^f, we broadly recover the values of the parameter n_0^{sers}. It is only for high value of n_0^{sers} and closer to edge-on inclinations that the measured Sérsic index starts to drop significantly from its intrinsic value. As mentioned in Sect. 5.3 the noisier curves at $n_0^{sers} = 8$ are not due to real physical effects, but are inherent to the limited resolution of our radiative transfer calculations for this high value of Sérsic index. As a result of these tests done for simulations with different n_0^{sers}, we decided that, because the differences are small, to only consider dust effects for two different values of the Sérsic index, $n_0^{sers} = 1.0$ (exponential bulge) and $n_0^{sers} = 4.0$ (de Vaucouleurs bulge).

Secondly we tested whether truncation radius affects dust corrections $corr^{dust}$. In Fig. 20 we show the effect of dust for bulges truncated at $3\,R^{eff}$ and at $10\,R^{eff}$, for two values of τ_B^f. This test indicates that, unlike for the projection effects, truncation radius does not affect the results on dust effects. Therefore there was no need to present our dust corrections as a function of truncation radius.

When performing the fit to simulations, one of the main problems was related to the dust-induced asymmetries in the sur-

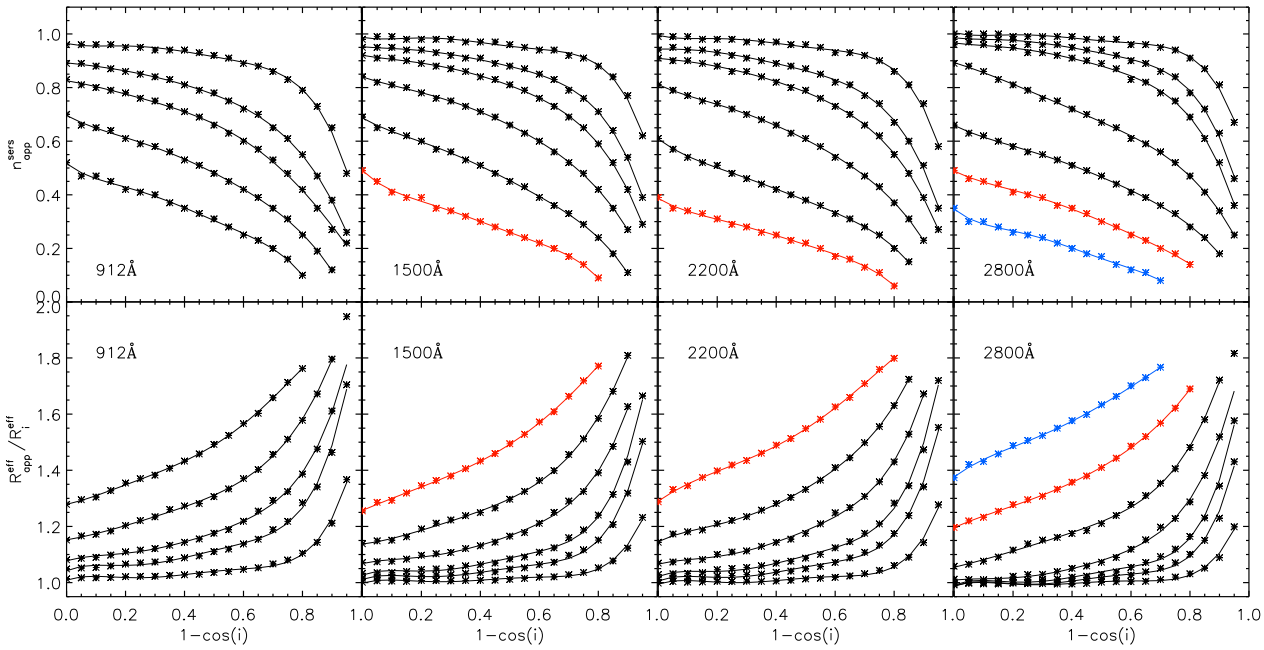

Fig. 16. Upper row: the inclination dependence of the derived Sérsic index for the dusty images of **thin disks fitted with Sérsic functions**. **Lower row**: same, for the ratio between the apparent and intrinsic Sérsic effective radii, R^{eff}_{app} and R^{eff}_{i} respectively. The symbols represent the measurements while the solid line are polynomial fits to the measurements. From left to right, the plots corresponds to increasing UV wavelengths: 912 Å, 1500 Å, 2200 Å and 2800 Å. The black curves are plotted for $\tau^f_B = 0.1, 0.3, 0.5, 1.0, 2.0$ (from top to bottom, in this order for the upper row and in reverse order for the lower row). The red curve corresponds to $\tau^f_B = 4.0$, while the blue one is for $\tau^f_B = 8.0$.

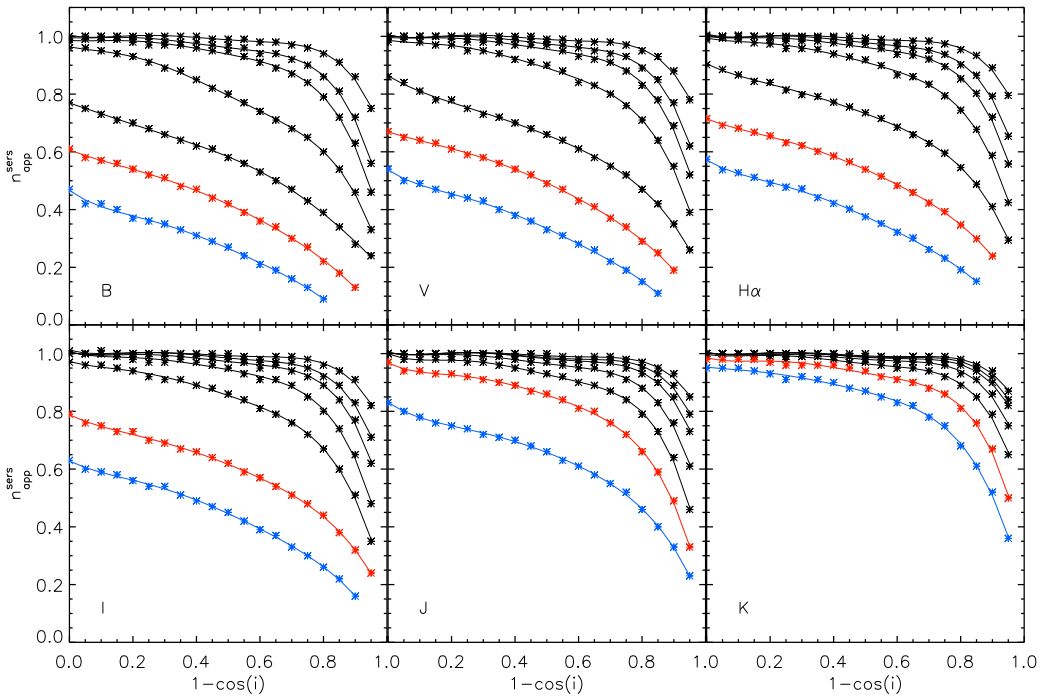

Fig. 17. Same as in Fig. 16 top, for the the optical bands and the $H\alpha$ line.

face brightness distribution profiles at high inclinations (of the dust disk) and large values of τ^f_B. As an illustration of this effect we show in Fig. 21 two dusty bulge simulated images, one at 73° inclination (left) and one edge-on (right). We can easily notice from the image on the left, that a bulge observed in the B band, at 73° inclination, for $\tau^f_B = 4.0$, would have half of its image obscured by dust. This issue produces difficulties when fitting such images with a symmetrical analytic function like a Sérsic distribution. Similar problems can arise for bulges seen at edge-on inclinations, where the dust lanes block the bulge stellar

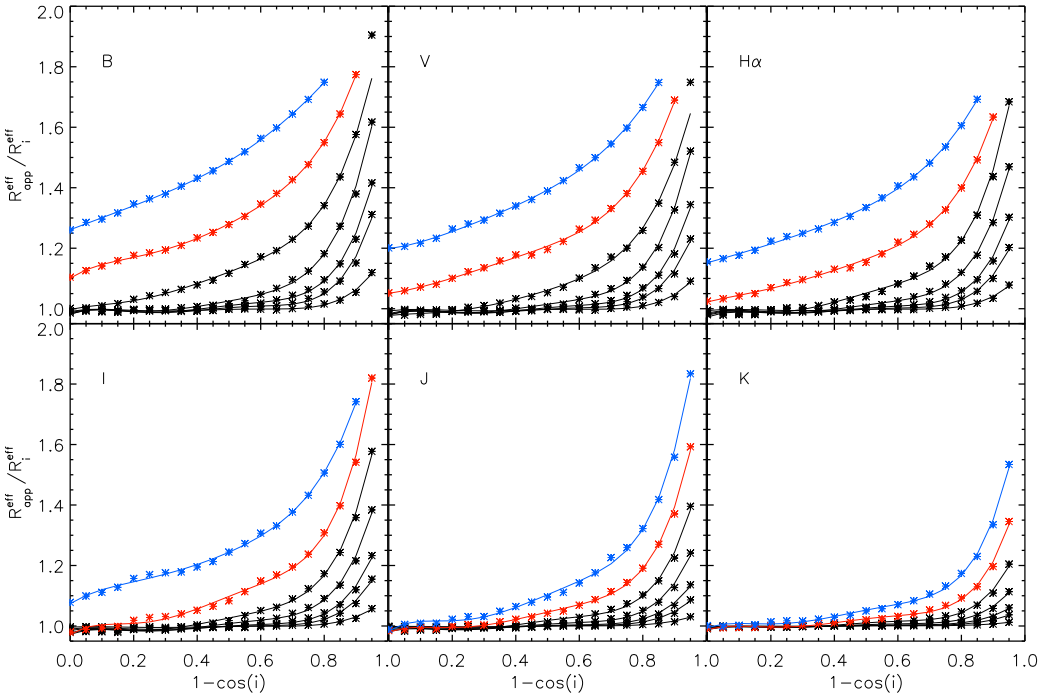

Fig. 18. Same as in Fig. 16 bottom, for the the optical bands and the $H\alpha$ line.

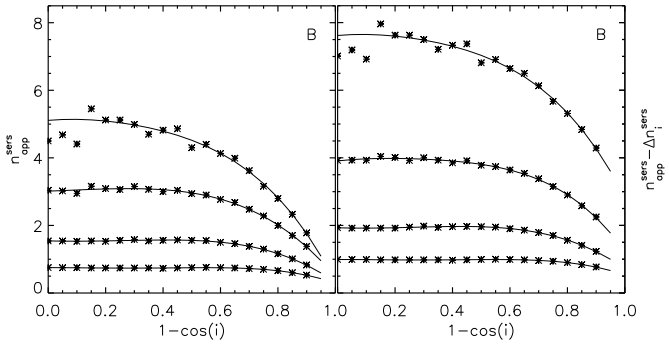

Fig. 19. Left: The inclination dependence of the derived Sérsic index of **bulges** due to combined dust and projection effects, in B band, for simulations having the volume stellar emissivity described by different Sérsic index, $n_0^{sersic} = 1, 2, 4, 8$ (from bottom to top curve), and $\tau_B^f = 1.0$. The symbols represent the measurements while the solid line are polynomial fits to the measurements. **Right**: The same but corrected for projection effects (Δn_i^{sers}).

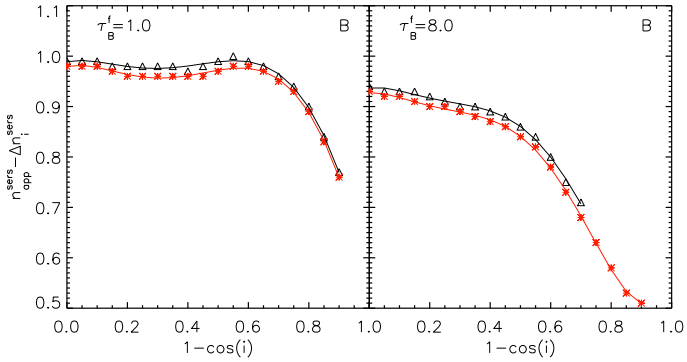

Fig. 20. The inclination dependence of the derived Sérsic index of **bulges** due to dust effects only (corrected for projection effects), for bulges truncated at 3 effective radii (black curves) and at 10 effective radii (red curves). The symbols represent the measurements while the solid line are polynomial fits to the measurements. Results are for the B band and for simulations corresponding to volume stellar emissivity described by a (deprojected) Sérsic function with $n_0^{sers} = 1$. Left panel is for τ_B^f=1 and right panel is for τ_B^f=8.

emissivity in the plane of the disk [3] (see right panel of Fig. 21 for an edge-on orientation). For this reason it is not feasible to do Sérsic fits for bulges at high inclinations and high τ_B^f.

To quantify the dust effects on the bulge photometric parameters, we fitted both exponential ($n_0^{sersic} = 1$) and de Vaucouleurs ($n_0^{sersic} = 4$) bulges with variable-index Sérsic functions. We plotted the inclination dependence of the Sérsic index only for the values of τ_B^f and at inclinations for which the derived fit was reasonable. The combined dust and projection effects on the Sérsic index of exponential bulges can be seen in the left panels from Fig. 22, for B and K bands. For large values of τ_B^f the distortions in the derived Sérsic index are strong, with observed trends looking similar, and with n_{app}^{sersic} decreasing with inclination and τ_B^f. For example, for $\tau_B^f = 4.0$, $i = 78°$, n_{app}^{sersic} decreases to 0.45. The decrease of the measured Sérsic index of bulges with increasing opacity and inclination has also been found by Gadotti et al. (2010), though a direct comparison is not possible, since the latter trends were derived from bulges obtained from bulge/disk decomposition, which, beside the effects of dust also contain the effect of dust on the bulge/disk decomposition itself, what we call in this paper $corr^{B/D}$, as given by Eq. 12 and 13.

Since the trends seen in our plots for n_{app}^{sersic} of exponential bulges are due to both dust and projection effects, we correct

[3] We remind the reader that no disk stellar emissivity is included in these simulations

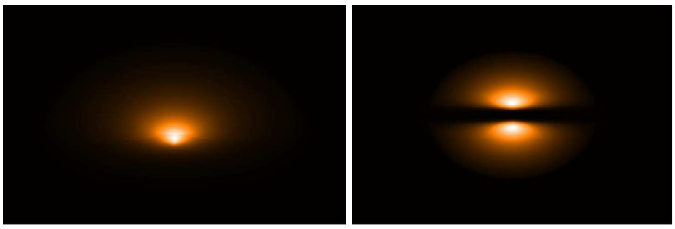

Fig. 21. Left: Simulated image of a **bulge** in the B band, seen through the dust disks, having $\tau_B^f = 4.0$, and inclined at $i = 73°$. **Right**: Same for $\tau_B^f = 1.0$ and $i = 90°$. In both cases, no stellar emissivity is included in the disk - pure bulge case.

for the latter by subtracting Δn_i^{sers} - the corrections defined in Sections 4.1 and 4.3, to the derived values of n_{app}^{sers}. The results are plotted in the right panels of Fig. 22. The derived values of Sérsic index are now closer to the values of the n_0^{sersic} parameter input in the simulations. At very high inclinations and large values of τ_B^f the deviations in the B band are still very important. The plots also show that at all inclinations the deviations from the intrinsic distributions are due to both dust and projection effects, with projection effects being constant with inclination (see Fig. 5).

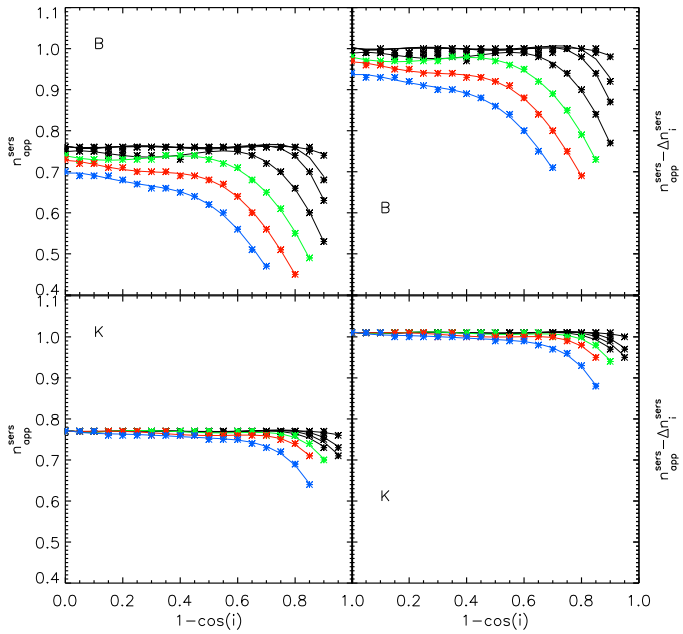

Fig. 22. Left panels: the inclination dependence of the derived Sérsic index for the **exponential bulges** ($n_0^{sers} = 1$), due to combined dust and projection effects. The symbols represent the measurements while the solid line are polynomial fits to the measurements. **Right panels**: The same but corrected for projection effects (Δn_i^{sers}). Upper panels are for the B band and lower panels are for the K band. From top to bottom, the curves are plotted for τ_B^f=0.1, 0.3, 0.5, 1.0 (black), 2.0 (green), 4.0 (red) and 8.0 (blue).

In Fig. 23 we show the inclination dependence of the ratio between the apparent and intrinsic bulge effective radii of exponential bulges, for different values of τ_B^f. The effect of dust on the effective ratios is small, even for large values of τ_B^f, and have a weak dependence on inclination.

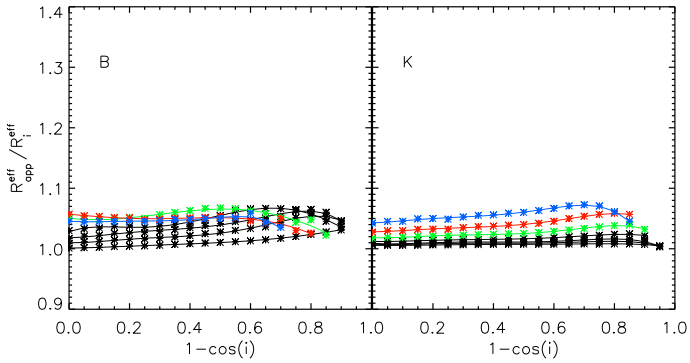

Fig. 23. Dust effects $corr^{dust}$ on the derived effective radius of **exponential ($n_0^{sers} = 1$) bulges**. The symbols represent the measurements while the solid lines are polynomial fits to the measurements. The plots represent the ratio between the apparent and intrinsic Sérsic effective radius, R_{app}^{eff} and R_i^{eff} respectively, versus inclination $(1 - \cos(i))$, for B and K optical bands. From bottom to top, the curves are plotted for τ_B^f=0.1, 0.3, 0.5, 1.0 (black), 2.0 (green), 4.0 (red) and 8.0 (blue).

Overall, looking at the effects dust has on bulge photometric parameters, we noticed an overestimation of the effective radii and an underestimation of the Sérsic indexes, when fitting bulges with variable-index Sérsic functions. The overestimation of the effective radii is more pronounced for de Vaucouleurs bulges than for exponential bulges, while the underestimation of the Sérsic indexes is more pronounced for exponential bulges than for de Vaucouleurs bulges. In particular at high inclination and opacities the ratio of the apparent to intrinsic effective radius increases with inclination for de Vaucouleurs bulges and decreases with inclination for exponential bulges.

All the corrections $corr^{dust}$ for both exponential and de Vaucouleurs bulges are presented in form of coefficients of polynomial fits in Tables B.46, B.47, B.48, B.49, B.50. B.51, B.52, B.53, B.54, B.55. For de Vaucouleurs bulges, the fits at higher inclinations were quite poor, therefore we restricted our measurements to inclinations of up to $1 - cos(i) = 0.7$. Consequently, only the flat trend with inclination was recovered. In addition, we also presented results for de Vaucouleurs fits to de Vaucoulers bulges (constrained Sérsic functions). These are listed in Tables B.56,B.57, B.58, B.59, B.60.

7. Discussion

The corrections presented in this paper, both for projection and dust effects, assume a fixed geometry for the underlying components of spiral galaxies. In particular the relative ratios between scalelengths and scaleheights of stars and dust are fixed to the reproductible trends found from modelling edge-on galaxies with radiative transfer calculations, as described in length in Tuffs et al. (2004) and Popescu et al. (2011). Nonetheless, one can expect some scatter from these trends, and a logical question to ask is to what extent the corrections presented in this paper are affected by such a variation. While it is beyond the scope of this paper to quantify this variation, as indeed the whole power and reliability of the calculations based on radiative transfer calculations rely on the existence of these constant trends in geometrical parameters, we can discuss some simple plausible variations from these trends and consequences for the dust and projection effects.

One geometrical parameter that could vary is the thickness of the old stellar disk relative to its scale-length. As long as the ratio

of the scale-height of the stellar disk to the dust disk remains the same, the dust corrections will not change much. However, there will be a visible effect on the projection effects. In particular this can be seen from our already existing calculations at various optical/NIR wavelengths, since our geometrical model assumes that the scalelength of the stellar disk decreases with increasing wavelength, which is the same, from the point of view of projection effects, as having a thicker stellar disk with increasing wavelength. The main effect is the departure from the cos(i) law of an infinitely thin disk (see Sect. 5.1 and Fig. 2). Because the stellar disk has a larger scaleheight, the departure from the infinitely thin approximation starts at lower inclinations, and the amplitude of the effect is more pronounced. Thus, $corr^{proj}(Q)$, the ratio between the intrinsic axis-ratio Q_i, and the axis-ratio of an infinitely thin disk, Q_0, will increase (at higher inclinations) for galaxies having a thicker stellar disk. Consequently, the overestimation of the exponential scalelength of the disk will start at lower inclinations, and the amplitude of the effect will increase for thicker stellar disks ($corr^{proj}(R)$ will increase). When fitting thicker stellar disks with Sérsic functions, the underestimation of the Sérsic index will also be larger. Overall thicker stellar disks will produce the same trends for projection effects, but with a larger amplitude of the effect.

A more complex problem to address is when an increase in thickness of the stellar disk is also accompanied by an increase in the ratio between the scale-height of stars and that of dust. This will produce not only changes in projection effects but also changes in the dust corrections. An extreme case of such a change can be seen from the differences in dust corrections between the "thin disk" and the "disk". The stellar emissivity in the thin disk is completely embedded in the dust disk, while the disk has a layer of stars extending above the dust layer. Consequently, the dust corrections are less severe for the disk than for the thin disk. Thus, when fitting a galaxy having a larger ratio of the scale-height of stars-to-dust, we will obtain smaller corrections for $corr^{dust}(R)$, $corr^{dust}(R^{eff})$ and Δn^{sersic}, for the same dust opacity and inclination.

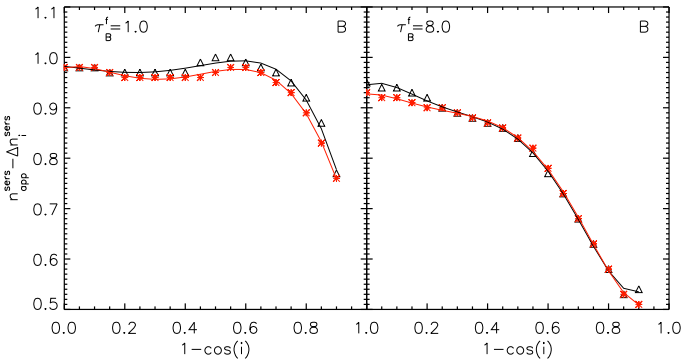

Fig. 24. The inclination dependence of the derived Sérsic index of **bulges** due to dust effects only (corrected for projection effects), for spherical bulges (axis-ratios of 1.0; black curves) and for our standard bulges with axis-ratios of 0.6 (red curves). The symbols represent the measurements while the solid lines are polynomial fits to the measurements. Results are for the B band and for simulations corresponding to volume stellar emissivity described by a (deprojected) Sérsic function with $n_0^{sers} = 1$. Left panel is for τ_B^f=1 and right panel is for τ_B^f=8.

In the case of bulges there are only two parameters defining the geometry: the effective radius and the ellipticity of the bulge. The effective radius in our model was taken to be much smaller than the radial scalelength of the stellar disk (and of the dust disk). Essentially much of the stellar light from the bulge is strongly attenuated by the higher optical depth in the centre of the disks. As long as the size of the bulge remains within these contraints, not much change in the dust corrections are foreseen due to changes in the radial distribution. It is more likely that any effects would be due to changes in the vertical distribution affecting the amount of stars seen above the dust layer. This can be caused by either a larger effective radius of the bulge, or by a more spherical bulge. We test the latter effect by producing a few simulations for bulges with axis ratios equal to unity (spherical bulge). In Fig. 24 we show the results for exponential bulges, for two cases of dust opacity, $\tau_B^f = 1$ and $\tau_B^f = 8$. The curves showing the inclination dependence of the corrected (for projection effects) Sérsic index are very similar for both spherical and ellipsoidal bulges, for both optically thin and optically thick cases. We therefore conclude that the ellipticity of the bulge does not significantly affect the corrections for dust effects of the derived structural parameters of bulges.

8. Application: the wavelength dependence of dust effects

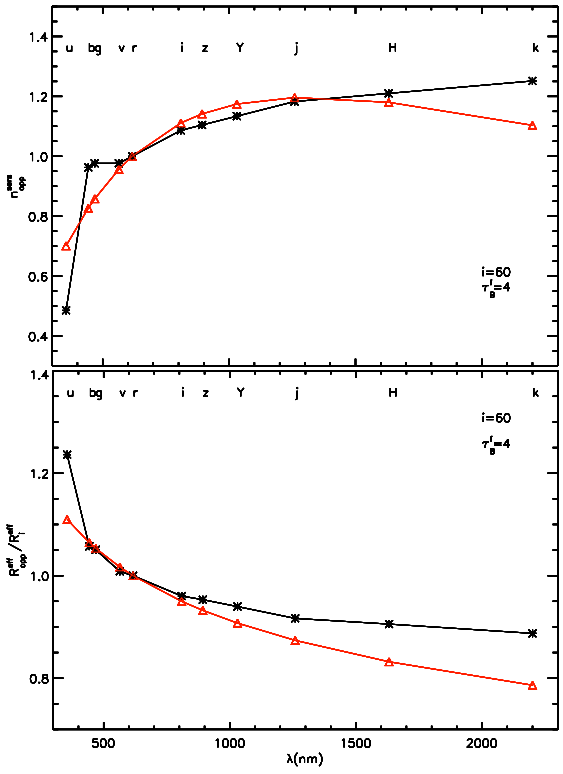

Fig. 25. The wavelength dependence of the Sérsic index (top) and effective radius (bottom) predicted to be measured on a disk population, due to the effect of dust only (black). The recent measurements from the GAMA survey, from Kelvin et al. (2012), are overplotted in red. All the plots are normalised to the corresponding measurement in the r band.

One important application of our modelling is the prediction on the wavelength dependence of the effects of dust. Recent observational work (Kelvin et al. 2012, Häußler et al. 2012) has

shown that for a population of disk dominated galaxies there is a distinctive trend of increasing Sérsic index and effective radius with increasing wavelength. In the case of Kelvin et al. (see the red curves in Fig. 25) the results have been obtained using single-Sérsic fits to 167600 galaxies measured independently in the ugrizYJHK bandpasses using reprocessed Sloan Sky Survey Data Release Seven and UKIRT Infrared Deep Sky Survey Large Area Survey imaging data available from the Galaxy and Mass Assembly (GAMA; Driver et al. 2011). The measured galaxies have been further divided into early-type and late-type galaxies, according the the K-band Sérsic index/u-r color relation. For the late-type galaxies their averaged trends are compared with the predictions of our models (black curves in Fig. 25). For this purpose we considered our $corr^{dust}$ obtained for disks simulations with $\tau_B^f = 4$ and for an average inclination of 60°. The choice of $\tau_B^f = 4$ was motivated by the analysis of the attenuation-inclination relation by Driver et al. (2007), who found an average dust opacity for local universe disk galaxies of $\tau_B^f = 3.8$. A similar average value for comparable stellar masses was also found by Grootes et al. (2012). Also, radiative transfer analysis of the UV to FIR SEDs of individual edge-on galaxies by Misiriotis et al. (2001) and Popescu et al. (2004) found similar values for τ_B^f.

The comparison between data and model predictions for effective radii indicates that in both cases there is a trend of decreasing radius with increasing wavelength, with the data showing a more pronounced decrease than the models. This could potentially indicate that, in addition to the dust effects, there is an intrinsic stellar gradient, with disks being smaller at longer than at shorter wavelength, as predicted from theories of disk growth from inside out. This preliminary result would need to be followed up with more accurate determinations of disk sizes, which are performed on disk/bulge decomposition. The caveat of our interpretation is that, although a population of disk dominated galaxies has been isolated in Kelvin et al. (2012), we cannot exclude contamination with bulges in late-type spirals. This would bias the results towards smaller effective radii at longer wavelength, where bulges are more prominent (see also Häußler et al 2012), resulting in the same qualitative trend as the effect of intrinsic stellar gradients. Thus, a quantitative interpretation of these trends are still awaiting for more accurate determinations of disk sizes and disk opacities.

The comparison between data and model predictions for Sérsic indexes shows again that dust effects can account for most of the trends shown in the data, with a small difference towards the K band. As before, we note that a quantitative comparison of these trends would require disk measurements obtained from bulge-disk decomposition on higher resolution data.

9. Summary and Conclusions

In this paper we present the results of a study to quantify the effects of dust on the derived photometric parameters of pure disks and bulges in spiral galaxies. In our approach we followed the same path observers do, but instead of real images we used simulated ones, produced by radiative transfer techniques.

The simulations were produced as part of the large library of dust and PAH emission SEDs and corresponding dust attenuations presented in Popescu et al. (2011). All the simulations were calculated using a modified version of the ray-tracing radiative transfer code of Kylafis & Bahcall (1987), which include a full treatment of anisotropic scattering. The simulations were produced separately for old stellar disks, bulges and young stellar disks, all seen through a common distribution of dust.

The intrinsic volume stellar distributions were described by exponential functions in both radial and vertical directions for the disks and by deprojected de Vaucouleurs functions for the bulges. The corresponding dust distributions were described by double (radial and vertical) exponential functions for the two dust disks of the model. Apart from these already existing simulations additional ones have been produced for the purpose of this study. These are simulations of bulges corresponding to general Sérsic functions with various Sérsic indexes.

We fitted the simulated images of disks and bulges with 1D analytic functions available in GALFIT, the same ones observers use when fitting real galaxy images (exponentials/variable index Sérsic functions or de Vaucouleurs distributions). We showed that, even in the absence of dust, these simple distributions would differ from those of real galaxies due to the fact that they describe infinitely thin disks, while disks and bulges have a thickness. We called these effects **projection effects**.

The approach adopted in this paper was to separate projection from dust effects. Thus, we first derived the projection effects, by calculating the change between the intrinsic parameters of the volume emissivity and those measured on dustless images. Subsequently, we derived the dust effects by calculationg the change between the parameters measured on dustless and dusty images, respectively, for the same inclination and wavelength. The total change in parameter values between the measured ones on dusty images and the corresponding parameters of the volume stellar emissivity was written as a chain of corrections (Eq. 4,5,6 or Eq. 7,8,9).

We showed that one advantage of this approach is that it provides a more robust quantification of the dust effects. In particular we showed that the term related to projection effects is affected by variations in the geometrical parameters of the volume stellar emissivity, including the truncation radius, while the term related to dust effects is relatively insensitive to such factors.

The main results on the dust effects are as follows:

Disks

- The derived scale-length of dusty disks fitted with exponential functions is always greater than that obtained in the absence of dust, with the amplitude of the effect increasing with the central face-on dust opacity τ_B^f of the disk and with inclination, and with decreasing wavelength. The increase is very small for low values of τ_B^f or longer wavelengths, steepens for intermediate values of τ_B^f or higher inclinations, and flattens again for very high values of τ_B^f and shorter wavelengths.
- The derived central surface-brightness of dusty disks fitted with exponential functions is always fainter than that obtained in the absence of dust, with the amplitude of the effect increasing with τ_B^f of the disk and with inclination, and with decreasing wavelength.
- At low to intermediate inclinations, up to $1 - cos(i) = 0.65$, the derived axis-ratio in the presence of dust is the same as the intrinsic axis-ratio, which, in turn, is the same as the axis ratio of the infinitely thin disk, $cos(i)$. It is only at higher inclinations and higher dust opacities that the dust starts to affect the derived axis-ratios, in the sense that the measured ratios are lower than the corresponding intrinsic values. This means that dust makes disks appear slightly thinner than they are in reality. Nonetheless, even at higher inclinations and

dust opacities, the effects due to dust are smaller than projection effects. Overall, the correction from the $cos(i)$ term is dominated by the increase in the axis ratio due to the vertical distribution of stars.
– The derived Sérsic index of dusty disks fitted with Sérsic functions is, for a broad range of τ_B^f and inclinations, smaller than that obtained in the absence of dust. The trend is for the Sérsic index to decrease with increasing inclination and τ_B^f. Only at very high opacitites (τ_B^f=4,8) and close to the edge-on view is the derived Sérsic index larger than that obtained in the absence of dust, and the trend with inclination is reversed. At low inclinations the deviations from exponentiality are mainly due to dust effects while at higher inclinations, both dust and projection effects affect the derived Sérsic index.
– The derived effective radius of disks fitted with Sérsic functions is always greater than that obtained in the absence of dust, with the amplitude of the effect increasing with τ_B^f of the disk and with inclination, and with decreasing wavelength.
– The effects of dust on the derived axis ratios are the same for the Sérsic and exponential fits.

Thin Disks

– The trends in the derived scale-length and effective radius of thin disks fitted with exponential and Sérsic functions, respectively, are similar to those obtained for disks. However, the amplitude of the effect is more pronounced, even when the comparison is done at the same optical wavelength. In the UV range the trend with wavelength is non-monotonic, due to the bump in the extinction curve at the 2200 Å. The derived Sérsic index is always smaller than that obtained in the absence of dust, and has a monotonic decrease with increasing inclination and τ_B^f.
– We also show corrections for the $H\alpha$ line, both for the case of exponential and Sérsic fits.

Bulges

– The effects of dust do not seem to strongly depend on the exact value of the Sérsic index corresponding to the intrinsic volume stellar emissivity, n_0^{sers}. Only at very high values of n_0^{sers} and close to the edge-on view do the effects of dust start to deviate from the trends seen at lower n_0^{sers}.
– The effects of dust are completely insensitive to the truncation radius of the bulge, in strong contrast to projection effects, which critically depend on the choice of truncation radius.
– The effects of dust are also insensitive to the ellipticity of the bulge. In particular spherical or ellipsoidal bulges seem to require the same corrections for the effects of dust.
– Dust does not significantly change the derived Sérsic index of bulges, for a wide range of τ_B^f and inclinations. Only at very high τ_B^f and close to the edge-on view is the derived Sérsic index of bulges smaller that that obtained in the absence of dust (the Sérsic index is underestimated). The trend is for the Sérsic index to decrease with inclination and τ_B^f.
– Similarly, dust only induces small changes in the derived effective radius of bulges. The radii are higher than that obtained in the absence of dust. The trend is for the effective radius to increase with τ_B^f.
– The overestimation of the effective radii is more pronounced for de Vaucouleurs bulges than for exponential bulges, while the underestimation of the Sérsic indexes is more pronounced for exponential bulges than for de Vaucouleurs bulges.

We used our derived corrections to compare our model predictions for the wavelength dependence of dust effects with similar trends seen in recent observational data coming from the GAMA survey (Kelvin et al. 2012). The results of this comparison for Sérsic indexes and effective radii show that dust effects can account for most of the trends seen in the data, with some additional room for intrinsic gradients in the stellar populations.

All the corrections for dust, for all opacities considered in this paper and at different wavelengths, are listed in the tables given in the Appendix. The corrections are provided in form of coefficients of polynomial fits to the corrections as a function of inclination. In the optical range, where both a disk and a thin disk are emitting, we recommend the following. For correcting the structural parameters of optical images in broad-band continuum light, dust corrections for the "disk" (and "bulge") component should be used. The corrections for the thin disk in the optical should only be used for correcting narrow-band optical images of line emission (Balmer or nebular lines), by interpolating between the optical wavelengths tabulated in this paper (except for the Hα line, for which corrections are already explicitely listed in the tables of this paper). The main application of our dust corrections for the thin disk is for UV broad-band imaging, where this morphological component dominates the bolometric output and appearance of the spiral galaxy images.

This study was done for pure disks and bulges. As real spiral galaxies have both a bulge and a disk one needs to decompose their images into its components - bulge-disk decompositions - and only then correct for dust and projection effects to recover the intrinsic photometric parameters. Doing bulge-disk decompositions to real dusty spiral galaxy images has proven to be a difficult task as the derived photometric parameters for disks and bulges can be biased due to the decomposition process itself. In this respect, a mixing between stellar emissivity coming from disks and bulges can occur, with a fraction of the disk stellar emissivity being embedded in the bulge stellar emissivity as a result of the decompositions (and vice-versa). Therefore one needs to quantify the dust effects when doing bulge-disk decompositions. In our future work we will assess the dust effects on bulge-disk decompositions through multi-component fits of simulated galaxy images. This new set of corrections will be added to the ones due to projection and dust effects in the attempt to accurately recover the intrinsic photometric parameters of disk and bulges in spiral galaxies.

Acknowledgements. We thank the referee for his careful reading of the text, for the useful suggestions and for pointing out an omission from the original manuscript. C.C. Popescu thanks the Max Planck Institute für Kernphysik for support during a sabbatical, when this work was completed.

References

Allen, P.D., Driver, S.P., Graham, A.W. et al. 2006, MNRAS, 371, 2
Arnaboldi, M., Rejkuba, M., Retzlaff, J. et al. 2012, Msngr, 149, 7
Baes, M., Davies, J. I., Dejonghe, H. et al. 2003, MNRAS, 343, 1081
Bamford, S.P. et al. 2012, submitted
Boissier, S., Boselli, A., Buat, V. et al. 2004, A&A, 424, 465
Bourne, N., Maddox, S. J., Dunne, L. et al. 2012, MNRAS, 421, 3027
Byun Y. I., Freeman K. C., Kylafis N. D. 1994, ApJ, 432, 114
Cimatti, A. & Scaramella, R. 2012, MSAIS, 19, 31
Ciotti, L. & Bertin, G. 1999, A&A, 352, 447
Cunow B. 2001, MNRAS, 323, 130

Evans R. 1994, MNRAS, 266, 511
Dale, D. A., Aniano, G., Engelbracht, C. W. et al. 2012, ApJ, 2012, 745, 95
Dariush, A., Cortese, L., Eales, S. et al. 2011, MNRAS, 418, 64
Draine, B.T. & Li, A. 2007, ApJ, 657, 810
Driver, S. P., Popescu, C. C., Tuffs, R. J. et al. 2007, MNRAS, 379, 1022
Driver, S.P., Hill, D.K., Kelvin, L.S. et al. 2011, MNRAS, 413, 971
Dwek, E. 1998, ApJ, 501, 643
Emerson, J.P. & Sutherland, W.J. 2010, SPIE, 7733, 4
Gadotti A. D. 2008, MNRAS, 384, 420
Gadotti A. D., Baes M., Falony S. 2010, MNRAS, 403, 2053
Graham, A.W. 2011, arXiv:1108.0997
Graham, A.W. & Driver, S.P. 2005, PASA, 22, 118
Graham, A.W. & Worley, C.C. 2008, MNRAS, 388, 1708
Grootes, M., Tuffs, R.J., Popescu, C.C., Pastrav, B.A., Andrae, E. et al. 2013, ApJ submitted
Häußler, B., Bamford, S.P., Vika, M. et al. 2012, MNRAS accepted, arXiv:1212.3332
Hoyos, C., den Brok, M., Verdoes, K.G. et al. 2011, MNRAS, 411, 2439
Hubble E. 1926, ApJ, 64, 321
Jouvel, S. Kneib, J.-P., Bernstein, G. et al. 2011, A&A, 532, 25
Kelvin, L.S., Driver, S.P., Robotham, A.S.G. et al. 2012, MNRAS, 421, 1007
Kylafis, N. D. & Bahcall, J. N. 1987, ApJ, 317, 637
Lackner, C. N, Gunn, J. E. 2012, MNRAS, 421, 2277
Laureijs, R.J., Duvet, L., Escudero S.I. et al. 2010, SPIE, 7731, 40
Maltby, D. T., Hoyos, C., Gray, M. E., Aragón-Salamanca, A., Wolf, C. 2012, MNRAS, 420, 2475
Martinelli, M., Calabrese, E., de Bernardis, F. et al. 2011, Phys. Rev. D, 83, 023012
Misiriotis, A., Popescu, C. C., Tuffs, R., Kylafis, N. D. 2001, A&A, 372, 775
Mo, H., Mao, S., White, S. D. M. 1998, MNRAS, 295, 319
Möllenhoff, C., Popescu, C. C., Tuffs, R. J. 2006, A&A, 456, 941
Pastrav, B. A., Popescu, C. C., Tuffs, R. J., Sansom, A. E. 2012, in Proceedings of the IAU Symp. 284: The Spectral Energy Distribution of Galaxies, eds. R. J. Tuffs & C. C. Popescu, 306
Peacock, J.. 2008, in “A Decade of Dark Energy”, eds N. Pirzkal and H. Ferguson
Peng, C. Y., Ho, L. C., Impey, C. D., Rix 2002, H.-W., AJ, 124, 266
Peng, C. Y., Ho, L. C., Impey, C. D., Rix 2010, H.-W., AJ, 139, 2097
Pierini D., Gordon K. D., Witt A. N., Madsen G. J. 2004, ApJ, 617, 1022
Popescu, C. C., Misiriotis, A., Kylafis, N. D., Tuffs, R. J. & Fischera, J. 2000, A&A, 362, 138
Popescu, C.C., Tuffs, R.J., Vlk, H.J., Pierini, D., Madore, B.F. 2002, ApJ, 567, 221
Popescu, C. C., Tuffs, R. J., Kylafis, N. D., Madore, B. F. 2004, A&A, 414, 45
Popescu, C. C., Tuffs, R. J., Madore, B. F. et al. 2005, ApJ, 619, L75
Popescu, C. C., Tuffs, R. J., Dopita, M. A. et al. 2011, A&A, 527, A109
Rowlands, K., Dunne, L., Maddox, S., et al. 2012, MNRAS, 419, 2545
Simard, L., Willmer, C.N.A., Vogt, N.P. et al. 2002, ApJS, 142, 1
Simard, L., Mendel, J.T, Patton, D.R. et al. 2011, ApJS, 196, 11
Stickel, M., Lemke, D., Klaas, U. et al. 2000, A&A, 359, 865
Stickel, M., Lemke, D., Klaas, U., Krause, O., & Egner, S. 2004, A&A, 422, 39
Tuffs, R.J., Popescu, C.C., Pierini, D. et al. 2002, ApJS, 139, 37
Tuffs, R. J., Popescu, C. C., Völk, H. J., Kylafis, N. D., Dopita, M. A. 2004, A&A, 419, 821
Vlahakis, C., Dunne, L. & Eales, S. 2005, MNRAS, 364, 1253
Weingartner, J.C. & Draine, B.T. 2001, ApJ, 548, 296
York, D. G., Adelman, J., Anderson, J. E. Jr. et al. 2000, AJ, 120, 1579

Appendix A: The corrections for projection effects

Table A.1. Projection effects $corr^{proj}$ on the derived photometric parameters of the **disk**: scale-lengths and central surface brightnesses. Results are listed as coefficients of polynomial fits a_k (Eq. 14) at different optical wavelengths, corresponding to the effective wavelength of B,V,I,J,K bands.

Disk (exponential fits)		
	$\frac{R_i}{R_0}$	ΔSB_0
B		
a_0	1.000	-0.005
a_1	0.005	-0.736
a_2	-0.055	0.863
a_3	0.352	0.825
a_4	-0.699	-4.004
a_5	0.497	2.542
V		
a_0	1.000	-0.006
a_1	0.010	-0.740
a_2	-0.101	0.703
a_3	0.508	1.524
a_4	-0.915	-5.095
a_5	0.603	3.116
I		
a_0	1.000	-0.005
a_1	0.026	-0.917
a_2	-0.239	1.789
a_3	0.970	-1.652
a_4	-1.547	-1.135
a_5	0.912	1.390
J		
a_0	1.000	-0.004
a_1	0.032	-1.102
a_2	-0.292	2.813
a_3	1.164	-4.469
a_4	-1.817	2.233
a_5	1.047	-0.017
K		
a_0	1.000	-0.004
a_1	0.037	-1.230
a_2	-0.310	3.120
a_3	1.232	-4.717
a_4	-1.902	1.986
a_5	1.089	0.336

Table A.2. Projection effects $corr^{proj}$ on the derived axis ratios of the **disk**. Results are listed as coefficients of polynomial fits a_k and b_0 (Eq. 19) at different optical wavelengths, corresponding to the effective wavelength of B,V,I,J,K bands.

Disk (exponential fits)	
	$\frac{Q_i}{Q_0}$
B	
a_0	1.000
a_1	0.062
a_2	-1.076
a_3	5.554
a_4	-10.067
a_5	6.219
b_0	1.800
V	
a_0	1.000
a_1	0.112
a_2	-1.403
a_3	6.462
a_4	-11.075
a_5	6.591
b_0	1.800
I	
a_0	1.000
a_1	0.354
a_2	-3.917
a_3	15.437
a_4	-24.016
a_5	13.120
b_0	1.800
J	
a_0	1.000
a_1	0.199
a_2	-1.876
a_3	7.766
a_4	-12.960
a_5	7.765
b_0	2.000
K	
a_0	1.000
a_1	0.456
a_2	-4.612
a_3	17.689
a_4	-27.146
a_5	14.786
b_0	2.200

Table A.3. Projection effects $corr^{proj}$ on the derived photometric parameters of the **disk**: effective radius, central surface brightnesses and Sérsic index. Results are listed as coefficients of polynomial fits a_k (Eq. 14) at different optical wavelengths, corresponding to the effective wavelength of B,V,I,J,K bands.

	Disk (Sérsic fits)		
	$\frac{R_i}{R_0}$	ΔSB_0	n_i^{sers}
B			
a_0	1.000	0.022	1.000
a_1	0.019	-0.641	-0.023
a_2	-0.368	0.893	-0.180
a_3	1.259	1.228	0.459
a_4	-1.840	-4.709	-4.709
a_5	0.891	3.375	0.000
V			
a_0	1.000	0.022	1.000
a_1	0.024	-0.671	-0.041
a_2	-0.429	1.030	-0.057
a_3	1.479	0.897	0.141
a_4	-2.162	-4.321	-4.321
a_5	1.059	3.205	0.000
I			
a_0	1.000	0.026	1.000
a_1	0.046	-0.906	-0.067
a_2	-0.625	2.819	0.060
a_3	2.139	-4.731	-0.117
a_4	-3.098	3.214	3.214
a_5	1.539	-0.355	0.000
J			
a_0	1.000	0.032	1.000
a_1	0.065	-1.163	-0.112
a_2	-0.794	4.633	0.369
a_3	2.681	-10.149	-0.824
a_4	-3.848	10.273	10.273
a_5	1.921	-3.636	0.000
K			
a_0	1.000	0.035	1.000
a_1	0.057	-1.297	-0.146
a_2	-0.809	5.376	0.530
a_3	2.825	-12.078	-1.220
a_4	-4.138	12.662	12.662
a_5	2.110	-4.729	0.000

Table A.4. Projection effects $corr^{proj}$ on the derived photometric parameters of the **bulge**: effective radius and Sérsic index. Results are listed as coefficients of polynomial fits a_0 (Eq. 14) for four different n_0^{sers} of the intrinsic volume stellar emissivity and two different truncation radii ($3R_0^{eff}$ and $10R_0^{eff}$). Results are independent of optical waveband.

		Bulge (Sérsic fits)	
$3R_0^{eff}$	n_0^{sers}	$\frac{R_i^{eff}}{R_0^{eff}}$	n_i^{sers}
a_0	1	1.124	0.760
a_0	2	1.009	1.604
a_0	4	0.875	3.123
a_0	8	0.702	5.490
$10R_0^{eff}$	n_0^{sers}	$\frac{R_i^{eff}}{R_0^{eff}}$	n_i^{sers}
a_0	1	1.212	0.860
a_0	2	1.200	1.829
a_0	4	1.177	3.760
a_0	8	1.061	7.112

Table A.5. Projection effects $corr^{proj}$ on the derived effective radius of de Vaucouleurs **bulges**. Bulges are truncated at $3R_0^{eff}$. Results are listed as coefficients of polynomial fits a_0 (Eq. 14). Results are independent of optical waveband.

Bulge (de Vaucouleurs fits)	
	$\frac{R_i}{R_0}$
a_0	0.870

Appendix B: The corrections for dust effects

Table B.1. Dust effects $corr^{dust}$ on the derived photometric parameters of the **disk**: scale-lengths and central surface brightnesses. Results are listed as coefficients of polynomial fits a_k (Eq. 14) at different τ_B^f and at the effective wavelength of the B band.

Disk (exponential fits); B band

	$\frac{R_{app}}{R_i}$	ΔSB
$\tau_B^f = 0.1$		
a_0	0.997	-0.038
a_1	0.085	1.616
a_2	-0.812	-15.360
a_3	2.937	52.673
a_4	-4.296	-73.834
a_5	2.274	36.932
$\tau_B^f = 0.3$		
a_0	1.001	-0.043
a_1	0.021	2.361
a_2	-0.179	-23.824
a_3	1.204	86.724
a_4	-2.266	-126.152
a_5	1.577	65.145
$\tau_B^f = 0.5$		
a_0	1.011	-0.010
a_1	-0.109	2.286
a_2	1.185	-20.803
a_3	-3.211	76.489
a_4	3.783	-113.419
a_5	-1.257	60.717
$\tau_B^f = 1.0$		
a_0	1.043	0.106
a_1	-0.251	2.702
a_2	3.103	-22.735
a_3	-9.716	84.285
a_4	13.274	-122.295
a_5	-6.060	64.497
$\tau_B^f = 2.0$		
a_0	1.120	0.501
a_1	-0.056	3.620
a_2	2.405	-26.334
a_3	-7.737	95.612
a_4	11.398	-135.142
a_5	-5.750	69.357
$\tau_B^f = 4.0$		
a_0	1.274	1.300
a_1	0.372	3.307
a_2	-0.613	-19.225
a_3	1.889	73.647
a_4	-1.905	-108.615
a_5	0.457	58.097
$\tau_B^f = 8.0$		
a_0	1.470	2.278
a_1	0.529	4.961
a_2	-2.545	-30.875
a_3	7.470	104.631
a_4	-9.944	-146.070
a_5	4.658	75.259

Table B.2. Dust effects $corr^{dust}$, as in Table B.1, but in V band.

Disk (exponential fits); V band

	$\frac{R_{app}}{R_i}$	ΔSB
$\tau_B^f = 0.1$		
a_0	0.996	-0.066
a_1	0.077	1.918
a_2	-0.736	-18.401
a_3	2.634	63.155
a_4	-3.826	-88.001
a_5	2.003	42.994
$\tau_B^f = 0.3$		
a_0	0.997	-0.115
a_1	0.073	3.761
a_2	-0.660	-34.873
a_3	2.661	118.192
a_4	-4.140	-164.147
a_5	2.383	81.037
$\tau_B^f = 0.5$		
a_0	1.001	-0.099
a_1	-0.008	3.738
a_2	0.190	-35.218
a_3	-0.030	123.256
a_4	-0.528	-175.160
a_5	0.753	88.595
$\tau_B^f = 1.0$		
a_0	1.022	-0.027
a_1	-0.190	2.530
a_2	2.232	-22.728
a_3	-6.798	84.104
a_4	9.033	-122.926
a_5	-3.910	65.082
$\tau_B^f = 2.0$		
a_0	1.074	0.249
a_1	-0.162	2.492
a_2	2.843	-19.569
a_3	-9.104	76.479
a_4	13.040	-112.807
a_5	-6.337	60.324
$\tau_B^f = 4.0$		
a_0	1.194	0.855
a_1	0.212	4.148
a_2	0.534	-30.259
a_3	-1.796	113.208
a_4	3.296	-164.003
a_5	-2.042	84.867
$\tau_B^f = 8.0$		
a_0	1.380	1.802
a_1	0.454	5.040
a_2	-1.699	-34.958
a_3	5.204	123.917
a_4	-6.930	-175.264
a_5	3.124	89.385

Table B.3. Dust effects $corr^{dust}$, as in Table B.1, but in I band.

Disk (exponential fits); I band		
	$\frac{R_{app}}{R_i}$	ΔSB
$\tau_B^f = 0.1$		
a_0	0.998	-0.040
a_1	0.043	1.170
a_2	-0.405	-10.802
a_3	1.465	35.834
a_4	-2.135	-48.074
a_5	1.120	22.735
$\tau_B^f = 0.3$		
a_0	0.995	-0.094
a_1	0.080	2.791
a_2	-0.687	-26.681
a_3	2.541	92.471
a_4	-3.763	-129.647
a_5	2.042	64.046
$\tau_B^f = 0.5$		
a_0	0.996	-0.116
a_1	0.072	3.692
a_2	-0.518	-35.113
a_3	2.039	121.962
a_4	-3.126	-170.856
a_5	1.818	84.483
$\tau_B^f = 1.0$		
a_0	1.003	-0.123
a_1	-0.004	3.955
a_2	0.503	-34.541
a_3	-1.433	119.722
a_4	1.789	-168.466
a_5	-0.516	84.852
$\tau_B^f = 2.0$		
a_0	1.029	0.005
a_1	-0.080	3.910
a_2	1.822	-32.885
a_3	-6.159	115.346
a_4	8.943	-161.037
a_5	-4.232	81.347
$\tau_B^f = 4.0$		
a_0	1.098	0.354
a_1	0.080	4.626
a_2	1.136	-33.132
a_3	-4.122	114.623
a_4	6.840	-158.173
a_5	-3.731	79.565
$\tau_B^f = 8.0$		
a_0	1.238	1.101
a_1	0.350	5.451
a_2	-0.927	-37.437
a_3	2.791	131.221
a_4	-3.132	-183.944
a_5	1.049	93.035

Table B.4. Dust effects $corr^{dust}$, as in Table B.1, but in J band.

Disk (exponential fits); J band		
	$\frac{R_{app}}{R_i}$	ΔSB
$\tau_B^f = 0.1$		
a_0	0.999	-0.003
a_1	0.025	-0.387
a_2	-0.230	3.483
a_3	0.816	-9.873
a_4	-1.165	10.686
a_5	0.597	-3.568
$\tau_B^f = 0.3$		
a_0	0.998	-0.032
a_1	0.063	0.599
a_2	-0.555	-5.416
a_3	1.962	19.556
a_4	-2.794	-28.555
a_5	1.441	14.989
$\tau_B^f = 0.5$		
a_0	0.998	-0.053
a_1	0.087	1.439
a_2	-0.727	-14.406
a_3	2.566	53.389
a_4	-3.646	-78.165
a_5	1.895	39.884
$\tau_B^f = 1.0$		
a_0	1.000	-0.069
a_1	0.103	2.379
a_2	-0.700	-21.841
a_3	2.431	77.446
a_4	-3.396	-111.134
a_5	1.823	56.793
$\tau_B^f = 2.0$		
a_0	1.010	-0.027
a_1	0.072	2.777
a_2	0.025	-24.235
a_3	-0.289	85.624
a_4	0.722	-121.744
a_5	-0.234	62.772
$\tau_B^f = 4.0$		
a_0	1.039	0.065
a_1	0.072	3.090
a_2	0.739	-20.816
a_3	-3.223	71.558
a_4	5.601	-99.585
a_5	-2.951	51.943
$\tau_B^f = 8.0$		
a_0	1.110	0.502
a_1	0.264	3.961
a_2	-0.326	-25.968
a_3	0.093	90.053
a_4	1.546	-123.285
a_5	-1.428	62.387

Table B.5. Dust effects $corr^{dust}$, as in Table B.1, but in K band.

Disk (exponential fits); K band		
	$\frac{R_{app}}{R_i}$	ΔSB
$\tau_B^f = 0.1$		
a_0	1.000	-0.002
a_1	0.007	0.177
a_2	-0.064	-1.737
a_3	0.241	6.099
a_4	-0.356	-8.839
a_5	0.189	4.587
$\tau_B^f = 0.3$		
a_0	1.001	0.005
a_1	0.017	-0.201
a_2	-0.163	0.870
a_3	0.638	-0.106
a_4	-0.962	-2.692
a_5	0.517	2.674
$\tau_B^f = 0.5$		
a_0	1.001	0.008
a_1	0.023	-0.141
a_2	-0.232	-0.302
a_3	0.928	5.527
a_4	-1.414	-11.720
a_5	0.769	7.566
$\tau_B^f = 1.0$		
a_0	1.003	0.010
a_1	0.037	0.796
a_2	-0.338	-11.017
a_3	1.371	44.350
a_4	-2.107	-66.118
a_5	1.167	33.936
$\tau_B^f = 2.0$		
a_0	1.008	-0.013
a_1	0.032	2.251
a_2	-0.212	-22.720
a_3	1.037	81.245
a_4	-1.713	-113.686
a_5	1.057	56.193
$\tau_B^f = 4.0$		
a_0	1.020	0.021
a_1	-0.016	3.379
a_2	0.508	-28.283
a_3	-1.456	96.856
a_4	1.871	-135.716
a_5	-0.672	68.721
$\tau_B^f = 8.0$		
a_0	1.047	0.183
a_1	-0.031	4.151
a_2	1.244	-33.590
a_3	-4.392	113.511
a_4	6.612	-153.092
a_5	-3.251	75.245

Table B.6. Dust effects $corr^{dust}$ on the derived axis ratios of the **disk**. Results are listed as coefficients of polynomial fits a_0 and b_k (Eq. 21) at different τ_B^f and at the effective wavelength of the B band.

Disk (exponential fits) B band	
	$\frac{Q_{app}}{Q_i}$
$\tau_B^f = 0.1$	
a_0	1.000
b_0	–
b_1	–
$\tau_B^f = 0.3$	
a_0	1.000
b_0	–
b_1	–
$\tau_B^f = 0.5$	
a_0	1.000
b_0	0.888
b_1	–
$\tau_B^f = 1.0$	
a_0	1.000
b_0	0.888
b_1	–
$\tau_B^f = 2.0$	
a_0	1.000
b_0	0.888
b_1	–
$\tau_B^f = 4.0$	
a_0	1.000
b_0	1.202
b_1	-0.317
$\tau_B^f = 8.0$	
a_0	1.000
b_0	1.202
b_1	-0.317

Table B.7. Dust effects $corr^{dust}$, as in Table B.6, but in V band.

Disk (exponential fits) V band	$\frac{Q_{app}}{Q_i}$
$\tau_B^f = 0.1$	
a_0	1.000
b_0	–
b_1	–
$\tau_B^f = 0.3$	
a_0	1.000
b_0	–
b_1	–
$\tau_B^f = 0.5$	
a_0	1.000
b_0	–
b_1	–
$\tau_B^f = 1.0$	
a_0	1.000
b_0	0.888
b_1	–
$\tau_B^f = 2.0$	
a_0	1.000
b_0	0.888
b_1	–
$\tau_B^f = 4.0$	
a_0	1.000
b_0	1.185
b_1	-0.285
$\tau_B^f = 8.0$	
a_0	1.000
b_0	1.152
b_1	-0.259

Table B.8. Dust effects $corr^{dust}$, as in Table B.6, but in I band.

Disk (exponential fits) I band	$\frac{Q_{app}}{Q_i}$
$\tau_B^f = 0.1$	
a_0	1.000
b_0	–
b_1	–
$\tau_B^f = 0.3$	
a_0	1.000
b_0	–
b_1	–
$\tau_B^f = 0.5$	
a_0	1.000
b_0	–
b_1	–
$\tau_B^f = 1.0$	
a_0	1.000
b_0	–
b_1	–
$\tau_B^f = 2.0$	
a_0	1.000
b_0	–
b_1	–
$\tau_B^f = 4.0$	
a_0	1.000
b_0	1.263
b_1	-0.380
$\tau_B^f = 8.0$	
a_0	1.000
b_0	1.173
b_1	-0.277

Table B.9. Dust effects $corr^{dust}$, as in Table B.6, but in J band.

Disk (exponential fits) J band	$\frac{Q_{app}}{Q_i}$
$\tau_B^f = 0.1$	
a_0	1.000
b_0	–
b_1	–
$\tau_B^f = 0.3$	
a_0	1.000
b_0	–
b_1	–
$\tau_B^f = 0.5$	
a_0	1.000
b_0	–
b_1	–
$\tau_B^f = 1.0$	
a_0	1.000
b_0	–
b_1	–
$\tau_B^f = 2.0$	
a_0	1.000
b_0	–
b_1	–
$\tau_B^f = 4.0$	
a_0	1.000
b_0	1.115
b_1	-0.283
$\tau_B^f = 8.0$	
a_0	1.000
b_0	1.180
b_1	-0.285

Table B.10. Dust effects $corr^{dust}$, as in Table B.6, but in K band.

Disk (exponential fits) K band	$\frac{Q_{app}}{Q_i}$
$\tau_B^f = 0.1$	
a_0	1.000
b_0	–
b_1	–
$\tau_B^f = 0.3$	
a_0	1.000
b_0	–
b_1	–
$\tau_B^f = 0.5$	
a_0	1.000
b_0	–
b_1	–
$\tau_B^f = 1.0$	
a_0	1.000
b_0	–
b_1	–
$\tau_B^f = 2.0$	
a_0	1.000
b_0	–
b_1	–
$\tau_B^f = 4.0$	
a_0	1.000
b_0	–
b_1	–
$\tau_B^f = 8.0$	
a_0	1.000
b_0	1.155
b_1	-0.234

Table B.11. Dust effects $corr^{dust}$ on on the derived photometric parameters of the **disk**: effective radius, central surface brightnesses and Sérsic index. Results are listed as coefficients of polynomial fits a_k (Eq. 14) at different τ_B^f and at the effective wavelength of the B band.

Disk (Sérsic fits); B band

	$\frac{R_{app}}{R_i}$	ΔSB	n_{app}^{sers}
$\tau_B^f = 0.1$			
a_0	0.995	-0.063	1.002
a_1	0.044	2.372	-0.182
a_2	-0.345	-22.131	1.211
a_3	1.120	74.180	-4.537
a_4	-1.560	-101.264	6.691
a_5	0.833	48.914	-3.684
$\tau_B^f = 0.3$			
a_0	0.994	-0.048	0.992
a_1	0.056	2.415	-0.132
a_2	-0.496	-21.653	0.417
a_3	1.898	74.819	-1.545
a_4	-2.891	-104.905	2.127
a_5	1.672	53.047	-1.365
$\tau_B^f = 0.5$			
a_0	0.995	0.003	0.967
a_1	0.065	2.920	0.247
a_2	-0.613	-24.752	-3.059
a_3	2.598	83.061	9.676
a_4	-4.112	-112.046	-13.110
a_5	2.425	55.212	5.969
$\tau_B^f = 1.0$			
a_0	1.002	0.194	0.925
a_1	0.122	4.000	0.393
a_2	-1.139	-33.452	-5.211
a_3	5.024	117.268	17.873
a_4	-8.032	-160.212	-25.941
a_5	4.653	77.956	13.052
$\tau_B^f = 2.0$			
a_0	1.026	0.727	0.842
a_1	-0.041	5.733	-0.142
a_2	1.345	-44.096	-0.664
a_3	-3.587	156.440	2.953
a_4	3.989	-218.542	-5.624
a_5	-1.016	107.254	3.783
$\tau_B^f = 4.0$			
a_0	1.099	1.718	0.729
a_1	0.141	5.685	-0.277
a_2	0.394	-37.795	1.157
a_3	-1.125	129.619	-3.232
a_4	2.309	-182.610	4.996
a_5	-1.065	91.756	-2.343
$\tau_B^f = 8.0$			
a_0	1.230	2.763	0.685
a_1	0.483	6.037	0.878
a_2	-1.827	-44.548	-7.585
a_3	6.694	144.855	27.851
a_4	-7.716	-197.911	-37.802
a_5	2.714	98.889	17.186
b_0	1.914	–	–

Table B.12. Dust effects $corr^{dust}$, as in Table B.11, but in V band.

Disk (Sérsic fits); V band

	$\frac{R_{app}}{R_i}$	ΔSB	n_{app}^{sers}
$\tau_B^f = 0.1$			
a_0	0.996	-0.073	1.002
a_1	0.030	2.129	-0.182
a_2	-0.271	-18.625	1.108
a_3	0.932	60.194	-3.893
a_4	-1.334	-80.297	5.541
a_5	0.714	38.186	-3.026
$\tau_B^f = 0.3$			
a_0	0.993	-0.063	0.993
a_1	0.045	2.638	-0.113
a_2	-0.395	-25.476	0.591
a_3	1.489	87.379	-2.464
a_4	-2.249	-119.994	3.709
a_5	1.297	58.553	-2.226
$\tau_B^f = 0.5$			
a_0	0.993	-0.040	0.979
a_1	0.043	2.347	0.090
a_2	-0.393	-21.559	-1.267
a_3	1.682	74.742	3.511
a_4	-2.686	-103.175	-4.456
a_5	1.634	51.468	1.726
$\tau_B^f = 1.0$			
a_0	0.995	0.027	0.953
a_1	0.143	3.812	0.320
a_2	-1.396	-30.914	-4.416
a_3	5.636	103.901	15.434
a_4	-8.588	-139.285	-22.605
a_5	4.738	67.656	11.295
$\tau_B^f = 2.0$			
a_0	1.014	0.405	0.889
a_1	-0.041	4.579	0.039
a_2	0.577	-37.239	-2.297
a_3	-0.384	134.507	8.525
a_4	-0.828	-187.320	-13.661
a_5	1.332	91.712	7.669
$\tau_B^f = 4.0$			
a_0	1.067	1.221	0.784
a_1	-0.117	6.442	-0.432
a_2	2.347	-48.673	2.099
a_3	-6.991	170.863	-6.111
a_4	9.211	-239.758	7.741
a_5	-3.855	118.370	-3.032
$\tau_B^f = 8.0$			
a_0	1.170	2.305	0.691
a_1	0.328	5.584	0.551
a_2	-0.744	-37.821	-5.302
a_3	2.194	125.151	18.248
a_4	-0.993	-174.691	-22.781
a_5	-0.404	88.842	9.689
b_0	1.734	–	–

Table B.13. Dust effects $corr^{dust}$, as in Table B.11, but in I band.

Disk (Sérsic fits); I band

	$\frac{R_{app}}{R_i}$	ΔSB	n_{app}^{sers}
$\tau_B^f = 0.1$			
a_0	0.998	-0.044	1.001
a_1	0.005	0.836	-0.110
a_2	-0.065	-7.329	0.362
a_3	0.294	23.507	-1.198
a_4	-0.478	-30.968	1.583
a_5	0.285	14.771	-1.000
$\tau_B^f = 0.3$			
a_0	0.994	-0.102	1.000
a_1	0.022	2.777	-0.192
a_2	-0.185	-24.179	1.045
a_3	0.765	79.406	-3.402
a_4	-1.205	-107.268	4.523
a_5	0.723	51.710	-2.420
$\tau_B^f = 0.5$			
a_0	0.993	-0.108	0.991
a_1	0.038	3.564	-0.033
a_2	-0.284	-31.501	-0.197
a_3	1.153	103.483	0.219
a_4	-1.796	-138.234	-0.104
a_5	1.076	65.947	-0.299
$\tau_B^f = 1.0$			
a_0	0.991	-0.072	0.974
a_1	0.126	3.207	0.217
a_2	-1.006	-25.867	-2.983
a_3	3.742	85.774	10.048
a_4	-5.481	-115.619	-14.227
a_5	2.980	56.726	6.767
$\tau_B^f = 2.0$			
a_0	0.997	0.082	0.943
a_1	0.188	4.511	0.285
a_2	-1.357	-35.919	-4.521
a_3	5.193	121.950	16.264
a_4	-7.681	-164.960	-24.092
a_5	4.224	80.136	12.253
$\tau_B^f = 4.0$			
a_0	1.029	0.572	0.863
a_1	0.018	6.053	-0.058
a_2	0.893	-46.157	-0.692
a_3	-2.523	157.560	2.460
a_4	3.283	-213.748	-4.427
a_5	-1.132	102.909	2.974
$\tau_B^f = 8.0$			
a_0	1.103	1.514	0.762
a_1	0.206	6.497	0.022
a_2	0.087	-47.529	-0.630
a_3	-0.788	163.635	1.580
a_4	2.447	-228.405	-0.712
a_5	-1.548	113.085	-0.019
b_0	1.516	–	–

Table B.14. Dust effects $corr^{dust}$, as in Table B.11, but in J band.

Disk (Sérsic fits); J band

	$\frac{R_{app}}{R_i}$	ΔSB	n_{app}^{sers}
$\tau_B^f = 0.1$			
a_0	0.990	-0.022	0.991
a_1	0.158	-0.132	0.143
a_2	-0.877	2.597	-1.399
a_3	2.098	-9.741	3.762
a_4	-2.243	13.065	-4.611
a_5	0.894	-5.539	1.840
$\tau_B^f = 0.3$			
a_0	0.989	-0.032	0.990
a_1	0.158	-0.149	0.018
a_2	-0.901	2.272	-0.361
a_3	2.280	-5.536	0.536
a_4	-2.572	3.323	-0.382
a_5	1.107	1.290	-0.155
$\tau_B^f = 0.5$			
a_0	0.989	-0.049	0.991
a_1	0.166	0.531	-0.049
a_2	-0.981	-3.416	0.150
a_3	2.622	12.386	-0.991
a_4	-3.094	-19.444	1.451
a_5	1.399	11.707	-0.931
$\tau_B^f = 1.0$			
a_0	0.996	-0.042	0.987
a_1	0.066	1.180	-0.046
a_2	-0.548	-9.131	-0.280
a_3	2.056	32.105	0.897
a_4	-2.975	-46.121	-1.467
a_5	1.599	24.969	0.546
$\tau_B^f = 2.0$			
a_0	0.986	-0.022	0.966
a_1	0.378	3.265	0.262
a_2	-2.632	-26.149	-3.543
a_3	8.165	87.412	12.589
a_4	-10.676	-118.301	-18.537
a_5	5.172	58.245	9.199
$\tau_B^f = 4.0$			
a_0	0.999	0.175	0.928
a_1	0.381	5.298	0.425
a_2	-2.277	-41.000	-4.877
a_3	6.996	133.928	16.352
a_4	-9.024	-176.144	-23.504
a_5	4.464	83.760	11.869
$\tau_B^f = 8.0$			
a_0	1.044	0.711	0.873
a_1	0.277	5.220	-0.141
a_2	-1.082	-36.255	0.056
a_3	3.213	121.875	0.205
a_4	-3.534	-164.571	-1.115
a_5	1.620	80.321	1.203
b_0	1.417	–	–

Table B.15. Dust effects $corr^{dust}$, as in Table B.11, but in K band.

Disk (Sérsic fits); K band

	$\frac{R_{app}}{R_i}$	ΔSB	n_{app}^{sers}
$\tau_B^f = 0.1$			
a_0	1.000	-0.004	1.000
a_1	-0.003	0.362	-0.018
a_2	0.016	-3.375	-0.756
a_3	-0.015	10.413	2.705
a_4	-0.012	-13.219	-4.034
a_5	0.019	6.028	1.867
$\tau_B^f = 0.3$			
a_0	1.000	-0.004	1.000
a_1	-0.005	0.336	-0.004
a_2	0.030	-2.616	-0.771
a_3	-0.019	7.521	2.427
a_4	-0.044	-9.168	-3.355
a_5	0.058	4.301	1.435
$\tau_B^f = 0.5$			
a_0	1.000	-0.013	0.998
a_1	-0.007	0.803	-0.065
a_2	0.044	-7.283	-0.100
a_3	-0.023	24.732	0.316
a_4	-0.076	-34.370	-0.758
a_5	0.097	16.966	0.322
$\tau_B^f = 1.0$			
a_0	1.001	-0.014	0.990
a_1	-0.007	1.452	0.051
a_2	0.044	-12.479	-0.999
a_3	0.072	40.648	2.865
a_4	-0.287	-55.139	-3.709
a_5	0.252	27.300	1.483
$\tau_B^f = 2.0$			
a_0	1.002	-0.002	0.990
a_1	0.016	1.973	-0.017
a_2	-0.151	-15.100	-0.740
a_3	0.865	47.400	2.539
a_4	-1.493	-62.524	-3.822
a_5	0.917	30.901	1.741
$\tau_B^f = 4.0$			
a_0	1.006	0.087	0.973
a_1	0.125	1.723	0.222
a_2	-1.087	-14.479	-3.569
a_3	4.214	53.737	13.137
a_4	-6.265	-78.279	-19.515
a_5	3.341	41.376	9.712
$\tau_B^f = 8.0$			
a_0	1.020	0.253	0.945
a_1	0.167	3.285	0.380
a_2	-1.142	-21.763	-4.948
a_3	4.410	71.740	17.391
a_4	-6.501	-97.370	-25.382
a_5	3.535	49.569	12.819
b_0	1.360	–	–

Table B.16. Dust effects $corr^{dust}$ on the derived photometric parameters of the **thin disk**: scale-lengths and central surface brightnesses. Results are listed as coefficients of polynomial fits a_k (Eq. 14) at different τ_B^f and at 912Å.

Thin Disk (exponential fits); 912Å

	$\frac{R_{app}}{R_i}$	ΔSB
$\tau_B^f = 0.1$		
a_0	1.025	0.238
a_1	0.612	-0.557
a_2	-5.679	5.783
a_3	20.339	-13.798
a_4	-29.505	12.592
a_5	15.288	-0.727
$\tau_B^f = 0.3$		
a_0	1.096	0.628
a_1	1.058	1.292
a_2	-9.435	-4.892
a_3	35.353	25.837
a_4	-53.075	-45.920
a_5	28.711	31.399
$\tau_B^f = 0.5$		
a_0	1.176	1.026
a_1	1.096	2.155
a_2	-9.227	-5.062
a_3	37.412	22.126
a_4	-59.843	-36.171
a_5	34.669	26.218
$\tau_B^f = 1.0$		
a_0	1.356	1.928
a_1	2.340	4.346
a_2	-19.238	-14.232
a_3	76.913	50.135
a_4	-123.527	-69.942
a_5	72.592	41.298
$\tau_B^f = 2.0$		
a_0	–	–
a_1	–	–
a_2	–	–
a_3	–	–
a_4	–	–
a_5	–	–
$\tau_B^f = 4.0$		
a_0	–	–
a_1	–	–
a_2	–	–
a_3	–	–
a_4	–	–
a_5	–	–
$\tau_B^f = 8.0$		
a_0	–	–
a_1	–	–
a_2	–	–
a_3	–	–
a_4	–	–
a_5	–	–

Table B.17. Dust effects $corr^{dust}$, as in Table B.16, but at 1350Å.

Thin Disk (exponential fits); 1350Å

	$\frac{R_{app}}{R_i}$	ΔSB
$\tau_B^f = 0.1$		
a_0	1.008	0.105
a_1	0.431	-1.436
a_2	-4.047	16.665
a_3	14.298	-55.731
a_4	-20.601	72.612
a_5	10.593	-30.452
$\tau_B^f = 0.3$		
a_0	1.043	0.297
a_1	0.791	-0.097
a_2	-7.440	6.649
a_3	27.333	-19.443
a_4	-40.348	20.507
a_5	21.340	-2.430
$\tau_B^f = 0.5$		
a_0	1.081	0.540
a_1	0.985	1.190
a_2	-8.997	-5.326
a_3	33.861	25.912
a_4	-50.891	-44.371
a_5	27.550	30.185
$\tau_B^f = 1.0$		
a_0	1.169	1.066
a_1	2.141	2.646
a_2	-19.501	-11.187
a_3	73.491	46.183
a_4	-111.042	-70.482
a_5	60.172	43.042
$\tau_B^f = 2.0$		
a_0	1.401	2.035
a_1	0.867	3.980
a_2	-1.995	-8.583
a_3	12.122	30.125
a_4	-25.331	-39.597
a_5	21.825	25.467
$\tau_B^f = 4.0$		
a_0	–	–
a_1	–	–
a_2	–	–
a_3	–	–
a_4	–	–
a_5	–	–
$\tau_B^f = 8.0$		
a_0	–	–
a_1	–	–
a_2	–	–
a_3	–	–
a_4	–	–
a_5	–	–

Table B.18. Dust effects $corr^{dust}$, as in Table B.16, but at 1500Å.

Thin Disk (exponential fits); 1500Å

	$\frac{R_{app}}{R_i}$	ΔSB
$\tau_B^f = 0.1$		
a_0	1.004	0.084
a_1	0.420	-1.226
a_2	-3.944	13.980
a_3	13.839	-46.445
a_4	-19.831	60.230
a_5	10.147	-24.922
$\tau_B^f = 0.3$		
a_0	1.033	0.237
a_1	0.753	-0.277
a_2	-7.137	6.660
a_3	26.201	-16.706
a_4	-38.639	14.387
a_5	20.393	0.912
$\tau_B^f = 0.5$		
a_0	1.066	0.432
a_1	0.920	1.220
a_2	-8.538	-5.787
a_3	32.204	26.737
a_4	-48.409	-44.493
a_5	26.155	29.551
$\tau_B^f = 1.0$		
a_0	1.159	0.933
a_1	0.986	0.839
a_2	-8.441	4.623
a_3	35.277	-5.468
a_4	-57.262	-2.005
a_5	33.608	11.352
$\tau_B^f = 2.0$		
a_0	1.357	1.789
a_1	0.780	4.164
a_2	-1.599	-11.377
a_3	10.129	41.498
a_4	-20.688	-57.003
a_5	17.851	34.224
$\tau_B^f = 4.0$		
a_0	–	–
a_1	–	–
a_2	–	–
a_3	–	–
a_4	–	–
a_5	–	–
$\tau_B^f = 8.0$		
a_0	–	–
a_1	–	–
a_2	–	–
a_3	–	–
a_4	–	–
a_5	–	–

Table B.19. Dust effects $corr^{dust}$, as in Table B.16, but at 1650Å.

Thin Disk (exponential fits); 1650Å

	$\frac{R_{app}}{R_i}$	ΔSB
$\tau_B^f = 0.1$		
a_0	1.001	0.064
a_1	0.406	-1.523
a_2	-3.797	15.694
a_3	13.237	-50.444
a_4	-18.896	64.151
a_5	9.640	-26.392
$\tau_B^f = 0.3$		
a_0	1.024	0.200
a_1	0.710	-0.296
a_2	-6.804	5.411
a_3	24.945	-13.128
a_4	-36.769	11.177
a_5	19.385	1.437
$\tau_B^f = 0.5$		
a_0	1.053	0.321
a_1	0.857	0.896
a_2	-8.095	-1.783
a_3	30.557	10.602
a_4	-45.916	-20.849
a_5	24.761	17.916
$\tau_B^f = 1.0$		
a_0	1.132	0.774
a_1	0.987	1.492
a_2	-8.724	-3.603
a_3	35.796	22.766
a_4	-57.094	-40.579
a_5	32.859	29.342
$\tau_B^f = 2.0$		
a_0	1.316	1.570
a_1	0.707	4.048
a_2	-0.006	-8.385
a_3	3.119	29.322
a_4	-9.095	-39.432
a_5	10.836	25.428
$\tau_B^f = 4.0$		
a_0	–	–
a_1	–	–
a_2	–	–
a_3	–	–
a_4	–	–
a_5	–	–
$\tau_B^f = 8.0$		
a_0	–	–
a_1	–	–
a_2	–	–
a_3	–	–
a_4	–	–
a_5	–	–

Table B.20. Dust effects $corr^{dust}$, as in Table B.16, but at 2000Å.

Thin Disk (exponential fits); 2000Å

	$\frac{R_{app}}{R_i}$	ΔSB
$\tau_B^f = 0.1$		
a_0	0.999	0.040
a_1	0.441	-1.159
a_2	-4.126	13.118
a_3	14.467	-43.311
a_4	-20.727	56.216
a_5	10.616	-23.116
$\tau_B^f = 0.3$		
a_0	1.023	0.230
a_1	0.764	-1.520
a_2	-7.235	14.229
a_3	26.621	-35.838
a_4	-39.324	35.887
a_5	20.812	-7.620
$\tau_B^f = 0.5$		
a_0	1.055	0.325
a_1	0.914	1.547
a_2	-8.474	-7.152
a_3	32.139	28.827
a_4	-48.450	-44.874
a_5	26.273	29.142
$\tau_B^f = 1.0$		
a_0	1.151	0.820
a_1	0.848	0.964
a_2	-6.903	6.136
a_3	30.565	-12.717
a_4	-51.311	11.037
a_5	31.110	3.928
$\tau_B^f = 2.0$		
a_0	1.388	1.828
a_1	1.070	4.501
a_2	-2.240	-9.516
a_3	11.543	31.803
a_4	-22.974	-42.024
a_5	19.749	26.735
$\tau_B^f = 4.0$		
a_0	–	–
a_1	–	–
a_2	–	–
a_3	–	–
a_4	–	–
a_5	–	–
$\tau_B^f = 8.0$		
a_0	–	–
a_1	–	–
a_2	–	–
a_3	–	–
a_4	–	–
a_5	–	–

Table B.21. Dust effects $corr^{dust}$, as in Table B.16, but at 2200Å.

Thin Disk (exponential fits); 2200Å

	$\frac{R_{app}}{R_i}$	ΔSB
$\tau_B^f = 0.1$		
a_0	1.000	0.058
a_1	0.480	-1.337
a_2	-4.478	14.927
a_3	15.732	-48.808
a_4	-22.541	62.773
a_5	11.546	-25.547
$\tau_B^f = 0.3$		
a_0	1.029	0.212
a_1	0.822	-0.640
a_2	-7.653	10.231
a_3	28.202	-26.585
a_4	-41.722	26.286
a_5	22.143	-3.584
$\tau_B^f = 0.5$		
a_0	1.067	0.416
a_1	0.971	0.855
a_2	-8.789	-2.116
a_3	33.499	17.848
a_4	-50.765	-35.186
a_5	27.721	26.628
$\tau_B^f = 1.0$		
a_0	1.183	0.952
a_1	0.662	1.392
a_2	-4.824	4.614
a_3	24.674	-8.654
a_4	-45.213	6.739
a_5	29.510	5.524
$\tau_B^f = 2.0$		
a_0	1.434	2.018
a_1	1.322	5.194
a_2	-3.768	-11.877
a_3	17.879	36.876
a_4	-34.457	-46.861
a_5	27.841	28.553
$\tau_B^f = 4.0$		
a_0	–	–
a_1	–	–
a_2	–	–
a_3	–	–
a_4	–	–
a_5	–	–
$\tau_B^f = 8.0$		
a_0	–	–
a_1	–	–
a_2	–	–
a_3	–	–
a_4	–	–
a_5	–	–

Table B.22. Dust effects $corr^{dust}$, as in Table B.16, but at 2500Å.

Thin Disk (exponential fits); 2500Å

	$\frac{R_{app}}{R_i}$	ΔSB
$\tau_B^f = 0.1$		
a_0	0.992	0.008
a_1	0.401	-2.140
a_2	-3.752	21.033
a_3	13.031	-67.001
a_4	-18.536	84.758
a_5	9.433	-35.062
$\tau_B^f = 0.3$		
a_0	1.002	0.034
a_1	0.707	0.755
a_2	-6.727	-4.914
a_3	24.468	20.312
a_4	-35.873	-32.638
a_5	18.842	21.546
$\tau_B^f = 0.5$		
a_0	1.022	0.155
a_1	0.835	0.015
a_2	-7.878	2.954
a_3	29.564	-1.692
a_4	-44.193	-5.974
a_5	23.724	11.273
$\tau_B^f = 1.0$		
a_0	1.093	0.454
a_1	0.940	2.038
a_2	-7.505	-5.296
a_3	31.341	26.848
a_4	-50.467	-44.363
a_5	29.269	30.151
$\tau_B^f = 2.0$		
a_0	1.320	1.481
a_1	2.043	3.998
a_2	-14.879	-11.417
a_3	59.082	45.016
a_4	-94.459	-67.070
a_5	55.804	41.290
$\tau_B^f = 4.0$		
a_0	–	–
a_1	–	–
a_2	–	–
a_3	–	–
a_4	–	–
a_5	–	–
$\tau_B^f = 8.0$		
a_0	–	–
a_1	–	–
a_2	–	–
a_3	–	–
a_4	–	–
a_5	–	–

Table B.23. Dust effects $corr^{dust}$, as in Table B.16, but at 2800Å.

Thin Disk (exponential fits); 2800Å

	$\frac{R_{app}}{R_i}$	ΔSB
$\tau_B^f = 0.1$		
a_0	0.988	-0.029
a_1	0.468	-1.246
a_2	-4.414	14.170
a_3	15.151	-48.559
a_4	-21.310	64.367
a_5	10.664	-27.452
$\tau_B^f = 0.3$		
a_0	0.994	-0.012
a_1	0.647	0.137
a_2	-6.224	0.884
a_3	22.485	0.041
a_4	-32.824	-5.379
a_5	17.154	8.639
$\tau_B^f = 0.5$		
a_0	1.007	0.076
a_1	0.759	-0.846
a_2	-7.325	10.043
a_3	27.334	-25.567
a_4	-40.679	25.306
a_5	21.704	-3.076
$\tau_B^f = 1.0$		
a_0	1.059	0.306
a_1	0.934	0.357
a_2	-7.758	7.293
a_3	31.384	-14.306
a_4	-49.226	10.369
a_5	27.730	4.661
$\tau_B^f = 2.0$		
a_0	1.262	1.153
a_1	1.438	3.819
a_2	-9.505	-12.382
a_3	38.355	48.800
a_4	-61.693	-73.241
a_5	37.055	44.461
$\tau_B^f = 4.0$		
a_0	–	–
a_1	–	–
a_2	–	–
a_3	–	–
a_4	–	–
a_5	–	–
$\tau_B^f = 8.0$		
a_0	–	–
a_1	–	–
a_2	–	–
a_3	–	–
a_4	–	–
a_5	–	–

Table B.24. Dust effects $corr^{dust}$, as in Table B.16, but at 3600Å.

Thin Disk (exponential fits); 3600Å

	$\frac{R_{app}}{R_i}$	ΔSB
$\tau_B^f = 0.1$		
a_0	1.014	0.175
a_1	0.272	-2.847
a_2	-2.475	27.088
a_3	8.762	-84.574
a_4	-12.570	106.574
a_5	6.415	-45.439
$\tau_B^f = 0.3$		
a_0	1.044	0.324
a_1	0.661	0.059
a_2	-5.910	4.178
a_3	21.100	-10.477
a_4	-30.519	8.858
a_5	15.773	0.805
$\tau_B^f = 0.5$		
a_0	1.075	0.569
a_1	0.918	-0.624
a_2	-8.058	10.348
a_3	29.073	-26.076
a_4	-42.463	25.554
a_5	22.254	-4.167
$\tau_B^f = 1.0$		
a_0	1.157	1.018
a_1	1.282	1.022
a_2	-10.829	1.968
a_3	40.590	0.493
a_4	-61.384	-8.681
a_5	33.574	12.854
$\tau_B^f = 2.0$		
a_0	1.321	1.837
a_1	1.640	3.299
a_2	-12.336	-10.668
a_3	48.887	42.317
a_4	-78.133	-63.644
a_5	46.195	39.124
$\tau_B^f = 4.0$		
a_0	–	–
a_1	–	–
a_2	–	–
a_3	–	–
a_4	–	–
a_5	–	–
$\tau_B^f = 8.0$		
a_0	–	–
a_1	–	–
a_2	–	–
a_3	–	–
a_4	–	–
a_5	–	–

Table B.25. Dust effects $corr^{dust}$, as in Table B.16, but in B band.

Thin Disk (exponential fits); B band

	$\frac{R_{app}}{R_i}$	ΔSB
$\tau_B^f = 0.1$		
a_0	0.989	-0.084
a_1	0.304	1.115
a_2	-2.820	-7.785
a_3	9.527	22.418
a_4	-13.308	-29.037
a_5	6.645	14.784
$\tau_B^f = 0.3$		
a_0	0.981	-0.072
a_1	0.705	-0.250
a_2	-6.821	4.195
a_3	23.819	-14.539
a_4	-33.896	17.742
a_5	17.152	-4.332
$\tau_B^f = 0.5$		
a_0	0.980	-0.107
a_1	1.030	1.152
a_2	-10.144	-9.028
a_3	35.941	33.109
a_4	-51.487	-49.928
a_5	26.155	29.625
$\tau_B^f = 1.0$		
a_0	1.008	-0.017
a_1	0.451	0.973
a_2	-4.428	-5.939
a_3	18.618	29.424
a_4	-29.290	-48.859
a_5	16.546	31.756
$\tau_B^f = 2.0$		
a_0	1.125	0.459
a_1	0.662	3.284
a_2	-3.270	-14.923
a_3	14.334	56.927
a_4	-23.998	-83.837
a_5	15.305	48.504
$\tau_B^f = 4.0$		
a_0	–	–
a_1	–	–
a_2	–	–
a_3	–	–
a_4	–	–
a_5	–	–
$\tau_B^f = 8.0$		
a_0	–	–
a_1	–	–
a_2	–	–
a_3	–	–
a_4	–	–
a_5	–	–

Table B.26. Dust effects $corr^{dust}$, as in Table B.16, but in V band.

Thin Disk (exponential fits); V band

	$\frac{R_{app}}{R_i}$	ΔSB
$\tau_B^f = 0.1$		
a_0	0.990	-0.090
a_1	0.227	2.042
a_2	-2.121	-18.066
a_3	7.176	59.015
a_4	-10.017	-80.836
a_5	4.996	39.924
$\tau_B^f = 0.3$		
a_0	0.980	-0.082
a_1	0.562	-0.652
a_2	-5.369	7.347
a_3	18.583	-25.571
a_4	-26.304	34.385
a_5	13.259	-13.553
$\tau_B^f = 0.5$		
a_0	0.976	-0.114
a_1	0.825	0.330
a_2	-8.006	-2.191
a_3	28.105	9.075
a_4	-40.081	-15.884
a_5	20.309	12.349
$\tau_B^f = 1.0$		
a_0	0.991	-0.222
a_1	0.324	7.145
a_2	-3.202	-67.282
a_3	13.186	235.223
a_4	-20.885	-331.860
a_5	12.005	166.771
$\tau_B^f = 2.0$		
a_0	1.043	0.101
a_1	1.040	2.673
a_2	-7.848	-11.694
a_3	30.160	45.596
a_4	-46.295	-69.664
a_5	25.748	42.168
$\tau_B^f = 4.0$		
a_0	–	–
a_1	–	–
a_2	–	–
a_3	–	–
a_4	–	–
a_5	–	–
$\tau_B^f = 8.0$		
a_0	–	–
a_1	–	–
a_2	–	–
a_3	–	–
a_4	–	–
a_5	–	–

Table B.27. Dust effects $corr^{dust}$, as in Table B.16, but in I band.

Thin Disk (exponential fits); I band

	$\frac{R_{app}}{R_i}$	ΔSB
$\tau_B^f = 0.1$		
a_0	0.994	-0.040
a_1	0.105	0.842
a_2	-1.084	-8.802
a_3	3.863	31.279
a_4	-5.539	-44.841
a_5	2.813	22.743
$\tau_B^f = 0.3$		
a_0	0.985	-0.018
a_1	0.316	-2.304
a_2	-3.140	19.246
a_3	11.102	-58.373
a_4	-15.875	72.471
a_5	8.052	-29.911
$\tau_B^f = 0.5$		
a_0	0.978	-0.070
a_1	0.520	-2.038
a_2	-5.059	19.207
a_3	17.823	-61.176
a_4	-25.443	78.691
a_5	12.894	-32.947
$\tau_B^f = 1.0$		
a_0	0.980	-0.153
a_1	0.286	0.133
a_2	-2.574	0.107
a_3	9.890	4.659
a_4	-15.242	-12.537
a_5	8.603	11.954
$\tau_B^f = 2.0$		
a_0	0.988	-0.149
a_1	0.535	1.272
a_2	-4.533	-7.869
a_3	17.616	35.119
a_4	-27.148	-57.414
a_5	15.239	36.215
$\tau_B^f = 4.0$		
a_0	–	–
a_1	–	–
a_2	–	–
a_3	–	–
a_4	–	–
a_5	–	–
$\tau_B^f = 8.0$		
a_0	–	–
a_1	–	–
a_2	–	–
a_3	–	–
a_4	–	–
a_5	–	–

Table B.28. Dust effects $corr^{dust}$, as in Table B.16, but in J band.

Thin Disk (exponential fits); J band

	$\frac{R_{app}}{R_i}$	ΔSB
$\tau_B^f = 0.1$		
a_0	0.997	-0.026
a_1	0.037	0.277
a_2	-0.426	-3.052
a_3	1.630	12.543
a_4	-2.433	-19.996
a_5	1.271	10.933
$\tau_B^f = 0.3$		
a_0	0.993	-0.047
a_1	0.123	0.648
a_2	-1.333	-7.516
a_3	4.990	29.645
a_4	-7.367	-45.783
a_5	3.820	24.810
$\tau_B^f = 0.5$		
a_0	0.989	-0.028
a_1	0.219	-1.683
a_2	-2.287	14.309
a_3	8.444	-41.563
a_4	-12.367	49.316
a_5	6.376	-19.190
$\tau_B^f = 1.0$		
a_0	0.982	-0.066
a_1	0.481	-2.369
a_2	-4.764	22.219
a_3	17.193	-66.935
a_4	-24.848	82.261
a_5	12.685	-33.320
$\tau_B^f = 2.0$		
a_0	0.986	-0.098
a_1	0.296	-0.140
a_2	-2.644	1.152
a_3	10.382	5.930
a_4	-16.056	-17.966
a_5	9.019	15.560
$\tau_B^f = 4.0$		
a_0	0.998	-0.055
a_1	0.684	0.605
a_2	-5.693	-0.623
a_3	21.244	12.540
a_4	-31.888	-28.081
a_5	17.468	22.590
$\tau_B^f = 8.0$		
a_0	–	–
a_1	–	–
a_2	–	–
a_3	–	–
a_4	–	–
a_5	–	–

Table B.29. Dust effects $corr^{dust}$, as in Table B.16, but in K band.

Thin Disk (exponential fits); K band

	$\frac{R_{app}}{R_i}$	ΔSB
$\tau_B^f = 0.1$		
a_0	0.999	-0.014
a_1	0.030	0.017
a_2	-0.254	0.771
a_3	0.854	-3.193
a_4	-1.188	4.237
a_5	0.591	-1.691
$\tau_B^f = 0.3$		
a_0	0.996	-0.040
a_1	0.085	0.998
a_2	-0.738	-8.630
a_3	2.502	28.676
a_4	-3.495	-39.329
a_5	1.743	19.170
$\tau_B^f = 0.5$		
a_0	0.994	-0.064
a_1	0.136	1.304
a_2	-1.193	-10.857
a_3	4.077	36.415
a_4	-5.720	-50.806
a_5	2.860	25.267
$\tau_B^f = 1.0$		
a_0	0.991	-0.092
a_1	0.246	1.400
a_2	-2.226	-10.228
a_3	7.742	34.169
a_4	-10.967	-48.803
a_5	5.520	25.370
$\tau_B^f = 2.0$		
a_0	0.989	-0.051
a_1	0.434	-2.004
a_2	-4.094	22.106
a_3	14.516	-70.488
a_4	-20.775	89.315
a_5	10.527	-37.422
$\tau_B^f = 4.0$		
a_0	0.991	-0.049
a_1	0.809	0.100
a_2	-7.737	3.641
a_3	27.605	-9.946
a_4	-39.618	9.338
a_5	20.102	0.334
$\tau_B^f = 8.0$		
a_0	1.019	0.046
a_1	0.439	1.840
a_2	-3.783	-13.813
a_3	15.089	58.069
a_4	-23.572	-91.974
a_5	13.345	52.943

Table B.30. Dust effects $corr^{dust}$, as in Table B.16, but for the $H\alpha$ line.

Thin Disk (exponential fits); $H\alpha$

	$\frac{R_{app}}{R_i}$	ΔSB
$\tau_B^f = 0.1$		
a_0	0.992	-0.072
a_1	0.181	1.590
a_2	-1.731	-14.576
a_3	5.928	48.566
a_4	-8.330	-67.275
a_5	4.174	33.452
$\tau_B^f = 0.3$		
a_0	0.982	-0.058
a_1	0.469	-1.275
a_2	-4.529	11.830
a_3	15.765	-37.929
a_4	-22.375	48.733
a_5	11.297	-19.716
$\tau_B^f = 0.5$		
a_0	0.977	-0.098
a_1	0.710	-0.562
a_2	-6.896	5.870
a_3	24.232	-17.391
a_4	-34.567	19.746
a_5	17.516	-4.715
$\tau_B^f = 1.0$		
a_0	0.987	-0.196
a_1	0.310	4.503
a_2	-2.966	-41.894
a_3	11.944	148.362
a_4	-18.759	-211.560
a_5	10.724	108.446
$\tau_B^f = 2.0$		
a_0	1.022	0.015
a_1	0.850	1.605
a_2	-6.599	-4.982
a_3	25.435	23.761
a_4	-39.081	-40.432
a_5	21.789	28.152
$\tau_B^f = 4.0$		
a_0	–	–
a_1	–	–
a_2	–	–
a_3	–	–
a_4	–	–
a_5	–	–
$\tau_B^f = 8.0$		
a_0	–	–
a_1	–	–
a_2	–	–
a_3	–	–
a_4	–	–
a_5	–	–

Table B.31. Dust effects $corr^{dust}$ on the derived photometric parameters of the **thin disk**: effective radius, central surface brightnesses and Sérsic index. Results are listed as coefficients of polynomial fits a_k (Eq. 14) at different τ_B^f and at 912Å.

Thin Disk (Sérsic fits); 912Å

	$\frac{R_{app}}{R_i}$	ΔSB	n_{app}^{sers}
$\tau_B^f = 0.1$			
a_0	1.009	0.277	0.964
a_1	0.378	-0.892	-0.254
a_2	-3.454	12.056	2.360
a_3	12.052	-33.435	-8.939
a_4	-17.179	34.303	13.209
a_5	8.743	-7.513	-7.054
$\tau_B^f = 0.3$			
a_0	1.042	0.801	0.892
a_1	0.481	0.757	-0.114
a_2	-4.122	5.509	-0.056
a_3	14.788	-14.876	-0.904
a_4	-21.350	17.520	1.820
a_5	11.141	-1.621	-1.525
$\tau_B^f = 0.5$			
a_0	1.078	1.370	0.826
a_1	0.481	0.697	-0.172
a_2	-4.122	10.704	-0.671
a_3	14.788	-27.731	2.002
a_4	-21.350	32.454	-3.182
a_5	11.141	-7.546	1.330
$\tau_B^f = 1.0$			
a_0	1.152	2.473	0.696
a_1	0.170	4.699	-0.610
a_2	0.596	-13.554	1.828
a_3	-1.009	50.192	-5.388
a_4	0.409	-71.104	6.447
a_5	0.798	40.843	-3.069
$\tau_B^f = 2.0$			
a_0	1.279	4.156	0.516
a_1	0.226	5.857	-0.857
a_2	1.218	-11.610	4.080
a_3	-4.399	35.626	-13.232
a_4	7.392	-46.473	18.242
a_5	-3.819	27.968	-9.272
$\tau_B^f = 4.0$			
a_0	–	–	–
a_1	–	–	–
a_2	–	–	–
a_3	–	–	–
a_4	–	–	–
a_5	–	–	–
$\tau_B^f = 8.0$			
a_0	–	–	–
a_1	–	–	–
a_2	–	–	–
a_3	–	–	–
a_4	–	–	–
a_5	–	–	–

Table B.32. Dust effects $corr^{dust}$, as in Table B.31, but at 1350Å.

Thin Disk (Sérsic fits); 1350Å

	$\frac{R_{app}}{R_i}$	ΔSB	n_{app}^{sers}
$\tau_B^f = 0.1$			
a_0	1.001	0.047	0.985
a_1	0.278	4.131	-0.301
a_2	-2.535	-38.595	3.022
a_3	8.708	134.298	-11.223
a_4	-12.362	-190.641	16.596
a_5	6.280	96.236	-8.710
$\tau_B^f = 0.3$			
a_0	1.018	0.422	0.945
a_1	0.298	-0.570	-0.322
a_2	-2.694	11.027	2.854
a_3	9.852	-31.606	-10.893
a_4	-14.577	35.591	15.755
a_5	7.807	-8.433	-8.230
$\tau_B^f = 0.5$			
a_0	1.037	0.679	0.912
a_1	0.251	0.640	-0.268
a_2	-2.051	4.335	1.413
a_3	7.875	-8.661	-5.879
a_4	-11.947	6.903	8.670
a_5	6.697	4.273	-4.800
$\tau_B^f = 1.0$			
a_0	1.081	1.398	0.821
a_1	0.246	1.126	-0.478
a_2	-1.451	9.271	2.014
a_3	5.914	-24.267	-7.227
a_4	-8.833	29.458	9.663
a_5	5.080	-6.507	-4.837
$\tau_B^f = 2.0$			
a_0	1.155	2.580	0.666
a_1	0.265	5.532	-0.586
a_2	0.231	-17.902	1.417
a_3	-0.679	63.611	-4.186
a_4	0.930	-88.919	5.082
a_5	0.216	49.377	-2.495
$\tau_B^f = 4.0$			
a_0	–	–	–
a_1	–	–	–
a_2	–	–	–
a_3	–	–	–
a_4	–	–	–
a_5	–	–	–
$\tau_B^f = 8.0$			
a_0	–	–	–
a_1	–	–	–
a_2	–	–	–
a_3	–	–	–
a_4	–	–	–
a_5	–	–	–

Table B.33. Dust effects $corr^{dust}$, as in Table B.31, but at 1500Å.

Thin Disk (Sérsic fits); 1500Å

	$\frac{R_{app}}{R_i}$	ΔSB	n_{app}^{sers}
$\tau_B^f = 0.1$			
a_0	1.001	0.064	0.984
a_1	0.150	1.670	-0.020
a_2	-1.264	-15.136	0.530
a_3	4.302	53.938	-3.148
a_4	-6.186	-78.692	5.618
a_5	3.272	41.979	-3.410
$\tau_B^f = 0.3$			
a_0	1.014	0.330	0.951
a_1	0.235	0.102	-0.010
a_2	-2.108	3.307	-0.190
a_3	7.840	-4.150	-0.883
a_4	-11.809	-3.059	2.577
a_5	6.480	9.980	-2.190
$\tau_B^f = 0.5$			
a_0	1.031	0.606	0.920
a_1	0.135	0.366	-0.159
a_2	-0.996	2.250	0.414
a_3	4.334	2.558	-2.265
a_4	-7.134	-11.701	3.493
a_5	4.407	14.170	-2.252
$\tau_B^f = 1.0$			
a_0	1.068	1.192	0.839
a_1	0.246	2.551	-0.372
a_2	-1.622	-6.502	0.918
a_3	6.604	29.512	-3.316
a_4	-9.941	-44.610	4.157
a_5	5.678	28.864	-2.181
$\tau_B^f = 2.0$			
a_0	1.137	2.325	0.687
a_1	0.123	5.650	-0.646
a_2	0.968	-19.041	1.967
a_3	-2.156	66.528	-6.326
a_4	2.028	-91.481	8.224
a_5	0.025	49.887	-4.020
$\tau_B^f = 4.0$			
a_0	1.257	4.058	0.491
a_1	0.443	8.584	-1.088
a_2	-0.154	-25.036	4.581
a_3	-0.139	67.987	-13.238
a_4	1.643	-83.571	17.536
a_5	-1.045	44.101	-8.748
$\tau_B^f = 8.0$			
a_0	–	–	–
a_1	–	–	–
a_2	–	–	–
a_3	–	–	–
a_4	–	–	–
a_5	–	–	–

Table B.34. Dust effects $corr^{dust}$, as in Table B.31, but at 1650Å.

Thin Disk (Sérsic fits); 1650Å

	$\frac{R_{app}}{R_i}$	ΔSB	n_{app}^{sers}
$\tau_B^f = 0.1$			
a_0	0.997	-0.006	0.997
a_1	0.236	3.877	-0.413
a_2	-2.098	-36.566	3.877
a_3	7.065	126.647	-13.712
a_4	-9.922	-179.338	19.641
a_5	5.027	90.341	-9.991
$\tau_B^f = 0.3$			
a_0	1.070	0.225	0.965
a_1	-0.802	0.333	-0.281
a_2	3.306	3.406	2.399
a_3	-4.236	-8.225	-9.338
a_4	0.181	4.178	13.927
a_5	2.107	6.227	-7.523
$\tau_B^f = 0.5$			
a_0	1.022	0.494	0.935
a_1	0.208	-0.234	-0.312
a_2	-1.822	9.213	2.023
a_3	7.190	-24.280	-7.916
a_4	-11.164	26.811	11.635
a_5	6.371	-4.537	-6.313
$\tau_B^f = 1.0$			
a_0	1.056	1.009	0.859
a_1	0.176	1.903	-0.403
a_2	-1.126	-3.370	1.545
a_3	4.973	22.405	-5.646
a_4	-7.808	-37.435	7.272
a_5	4.719	26.134	-3.581
$\tau_B^f = 2.0$			
a_0	1.113	2.096	0.710
a_1	0.137	5.286	-0.901
a_2	0.580	-12.481	2.473
a_3	-0.670	42.841	-6.338
a_4	-0.114	-60.495	7.596
a_5	1.085	36.223	-3.616
$\tau_B^f = 4.0$			
a_0	1.232	3.980	0.470
a_1	0.500	7.302	-0.876
a_2	-0.576	-21.113	3.245
a_3	1.231	63.224	-8.606
a_4	-0.437	-81.930	10.542
a_5	0.109	44.278	-5.049
$\tau_B^f = 8.0$			
a_0	–	–	–
a_1	–	–	–
a_2	–	–	–
a_3	–	–	–
a_4	–	–	–
a_5	–	–	–

Table B.35. Dust effects $corr^{dust}$, as in Table B.31, but at 2000Å.

Thin Disk (Sérsic fits); 2000Å

	$\frac{R_{app}}{R_i}$	ΔSB	n_{app}^{sers}
$\tau_B^f = 0.1$			
a_0	0.995	-0.008	0.997
a_1	0.285	3.753	-0.410
a_2	-2.580	-36.012	3.842
a_3	8.764	126.654	-13.620
a_4	-12.333	-180.907	19.483
a_5	6.230	91.874	-9.927
$\tau_B^f = 0.3$			
a_0	1.006	0.259	0.957
a_1	0.281	-0.401	-0.215
a_2	-2.520	9.726	1.933
a_3	9.237	-28.059	-8.078
a_4	-13.718	31.554	12.321
a_5	7.409	-6.765	-6.793
$\tau_B^f = 0.5$			
a_0	1.021	0.508	0.925
a_1	0.223	-0.019	-0.307
a_2	-1.830	7.585	2.088
a_3	7.189	-17.210	-8.384
a_4	-11.065	17.346	12.172
a_5	6.310	-0.188	-6.455
$\tau_B^f = 1.0$			
a_0	1.056	1.105	0.833
a_1	0.226	2.397	-0.417
a_2	-1.574	-3.441	1.099
a_3	6.782	21.158	-4.412
a_4	-10.387	-34.370	6.120
a_5	5.960	24.215	-3.195
$\tau_B^f = 2.0$			
a_0	1.115	2.436	0.629
a_1	0.676	6.757	-0.913
a_2	-3.137	-22.838	3.196
a_3	9.494	74.196	-8.392
a_4	-11.733	-100.796	9.906
a_5	5.777	54.414	-4.523
$\tau_B^f = 4.0$			
a_0	1.264	4.394	0.408
a_1	0.685	8.024	-0.803
a_2	-1.485	-27.229	3.987
a_3	3.175	83.257	-12.626
a_4	-2.169	-110.649	17.083
a_5	0.553	59.201	-8.446
$\tau_B^f = 8.0$			
a_0	–	–	–
a_1	–	–	–
a_2	–	–	–
a_3	–	–	–
a_4	–	–	–
a_5	–	–	–

Table B.36. Dust effects $corr^{dust}$, as in Table B.31, but at 2200Å.

Thin Disk (Sérsic fits); 2200Å

	$\frac{R_{app}}{R_i}$	ΔSB	n_{app}^{sers}
$\tau_B^f = 0.1$			
a_0	0.998	0.017	0.992
a_1	0.159	2.313	-0.112
a_2	-1.362	-21.335	0.776
a_3	4.696	77.046	-3.370
a_4	-6.775	-113.025	5.657
a_5	3.598	59.827	-3.446
$\tau_B^f = 0.3$			
a_0	1.009	0.301	0.942
a_1	0.188	0.322	0.144
a_2	-1.518	3.148	-1.499
a_3	5.785	-5.788	2.913
a_4	-8.854	2.372	-2.154
a_5	5.048	6.545	-0.099
$\tau_B^f = 0.5$			
a_0	1.027	0.587	0.909
a_1	0.132	1.147	-0.079
a_2	-0.783	-2.277	-0.330
a_3	3.561	16.310	-0.281
a_4	-5.948	-27.720	1.111
a_5	3.834	20.843	-1.194
$\tau_B^f = 1.0$			
a_0	1.066	1.268	0.811
a_1	0.271	3.389	-0.515
a_2	-1.760	-8.475	1.453
a_3	7.419	33.987	-4.639
a_4	-11.231	-48.892	5.726
a_5	6.344	30.469	-2.827
$\tau_B^f = 2.0$			
a_0	1.145	2.685	0.608
a_1	0.515	6.391	-0.854
a_2	-2.193	-16.420	2.707
a_3	7.357	50.803	-7.327
a_4	-9.451	-67.610	9.260
a_5	4.824	38.181	-4.563
$\tau_B^f = 4.0$			
a_0	1.290	4.693	0.387
a_1	0.745	8.583	-0.677
a_2	-1.610	-30.858	2.635
a_3	2.957	94.014	-7.925
a_4	-1.201	-124.039	10.701
a_5	-0.234	65.111	-5.477
$\tau_B^f = 8.0$			
a_0	–	–	–
a_1	–	–	–
a_2	–	–	–
a_3	–	–	–
a_4	–	–	–
a_5	–	–	–

Table B.37. Dust effects $corr^{dust}$, as in Table B.31, but at 2500Å.

Thin Disk (Sérsic fits); 2500Å

	$\frac{R_{app}}{R_i}$	ΔSB	n_{app}^{sers}
$\tau_B^f = 0.1$			
a_0	0.992	-0.079	0.999
a_1	0.222	3.395	-0.327
a_2	-1.995	-31.101	3.478
a_3	6.721	106.880	-12.913
a_4	-9.424	-151.494	18.877
a_5	4.775	77.064	-9.703
$\tau_B^f = 0.3$			
a_0	0.992	0.081	0.978
a_1	0.327	-0.570	-0.273
a_2	-2.831	8.717	2.463
a_3	9.881	-22.103	-9.851
a_4	-14.245	20.363	14.957
a_5	7.503	-0.546	-8.126
$\tau_B^f = 0.5$			
a_0	1.002	0.232	0.947
a_1	0.228	-0.165	-0.201
a_2	-1.946	8.304	1.548
a_3	7.420	-20.400	-7.064
a_4	-11.291	20.523	11.029
a_5	6.369	-1.054	-6.189
$\tau_B^f = 1.0$			
a_0	1.023	0.730	0.860
a_1	0.205	2.444	-0.335
a_2	-1.753	-4.652	-0.369
a_3	7.414	27.175	0.216
a_4	-11.188	-45.251	0.603
a_5	6.295	29.955	-0.870
$\tau_B^f = 2.0$			
a_0	1.079	2.133	0.628
a_1	0.621	4.914	-0.716
a_2	-2.478	-12.420	2.464
a_3	7.091	43.462	-6.766
a_4	-8.641	-61.328	8.030
a_5	4.444	36.551	-3.686
$\tau_B^f = 4.0$			
a_0	1.234	3.875	0.446
a_1	0.513	7.161	-0.629
a_2	-0.871	-23.633	2.581
a_3	2.335	75.669	-8.643
a_4	-2.201	-101.550	12.146
a_5	1.080	54.322	-6.208
$\tau_B^f = 8.0$			
a_0	–	–	–
a_1	–	–	–
a_2	–	–	–
a_3	–	–	–
a_4	–	–	–
a_5	–	–	–

Table B.38. Dust effects $corr^{dust}$, as in Table B.31, but at 2800Å.

Thin Disk (Sérsic fits); 2800Å

	$\frac{R_{app}}{R_i}$	ΔSB	n_{app}^{sers}
$\tau_B^f = 0.1$			
a_0	0.992	-0.081	1.002
a_1	0.142	2.049	-0.099
a_2	-1.222	-17.308	0.805
a_3	4.041	57.379	-3.302
a_4	-5.671	-80.248	5.370
a_5	2.935	41.373	-3.168
$\tau_B^f = 0.3$			
a_0	0.991	-0.039	0.983
a_1	0.182	2.222	0.043
a_2	-1.564	-17.944	-0.465
a_3	5.546	65.932	0.041
a_4	-8.177	-100.144	1.468
a_5	4.506	56.944	-1.705
$\tau_B^f = 0.5$			
a_0	0.996	0.122	0.964
a_1	0.186	-0.620	-0.009
a_2	-1.623	8.661	-0.470
a_3	6.199	-19.146	0.307
a_4	-9.508	16.618	0.600
a_5	5.436	1.371	-1.140
$\tau_B^f = 1.0$			
a_0	0.991	0.475	0.893
a_1	0.479	2.040	-0.334
a_2	-4.482	-2.496	-0.447
a_3	15.898	19.533	0.432
a_4	-22.856	-34.649	0.504
a_5	11.820	24.634	-0.909
$\tau_B^f = 2.0$			
a_0	1.055	1.762	0.659
a_1	0.251	4.375	-0.554
a_2	0.195	-10.180	1.524
a_3	0.147	35.434	-4.388
a_4	-1.426	-48.635	5.270
a_5	1.871	29.505	-2.495
$\tau_B^f = 4.0$			
a_0	1.196	3.417	0.489
a_1	0.470	5.597	-0.547
a_2	-0.801	-12.589	1.843
a_3	2.353	40.602	-5.712
a_4	-2.511	-52.808	7.049
a_5	1.381	29.884	-3.207
$\tau_B^f = 8.0$			
a_0	1.376	5.285	0.347
a_1	0.790	8.548	-0.918
a_2	-2.126	-28.904	4.933
a_3	5.129	86.346	-15.877
a_4	-4.762	-111.933	21.991
a_5	1.564	58.501	-11.152

Table B.39. Dust effects $corr^{dust}$, as in Table B.31, but at 3600Å.

Thin Disk (Sérsic fits); 3600Å

	$\frac{R_{app}}{R_i}$	ΔSB	n_{app}^{sers}
$\tau_B^f = 0.1$			
a_0	1.005	0.112	0.984
a_1	0.240	2.417	-0.240
a_2	-2.257	-22.913	2.424
a_3	7.868	81.680	-9.122
a_4	-11.132	-117.263	13.530
a_5	5.556	59.523	-7.037
$\tau_B^f = 0.3$			
a_0	1.020	0.457	0.955
a_1	0.450	-1.156	-0.297
a_2	-4.105	14.323	2.325
a_3	14.367	-39.806	-8.548
a_4	-20.399	43.268	12.561
a_5	10.272	-12.185	-6.730
$\tau_B^f = 0.5$			
a_0	1.035	0.665	0.921
a_1	0.534	0.254	-0.284
a_2	-4.716	7.190	1.664
a_3	16.577	-19.958	-5.993
a_4	-23.632	21.131	8.644
a_5	12.011	-2.850	-4.788
$\tau_B^f = 1.0$			
a_0	1.069	1.293	0.850
a_1	0.729	1.094	-0.183
a_2	-5.946	4.517	-0.328
a_3	20.450	-9.656	0.784
a_4	-28.585	9.771	-0.998
a_5	14.385	1.829	-0.028
$\tau_B^f = 2.0$			
a_0	1.144	2.295	0.729
a_1	0.347	3.082	-0.328
a_2	-1.697	-1.890	-0.033
a_3	6.809	10.353	0.087
a_4	-10.331	-16.644	-0.445
a_5	5.855	14.772	-0.036
$\tau_B^f = 4.0$			
a_0	1.263	3.793	0.570
a_1	0.452	5.965	-0.600
a_2	-1.766	-15.504	1.531
a_3	5.931	47.464	-4.589
a_4	-7.369	-59.379	6.065
a_5	3.644	31.722	-3.239
$\tau_B^f = 8.0$			
a_0	1.405	5.686	0.407
a_1	0.689	8.121	-0.921
a_2	-1.852	-25.809	3.991
a_3	4.623	76.490	-11.790
a_4	-4.297	-99.657	15.526
a_5	1.481	52.955	-7.748

Table B.40. Dust effects $corr^{dust}$, as in Table B.31, but in B band.

Thin Disk (Sérsic fits); B band

	$\frac{R_{app}}{R_i}$	ΔSB	n_{app}^{sers}
$\tau_B^f = 0.1$			
a_0	0.991	-0.107	1.003
a_1	0.207	2.751	-0.223
a_2	-1.884	-24.886	2.352
a_3	6.221	83.164	-8.472
a_4	-8.577	-115.570	12.209
a_5	4.238	57.476	-6.252
$\tau_B^f = 0.3$			
a_0	0.983	-0.093	0.995
a_1	0.439	0.848	-0.074
a_2	-4.071	-7.054	1.279
a_3	13.746	27.210	-6.406
a_4	-19.182	-44.258	10.890
a_5	9.579	27.854	-6.320
$\tau_B^f = 0.5$			
a_0	0.982	-0.048	0.985
a_1	0.420	-1.003	-0.063
a_2	-3.933	10.845	1.051
a_3	13.591	-29.587	-5.455
a_4	-19.296	30.622	9.153
a_5	9.868	-5.446	-5.407
$\tau_B^f = 1.0$			
a_0	0.987	0.039	0.963
a_1	0.308	0.328	-0.215
a_2	-3.136	3.427	1.272
a_3	11.627	-0.455	-7.250
a_4	-17.232	-6.626	11.480
a_5	9.332	10.809	-6.085
$\tau_B^f = 2.0$			
a_0	0.987	0.876	0.769
a_1	0.308	2.901	-0.352
a_2	-3.136	-2.187	-0.288
a_3	11.627	8.549	1.507
a_4	-17.232	-11.794	-2.585
a_5	9.332	11.483	1.130
$\tau_B^f = 4.0$			
a_0	1.101	2.201	0.607
a_1	0.688	4.862	-0.435
a_2	-3.269	-12.995	0.981
a_3	9.996	46.034	-3.102
a_4	-12.760	-63.563	3.549
a_5	6.409	36.644	-1.606
$\tau_B^f = 8.0$			
a_0	1.261	3.889	0.466
a_1	0.398	6.332	-0.807
a_2	-0.022	-13.992	3.220
a_3	-0.104	40.218	-8.834
a_4	1.007	-49.002	10.304
a_5	-0.539	27.453	-4.541

Table B.41. Dust effects $corr^{dust}$, as in Table B.31, but in V band.

Thin Disk (Sérsic fits); V band

	$\frac{R_{app}}{R_i}$	ΔSB	n_{app}^{sers}
$\tau_B^f = 0.1$			
a_0	0.993	-0.087	1.004
a_1	0.152	1.886	-0.259
a_2	-1.426	-17.304	2.662
a_3	4.772	57.824	-9.369
a_4	-6.618	-79.989	13.250
a_5	3.278	39.674	-6.635
$\tau_B^f = 0.3$			
a_0	0.984	-0.158	1.005
a_1	0.322	3.654	-0.292
a_2	-2.986	-34.389	2.882
a_3	10.055	118.403	-10.508
a_4	-14.024	-167.607	15.311
a_5	7.016	85.234	-7.964
$\tau_B^f = 0.5$			
a_0	0.980	-0.121	0.996
a_1	0.408	0.203	-0.088
a_2	-3.813	-0.117	1.253
a_3	13.037	4.624	-6.119
a_4	-18.355	-14.411	10.275
a_5	9.279	14.599	-5.991
$\tau_B^f = 1.0$			
a_0	0.980	-0.071	0.986
a_1	0.355	-0.654	-0.167
a_2	-3.396	9.504	1.243
a_3	12.204	-24.429	-5.989
a_4	-17.844	25.767	9.477
a_5	9.476	-3.724	-5.346
$\tau_B^f = 2.0$			
a_0	0.980	0.352	0.863
a_1	0.355	2.347	-0.677
a_2	-3.396	1.167	1.758
a_3	12.204	-3.939	-4.371
a_4	-17.844	5.003	5.112
a_5	9.476	3.690	-2.536
$\tau_B^f = 4.0$			
a_0	1.051	1.558	0.669
a_1	0.148	4.149	-0.357
a_2	0.644	-11.281	0.771
a_3	-0.416	41.440	-2.827
a_4	-1.507	-57.844	3.396
a_5	2.154	33.876	-1.606
$\tau_B^f = 8.0$			
a_0	1.199	3.069	0.537
a_1	0.123	6.042	-0.739
a_2	1.176	-16.817	2.934
a_3	-2.367	52.442	-8.421
a_4	2.356	-66.216	9.966
a_5	-0.413	35.395	-4.399

Table B.42. Dust effects $corr^{dust}$, as in Table B.31, but in I band.

Thin Disk (Sérsic fits); I band

	$\frac{R_{app}}{R_i}$	ΔSB	n_{app}^{sers}
$\tau_B^f = 0.1$			
a_0	0.996	-0.043	1.003
a_1	0.065	0.802	-0.205
a_2	-0.721	-9.124	2.101
a_3	2.588	33.814	-7.399
a_4	-3.723	-49.267	10.526
a_5	1.888	25.099	-5.310
$\tau_B^f = 0.3$			
a_0	0.990	-0.132	1.012
a_1	0.167	2.698	-0.319
a_2	-1.761	-25.408	2.856
a_3	6.309	87.455	-9.831
a_4	-9.089	-123.235	13.866
a_5	4.632	62.019	-7.025
$\tau_B^f = 0.5$			
a_0	0.985	-0.142	1.005
a_1	0.232	3.000	-0.278
a_2	-2.399	-31.168	2.581
a_3	8.604	113.106	-9.348
a_4	-12.413	-164.137	13.690
a_5	6.355	84.500	-7.207
$\tau_B^f = 1.0$			
a_0	0.977	-0.133	1.006
a_1	0.354	-0.449	-0.319
a_2	-3.398	5.159	2.312
a_3	12.064	-8.813	-8.210
a_4	-17.340	1.525	11.978
a_5	8.925	8.055	-6.485
$\tau_B^f = 2.0$			
a_0	0.973	-0.051	0.973
a_1	0.417	-0.489	-0.310
a_2	-3.780	9.253	1.736
a_3	13.520	-18.610	-6.907
a_4	-19.512	14.556	10.271
a_5	10.222	2.493	-5.598
$\tau_B^f = 4.0$			
a_0	0.971	0.702	0.788
a_1	0.728	2.126	-0.534
a_2	-5.732	0.644	1.753
a_3	20.197	3.109	-5.057
a_4	-28.523	-8.075	6.087
a_5	14.515	10.960	-2.901
$\tau_B^f = 8.0$			
a_0	1.074	1.947	0.628
a_1	0.665	4.144	-0.541
a_2	-2.733	-9.053	1.996
a_3	7.906	35.207	-6.125
a_4	-10.198	-51.156	7.329
a_5	5.430	31.511	-3.284

Table B.43. Dust effects $corr^{dust}$, as in Table B.31, but in J band.

Thin Disk (Sérsic fits); J band

	$\frac{R_{app}}{R_i}$	ΔSB	n_{app}^{sers}
$\tau_B^f = 0.1$			
a_0	0.998	-0.023	1.003
a_1	0.025	-0.099	-0.212
a_2	-0.302	0.802	2.146
a_3	1.155	-1.149	-7.436
a_4	-1.719	-0.483	10.375
a_5	0.892	1.465	-5.114
$\tau_B^f = 0.3$			
a_0	0.995	-0.048	1.003
a_1	0.059	0.317	-0.234
a_2	-0.733	-5.096	2.513
a_3	2.873	23.740	-9.132
a_4	-4.353	-39.637	13.103
a_5	2.294	22.493	-6.586
$\tau_B^f = 0.5$			
a_0	0.992	-0.079	1.003
a_1	0.097	1.572	-0.247
a_2	-1.142	-17.567	2.653
a_3	4.432	66.906	-9.689
a_4	-6.682	-99.598	13.957
a_5	3.515	51.868	-7.090
$\tau_B^f = 1.0$			
a_0	0.987	-0.144	1.004
a_1	0.175	2.832	-0.231
a_2	-1.935	-28.610	2.269
a_3	7.401	106.518	-8.793
a_4	-11.071	-157.063	13.291
a_5	5.812	81.679	-7.109
$\tau_B^f = 2.0$			
a_0	0.982	-0.062	0.999
a_1	0.296	-2.100	-0.489
a_2	-2.983	20.357	3.895
a_3	11.137	-54.545	-13.390
a_4	-16.414	58.711	18.701
a_5	8.573	-17.262	-9.479
$\tau_B^f = 4.0$			
a_0	0.980	0.005	0.967
a_1	0.417	0.419	-0.553
a_2	-3.719	5.381	3.340
a_3	13.581	-12.345	-10.585
a_4	-19.729	12.204	13.954
a_5	10.320	1.442	-6.997
$\tau_B^f = 8.0$			
a_0	0.984	0.597	0.830
a_1	0.723	2.650	-0.743
a_2	-5.800	-0.844	2.838
a_3	20.104	3.477	-7.220
a_4	-27.909	-5.171	8.132
a_5	14.058	8.814	-3.735

Table B.44. Dust effects $corr^{dust}$, as in Table B.31, but in K band.

Thin Disk (Sérsic fits); K band

	$\frac{R_{app}}{R_i}$	ΔSB	n_{app}^{sers}
$\tau_B^f = 0.1$			
a_0	0.999	-0.012	1.003
a_1	0.026	-0.212	-0.216
a_2	-0.207	2.728	2.207
a_3	0.666	-9.511	-7.703
a_4	-0.898	12.815	10.771
a_5	0.435	-5.761	-5.278
$\tau_B^f = 0.3$			
a_0	0.996	-0.031	1.002
a_1	0.065	0.369	-0.176
a_2	-0.548	-2.474	1.952
a_3	1.824	7.928	-7.273
a_4	-2.526	-11.265	10.641
a_5	1.247	6.154	-5.407
$\tau_B^f = 0.5$			
a_0	0.995	-0.066	1.002
a_1	0.100	1.455	-0.182
a_2	-0.848	-12.298	2.011
a_3	2.834	41.314	-7.463
a_4	-3.930	-57.482	10.847
a_5	1.944	28.442	-5.503
$\tau_B^f = 1.0$			
a_0	0.991	-0.113	1.004
a_1	0.171	2.614	-0.263
a_2	-1.472	-21.418	2.396
a_3	4.980	70.571	-8.475
a_4	-6.957	-97.000	12.220
a_5	3.466	47.851	-6.263
$\tau_B^f = 2.0$			
a_0	0.989	-0.136	0.997
a_1	0.247	3.446	-0.172
a_2	-2.234	-28.736	1.933
a_3	7.801	97.948	-7.857
a_4	-11.097	-138.172	12.112
a_5	5.610	69.999	-6.524
$\tau_B^f = 4.0$			
a_0	0.988	-0.044	0.985
a_1	0.325	0.237	-0.299
a_2	-3.043	3.473	2.709
a_3	10.972	-6.861	-10.124
a_4	-15.873	0.978	14.903
a_5	8.150	6.911	-7.878
$\tau_B^f = 8.0$			
a_0	0.995	0.130	0.953
a_1	0.377	-0.396	-0.121
a_2	-3.509	13.318	0.539
a_3	13.065	-39.085	-3.244
a_4	-19.214	46.028	5.827
a_5	10.062	-13.598	-3.779

Table B.45. Dust effects $corr^{dust}$, as in Table B.31, but for the $H\alpha$ line.

Thin Disk (Sérsic fits); $H\alpha$

	$\frac{R_{app}}{R_i}$	ΔSB	n_{app}^{sers}
$\tau_B^f = 0.1$			
a_0	0.994	-0.070	1.003
a_1	0.119	1.478	-0.238
a_2	-1.161	-14.233	2.451
a_3	3.954	48.815	-8.627
a_4	-5.535	-68.462	12.224
a_5	2.758	34.203	-6.136
$\tau_B^f = 0.3$			
a_0	0.986	-0.148	1.007
a_1	0.264	3.294	-0.302
a_2	-2.525	-31.016	2.872
a_3	8.649	106.780	-10.253
a_4	-12.173	-150.938	14.767
a_5	6.122	76.509	-7.610
$\tau_B^f = 0.5$			
a_0	0.982	-0.129	0.999
a_1	0.342	1.257	-0.160
a_2	-3.281	-11.825	1.753
a_3	11.373	45.529	-7.336
a_4	-16.125	-70.865	11.562
a_5	8.181	40.954	-6.449
$\tau_B^f = 1.0$			
a_0	0.979	-0.094	0.994
a_1	0.355	-0.576	-0.224
a_2	-3.397	7.857	1.646
a_3	12.156	-18.510	-6.826
a_4	-17.662	16.587	10.419
a_5	9.272	0.734	-5.775
$\tau_B^f = 2.0$			
a_0	0.973	0.200	0.904
a_1	0.437	1.279	-0.539
a_2	-4.025	4.203	1.750
a_3	15.025	-9.430	-5.326
a_4	-21.934	8.555	7.056
a_5	11.500	3.260	-3.689
$\tau_B^f = 4.0$			
a_0	1.023	1.229	0.714
a_1	0.255	3.797	-0.431
a_2	-0.670	-10.793	1.208
a_3	3.658	40.590	-3.897
a_4	-6.605	-57.795	4.726
a_5	4.382	34.185	-2.245
$\tau_B^f = 8.0$			
a_0	1.152	2.645	0.571
a_1	0.293	5.455	-0.653
a_2	0.057	-15.218	2.465
a_3	0.234	50.713	-7.143
a_4	-0.526	-67.472	8.371
a_5	0.854	37.433	-3.675

Table B.46. Dust effects $corr^{dust}$ on the derived photometric parameters of **exponential bulges**: effective radius and Sérsic index. Results are listed as coefficients of polynomial fits a_k (Eq. 14) at different τ_B^f and the effective wavelength of the B band.

exponential bulges (Sérsic fits); B band

	$\frac{R_{app}}{R_i}$	n_{app}^{sers}
$\tau_B^f = 0.1$		
a_0	1.001	0.761
a_1	0.004	-0.067
a_2	0.105	0.692
a_3	-0.324	-2.486
a_4	0.420	3.620
a_5	-0.167	-1.831
$\tau_B^f = 0.3$		
a_0	1.010	0.763
a_1	-0.013	-0.235
a_2	0.493	2.460
a_3	-1.999	-8.929
a_4	3.247	13.134
a_5	-1.733	-6.712
$\tau_B^f = 0.5$		
a_0	1.018	0.762
a_1	0.007	-0.171
a_2	0.456	1.927
a_3	-1.971	-7.495
a_4	3.323	11.816
a_5	-1.847	-6.479
$\tau_B^f = 1.0$		
a_0	1.029	0.749
a_1	0.181	0.122
a_2	-1.421	-1.758
a_3	4.386	5.735
a_4	-5.055	-6.312
a_5	1.887	1.786
$\tau_B^f = 2.0$		
a_0	1.050	0.739
a_1	-0.060	-0.147
a_2	0.399	0.465
a_3	-0.364	0.523
a_4	-0.249	-2.295
a_5	0.208	0.939
$\tau_B^f = 4.0$		
a_0	1.057	0.728
a_1	-0.039	0.003
a_2	-0.072	-1.633
a_3	0.694	7.464
a_4	-1.076	-12.035
a_5	0.399	5.716
$\tau_B^f = 8.0$		
a_0	1.046	0.697
a_1	-0.043	0.093
a_2	0.548	-2.264
a_3	-2.581	9.270
a_4	5.339	-15.430
a_5	-3.843	7.973

Table B.47. Dust effects $corr^{dust}$, as in Table B.46, but in V band.

exponential bulges (Sérsic fits); V band

	$\frac{R_{app}}{R_i}$	n_{app}^{sers}
$\tau_B^f = 0.1$		
a_0	1.009	0.770
a_1	-0.049	-0.224
a_2	0.385	1.558
a_3	-1.067	-4.445
a_4	1.282	5.475
a_5	-0.527	-2.405
$\tau_B^f = 0.3$		
a_0	1.018	0.771
a_1	-0.093	-0.321
a_2	1.011	2.633
a_3	-3.423	-8.525
a_4	4.825	11.686
a_5	-2.318	-5.645
$\tau_B^f = 0.5$		
a_0	1.024	0.772
a_1	-0.039	-0.342
a_2	0.588	3.073
a_3	-2.123	-10.730
a_4	3.304	15.591
a_5	-1.745	-7.933
$\tau_B^f = 1.0$		
a_0	1.036	0.767
a_1	0.014	-0.089
a_2	0.243	0.635
a_3	-1.420	-3.341
a_4	2.899	6.954
a_5	-1.801	-4.657
$\tau_B^f = 2.0$		
a_0	1.054	0.761
a_1	-0.009	-0.193
a_2	-0.480	0.208
a_3	3.258	1.979
a_4	-5.666	-4.302
a_5	2.942	1.883
$\tau_B^f = 4.0$		
a_0	1.067	0.747
a_1	-0.109	-0.236
a_2	0.553	0.634
a_3	-0.973	0.693
a_4	0.664	-3.628
a_5	-0.232	2.032
$\tau_B^f = 8.0$		
a_0	1.063	0.729
a_1	-0.173	-0.075
a_2	1.136	-1.370
a_3	-3.829	7.179
a_4	6.316	-12.867
a_5	-3.938	6.722

Table B.48. Dust effects $corr^{dust}$, as in Table B.46, but in I band.

exponential bulges (Sérsic fits); I band		
	$\frac{R_{app}}{R_i}$	n_{app}^{sers}
$\tau_B^f = 0.1$		
a_0	1.003	0.760
a_1	0.029	0.000
a_2	-0.082	0.000
a_3	0.081	0.000
a_4	0.012	0.000
a_5	-0.020	0.000
$\tau_B^f = 0.3$		
a_0	1.009	0.762
a_1	0.033	-0.134
a_2	0.012	1.363
a_3	-0.334	-4.789
a_4	0.677	6.785
a_5	-0.347	-3.320
$\tau_B^f = 0.5$		
a_0	1.015	0.765
a_1	-0.010	-0.037
a_2	0.560	0.533
a_3	-2.371	-2.666
a_4	3.705	4.699
a_5	-1.876	-2.656
$\tau_B^f = 1.0$		
a_0	1.031	0.774
a_1	-0.079	-0.285
a_2	0.937	2.444
a_3	-3.209	-8.784
a_4	4.759	13.299
a_5	-2.458	-7.053
$\tau_B^f = 2.0$		
a_0	1.046	0.767
a_1	0.015	-0.063
a_2	0.026	0.168
a_3	-0.339	-1.424
a_4	1.122	4.026
a_5	-0.888	-3.222
$\tau_B^f = 4.0$		
a_0	1.065	0.761
a_1	-0.091	-0.243
a_2	0.235	0.916
a_3	0.673	-0.973
a_4	-1.908	0.109
a_5	1.036	-0.371
$\tau_B^f = 8.0$		
a_0	1.074	0.748
a_1	-0.144	-0.293
a_2	0.492	0.812
a_3	-0.462	-0.670
a_4	-0.237	-0.278
a_5	0.287	-0.397

Table B.49. Dust effects $corr^{dust}$, as in Table B.46, but in J band.

exponential bulges (Sérsic fits); J band		
	$\frac{R_{app}}{R_i}$	n_{app}^{sers}
$\tau_B^f = 0.1$		
a_0	1.005	0.769
a_1	-0.059	-0.210
a_2	0.450	1.412
a_3	-1.315	-3.922
a_4	1.636	4.759
a_5	-0.716	-2.087
$\tau_B^f = 0.3$		
a_0	1.010	0.771
a_1	-0.094	-0.343
a_2	0.826	2.725
a_3	-2.614	-8.447
a_4	3.453	11.085
a_5	-1.586	-5.162
$\tau_B^f = 0.5$		
a_0	1.014	0.773
a_1	-0.129	-0.475
a_2	1.202	4.038
a_3	-3.899	-12.972
a_4	5.241	17.412
a_5	-2.443	-8.238
$\tau_B^f = 1.0$		
a_0	1.022	0.770
a_1	-0.108	-0.291
a_2	1.045	2.310
a_3	-3.385	-7.342
a_4	4.609	10.013
a_5	-2.165	-4.882
$\tau_B^f = 2.0$		
a_0	1.035	0.772
a_1	-0.143	-0.430
a_2	1.486	3.754
a_3	-5.054	-12.603
a_4	7.323	17.854
a_5	-3.706	-9.001
$\tau_B^f = 4.0$		
a_0	1.053	0.770
a_1	-0.169	-0.261
a_2	1.667	2.315
a_3	-5.359	-8.810
a_4	7.433	13.870
a_5	-3.733	-7.730
$\tau_B^f = 8.0$		
a_0	1.068	0.757
a_1	-0.037	-0.002
a_2	0.087	-1.189
a_3	-0.037	4.209
a_4	0.225	-4.765
a_5	-0.382	1.136

Table B.50. Dust effects $corr^{dust}$, as in Table B.46, but in K band.

exponential bulges (Sérsic fits); K band

	$\frac{R_{app}}{R_i}$	n_{app}^{sers}
$\tau_B^f = 0.1$		
a_0	1.006	0.770
a_1	-0.011	-0.032
a_2	0.126	0.311
a_3	-0.392	-1.057
a_4	0.509	1.455
a_5	-0.236	-0.696
$\tau_B^f = 0.3$		
a_0	1.007	0.771
a_1	-0.025	-0.101
a_2	0.292	1.002
a_3	-0.980	-3.468
a_4	1.339	4.872
a_5	-0.637	-2.380
$\tau_B^f = 0.5$		
a_0	1.009	0.771
a_1	-0.036	-0.104
a_2	0.421	1.057
a_3	-1.444	-3.752
a_4	2.008	5.413
a_5	-0.966	-2.722
$\tau_B^f = 1.0$		
a_0	1.012	0.771
a_1	-0.008	-0.066
a_2	0.201	0.712
a_3	-0.761	-2.669
a_4	1.144	4.074
a_5	-0.578	-2.172
$\tau_B^f = 2.0$		
a_0	1.018	0.772
a_1	-0.022	-0.127
a_2	0.407	1.361
a_3	-1.547	-5.007
a_4	2.348	7.433
a_5	-1.199	-3.868
$\tau_B^f = 4.0$		
a_0	1.028	0.770
a_1	0.004	-0.036
a_2	0.269	0.583
a_3	-1.202	-3.072
a_4	2.063	5.606
a_5	-1.144	-3.358
$\tau_B^f = 8.0$		
a_0	1.043	0.773
a_1	0.013	-0.152
a_2	0.350	1.078
a_3	-1.775	-3.875
a_4	3.390	6.184
a_5	-2.120	-3.670

Table B.51. Dust effects $corr^{dust}$ on the derived photometric parameters of **de Vaucouleurs bulges**: effective radius and Sérsic index. Results are listed as coefficients of polynomial fits a_k (Eq. 14) at different τ_B^f and the effective wavelength of the B band.

de Vaucouleurs bulges (Sérsic fits); B band

	$\frac{R_{app}}{R_i}$	n_{app}^{sers}
$\tau_B^f = 0.1$		
a_0	1.040	3.471
a_1	0.006	-0.072
a_2	-0.151	0.598
a_3	1.035	-0.981
a_4	-2.612	-0.978
a_5	2.174	1.375
$\tau_B^f = 0.3$		
a_0	1.041	3.310
a_1	0.051	0.042
a_2	-0.746	-1.209
a_3	3.683	8.354
a_4	-7.331	-19.540
a_5	5.060	13.095
$\tau_B^f = 0.5$		
a_0	1.030	3.220
a_1	-0.074	–
a_2	0.854	–
a_3	-2.969	–
a_4	3.018	–
a_5	0.274	–
$\tau_B^f = 1.0$		
a_0	1.095	3.303
a_1	-0.076	-0.296
a_2	0.928	3.450
a_3	-3.702	-11.970
a_4	5.501	14.094
a_5	-2.408	-8.427
$\tau_B^f = 2.0$		
a_0	1.126	2.885
a_1	–	-0.581
a_2	–	6.413
a_3	–	-25.091
a_4	–	27.521
a_5	–	-11.171
$\tau_B^f = 4.0$		
a_0	–	–
a_1	–	–
a_2	–	–
a_3	–	–
a_4	–	–
a_5	–	–
$\tau_B^f = 8.0$		
a_0	–	–
a_1	–	–
a_2	–	–
a_3	–	–
a_4	–	–
a_5	–	–

Table B.52. Dust effects $corr^{dust}$, as in Table B.51, but in V band.

de Vaucouleurs bulges (Sérsic fits); V band		
	$\frac{R_{app}}{R_i}$	n_{app}^{sers}
$\tau_B^f = 0.1$		
a_0	1.036	3.481
a_1	0.005	-0.120
a_2	-0.110	1.271
a_3	0.704	-4.055
a_4	-1.707	4.397
a_5	1.381	1.800
$\tau_B^f = 0.3$		
a_0	1.040	3.351
a_1	0.033	-0.095
a_2	-0.475	0.704
a_3	2.352	-0.374
a_4	-4.750	-4.055
a_5	3.377	3.832
$\tau_B^f = 0.5$		
a_0	1.029	3.230
a_1	0.083	0.082
a_2	-1.228	-1.837
a_3	6.016	11.714
a_4	-11.658	-26.833
a_5	7.856	18.614
$\tau_B^f = 1.0$		
a_0	1.002	3.301
a_1	0.118	-0.187
a_2	-0.085	2.236
a_3	0.307	-8.071
a_4	–	11.552
a_5	–	-7.655
$\tau_B^f = 2.0$		
a_0	1.066	3.286
a_1	0.031	-0.387
a_2	-0.308	-1.697
a_3	0.609	–
a_4	0.581	–
a_5	-0.962	–
$\tau_B^f = 4.0$		
a_0	–	–
a_1	–	–
a_2	–	–
a_3	–	–
a_4	–	–
a_5	–	–
$\tau_B^f = 8.0$		
a_0	–	–
a_1	–	–
a_2	–	–
a_3	–	–
a_4	–	–
a_5	–	–

Table B.53. Dust effects $corr^{dust}$, as in Table B.51, but in I band.

de Vaucouleurs bulges (Sérsic fits); I band		
	$\frac{R_{app}}{R_i}$	n_{app}^{sers}
$\tau_B^f = 0.1$		
a_0	1.024	3.490
a_1	0.041	-0.062
a_2	-0.543	0.552
a_3	2.453	-1.037
a_4	-4.487	-0.706
a_5	2.874	1.238
$\tau_B^f = 0.3$		
a_0	1.025	3.370
a_1	0.018	0.021
a_2	-0.201	-0.433
a_3	0.763	2.692
a_4	-1.304	-5.885
a_5	0.964	3.550
$\tau_B^f = 0.5$		
a_0	1.028	3.340
a_1	0.011	-0.102
a_2	-0.130	2.406
a_3	0.565	-13.826
a_4	-1.212	25.338
a_5	1.103	-15.648
$\tau_B^f = 1.0$		
a_0	1.022	3.143
a_1	0.027	-0.284
a_2	-0.436	2.664
a_3	2.367	-5.718
a_4	-5.260	0.309
a_5	4.117	3.877
$\tau_B^f = 2.0$		
a_0	0.981	3.201
a_1	0.263	-0.102
a_2	-0.309	0.575
a_3	0.383	0.320
a_4	–	-3.262
a_5	–	0.292
$\tau_B^f = 4.0$		
a_0	–	–
a_1	–	–
a_2	–	–
a_3	–	–
a_4	–	–
a_5	–	–
$\tau_B^f = 8.0$		
a_0	–	–
a_1	–	–
a_2	–	–
a_3	–	–
a_4	–	–
a_5	–	–

Table B.54. Dust effects $corr^{dust}$, as in Table B.51, but in J band.

de Vaucouleurs bulges (Sérsic fits); J band		
	$\frac{R_{app}}{R_i}$	n_{app}^{sers}
$\tau_B^f = 0.1$		
a_0	1.011	3.460
a_1	-0.002	–
a_2	0.013	–
a_3	0.024	–
a_4	-0.240	–
a_5	0.296	–
$\tau_B^f = 0.3$		
a_0	1.000	3.348
a_1	0.050	–
a_2	-0.553	–
a_3	2.229	–
a_4	-3.811	–
a_5	2.367	–
$\tau_B^f = 0.5$		
a_0	0.997	3.310
a_1	0.136	–
a_2	-1.438	–
a_3	5.388	–
a_4	-8.445	–
a_5	4.798	–
$\tau_B^f = 1.0$		
a_0	1.002	3.235
a_1	0.144	-0.387
a_2	-1.544	3.685
a_3	5.920	-11.578
a_4	-9.600	13.990
a_5	5.700	-6.003
$\tau_B^f = 2.0$		
a_0	1.014	3.081
a_1	0.037	-0.036
a_2	-0.347	-0.372
a_3	1.263	4.406
a_4	-2.352	-10.317
a_5	1.921	5.965
$\tau_B^f = 4.0$		
a_0	1.172	3.776
a_1	0.026	-0.164
a_2	-0.145	-3.411
a_3	-0.209	5.554
a_4	1.412	2.182
a_5	-0.508	-7.747
$\tau_B^f = 8.0$		
a_0	–	–
a_1	–	–
a_2	–	–
a_3	–	–
a_4	–	–
a_5	–	–

Table B.55. Dust effects $corr^{dust}$, as in Table B.51, but in K band.

de Vaucouleurs bulges (Sérsic fits); K band		
	$\frac{R_{app}}{R_i}$	n_{app}^{sers}
$\tau_B^f = 0.1$		
a_0	1.010	3.439
a_1	-0.002	–
a_2	0.064	–
a_3	-0.333	–
a_4	0.557	–
a_5	-0.253	–
$\tau_B^f = 0.3$		
a_0	0.992	3.359
a_1	0.008	–
a_2	-0.082	–
a_3	0.373	–
a_4	-0.810	–
a_5	0.651	–
$\tau_B^f = 0.5$		
a_0	0.985	3.330
a_1	0.017	–
a_2	-0.205	–
a_3	0.929	–
a_4	-1.833	–
a_5	1.313	–
$\tau_B^f = 1.0$		
a_0	0.986	3.301
a_1	0.070	–
a_2	-0.804	–
a_3	3.294	–
a_4	-5.658	–
a_5	3.491	–
$\tau_B^f = 2.0$		
a_0	0.998	3.234
a_1	0.125	–
a_2	-1.441	–
a_3	5.890	–
a_4	-9.992	–
a_5	6.040	–
$\tau_B^f = 4.0$		
a_0	1.090	3.350
a_1	0.153	3.239
a_2	–	-28.937
a_3	–	112.177
a_4	–	-173.207
a_5	–	89.894
$\tau_B^f = 8.0$		
a_0	1.095	3.292
a_1	0.204	2.851
a_2	–	-26.095
a_3	–	104.732
a_4	–	-172.223
a_5	–	95.467

Table B.56. Dust effects $corr^{dust}$ on the effective radius of **de Vaucouleurs bulges**. Results are listed as coefficients of polynomial fits a_k (Eq. 14) at different τ_B^f and the effective wavelength of the B band.

de Vaucouleurs bulges (de Vaucouleurs fits) B band

	$\frac{R_{app}}{R_i}$
$\tau_B^f = 0.1$	
a_0	1.032
a_1	–
a_2	–
a_3	–
a_4	–
a_5	–
$\tau_B^f = 0.3$	
a_0	1.058
a_1	0.026
a_2	-0.673
a_3	4.281
a_4	-7.875
a_5	4.756
$\tau_B^f = 0.5$	
a_0	1.085
a_1	0.131
a_2	-2.090
a_3	10.459
a_4	-19.227
a_5	12.454
$\tau_B^f = 1.0$	
a_0	1.103
a_1	0.249
a_2	-4.402
a_3	25.009
a_4	-50.839
a_5	36.672
$\tau_B^f = 2.0$	
a_0	1.361
a_1	0.155
a_2	-1.500
a_3	6.354
a_4	-5.392
a_5	4.735
$\tau_B^f = 4.0$	
a_0	–
a_1	–
a_2	–
a_3	–
a_4	–
a_5	–
$\tau_B^f = 8.0$	
a_0	–
a_1	–
a_2	–
a_3	–
a_4	–
a_5	–

Table B.57. Dust effects $corr^{dust}$, as in Table B.56, but in V band.

de Vaucouleurs bulges (de Vaucouleurs fits) V band

	$\frac{R_{app}}{R_i}$
$\tau_B^f = 0.1$	
a_0	1.025
a_1	–
a_2	–
a_3	–
a_4	–
a_5	–
$\tau_B^f = 0.3$	
a_0	1.049
a_1	-0.032
a_2	0.075
a_3	1.202
a_4	-3.057
a_5	2.189
$\tau_B^f = 0.5$	
a_0	1.077
a_1	0.054
a_2	-0.955
a_3	4.866
a_4	-7.860
a_5	4.398
$\tau_B^f = 1.0$	
a_0	1.092
a_1	0.192
a_2	-2.526
a_3	10.123
a_4	-14.938
a_5	8.621
$\tau_B^f = 2.0$	
a_0	1.205
a_1	-0.375
a_2	3.183
a_3	-7.006
a_4	7.785
a_5	-0.532
$\tau_B^f = 4.0$	
a_0	–
a_1	–
a_2	–
a_3	–
a_4	–
a_5	–
$\tau_B^f = 8.0$	
a_0	–
a_1	–
a_2	–
a_3	–
a_4	–
a_5	–

Table B.58. Dust effects $corr^{dust}$, as in Table B.56, but in I band.

de Vaucouleurs bulges (de Vaucouleurs fits) I band	
	$\frac{R_{app}}{R_i}$
$\tau_B^f = 0.1$	
a_0	1.013
a_1	–
a_2	–
a_3	–
a_4	–
a_5	–
$\tau_B^f = 0.3$	
a_0	1.032
a_1	-0.021
a_2	0.102
a_3	0.407
a_4	-1.098
a_5	0.712
$\tau_B^f = 0.5$	
a_0	1.058
a_1	0.027
a_2	-0.389
a_3	1.594
a_4	-1.680
a_5	0.615
$\tau_B^f = 1.0$	
a_0	1.092
a_1	0.076
a_2	-1.151
a_3	5.113
a_4	-7.487
a_5	3.930
$\tau_B^f = 2.0$	
a_0	1.105
a_1	0.529
a_2	-6.475
a_3	26.449
a_4	-41.819
a_5	24.295
$\tau_B^f = 4.0$	
a_0	–
a_1	–
a_2	–
a_3	–
a_4	–
a_5	–
$\tau_B^f = 8.0$	
a_0	–
a_1	–
a_2	–
a_3	–
a_4	–
a_5	–

Table B.59. Dust effects $corr^{dust}$, as in Table B.56, but in J band.

de Vaucouleurs bulges (de Vaucouleurs fits) J band	
	$\frac{R_{app}}{R_i}$
$\tau_B^f = 0.1$	
a_0	1.005
a_1	–
a_2	–
a_3	–
a_4	–
a_5	–
$\tau_B^f = 0.3$	
a_0	1.008
a_1	0.008
a_2	-0.224
a_3	1.774
a_4	-3.525
a_5	2.131
$\tau_B^f = 0.5$	
a_0	1.017
a_1	0.178
a_2	-2.133
a_3	8.677
a_4	-13.472
a_5	7.233
$\tau_B^f = 1.0$	
a_0	1.043
a_1	0.416
a_2	-4.778
a_3	18.737
a_4	-28.821
a_5	15.516
$\tau_B^f = 2.0$	
a_0	1.101
a_1	0.192
a_2	-3.501
a_3	15.213
a_4	-24.238
a_5	13.756
$\tau_B^f = 4.0$	
a_0	–
a_1	–
a_2	–
a_3	–
a_4	–
a_5	–
$\tau_B^f = 8.0$	
a_0	–
a_1	–
a_2	–
a_3	–
a_4	–
a_5	–

Table B.60. Dust effects $corr^{dust}$, as in Table B.56, but in K band.

de Vaucouleurs bulges (de Vaucouleurs fits) K band	
	$\frac{R_{app}}{R_i}$
$\tau_B^f = 0.1$	
a_0	0.993
a_1	–
a_2	–
a_3	–
a_4	–
a_5	–
$\tau_B^f = 0.3$	
a_0	0.994
a_1	-0.027
a_2	0.214
a_3	-0.055
a_4	-0.601
a_5	0.531
$\tau_B^f = 0.5$	
a_0	0.999
a_1	-0.003
a_2	-0.046
a_3	0.871
a_4	-1.958
a_5	1.239
$\tau_B^f = 1.0$	
a_0	1.005
a_1	0.159
a_2	-1.858
a_3	7.242
a_4	-10.986
a_5	5.819
$\tau_B^f = 2.0$	
a_0	1.058
a_1	0.050
a_2	-3.021
a_3	13.898
a_4	-22.302
a_5	12.164
$\tau_B^f = 4.0$	
a_0	–
a_1	–
a_2	–
a_3	–
a_4	–
a_5	–
$\tau_B^f = 8.0$	
a_0	–
a_1	–
a_2	–
a_3	–
a_4	–
a_5	–